ANALYTICAL EARTH-AEROCAPTURE GUIDANCE

A Dissertation

presented to

the Faculty of the Graduate School

at the University of Missouri-Columbia

In Partial Fulfillment

of the Requirements for the Degree

Doctor of Philosophy

---

by

IBRAHIM HALIL CIHAN

Dr. Craig Kluever, Dissertation Supervisor

DECEMBER 2020

The undersigned, appointed by the dean of the Graduate School, have examined the dissertation entitled

ANALYTICAL EARTH-AEROCAPTURE GUIDANCE

presented by Ibrahim Halil Cihan,

a candidate for the degree of Doctor of Philosophy,

and hereby certify that, in their opinion, it is worthy of acceptance.

Professor Craig Kluever

Professor Ming Xin

Professor Zaichun Frank Feng

Professor Roger Fales

Professor William Banks

ACKNOWLEDGEMENTS

First and foremost, I would like to express my sincere gratitude to my advisor, Dr. Craig Kluever, for guiding and supporting me during my Master's and PhD degree. This thesis would not have been possible without his support, patience, ideas and editing skills. Since I started working under his guidance in 2015, I have always been honored to be his student. I would also like to thank Dr. Ming Xin, Dr. Zaichun Feng, Dr. Roger Fales, and Dr. William Banks for being on my committee and contributing to my research with your ideas and feedback.

I would like to thank my parents, Mr. S. Cihan and Mrs. Z. Cihan, my sister Nadire and brother Mustafa for their love and encouragement. Even though I live more than ten thousand kilometers away from them, I always feel them with me.

I have been very happy to live in Columbia, MO, USA for 6 years. I have met many wonderful people in this lovely small town. Special thanks go to some of these friends: Ersen Uzun, Fatih Ertugrul, Fawaz Al-Bakri, Funda Taskiran, Huseyin Akkus, Idris Demirsoy, Kamran Mammadov, Mustafa Karnas, Szilard Bott, and Turgay Yildirim. Perhaps it is these people who make this town meaningful to me.

Finally, I must thank my Turkish Government for their financial support to study abroad including a language school, master, and doctorate programs. It would be a dream for me to come to the USA and study here if I did not get financial help from the Government.

TABLE OF CONTENTS

LIST OF FIGURES

LIST OF TABLES

SYMBOLS

a	Semimajor axis (km)
c	Inequality constraint
C_D	Drag coefficient
C_L	Lift coefficient
D	Drag acceleration (m/s^2)
e	Eccentricity
g_r	Radial gravitational acceleration (m/s^2)
g_ϕ	Latitudinal gravitational acceleration (m/s^2)
g_0	Gravitational acceleration at sea level (m/s^2)
h	Altitude (km)
h_{a0}	Apoapsis altitude of post-aerocapture orbit (km)
h_{PU}	Pull-up altitude (km)
h_{sat}	Bank saturation altitude (km)
i	Inclination (deg)
i_{rev}	Bank reversal inclination (deg)
I_{sp}	Specific impulse of propellant (s)
J_2	Second zonal coefficient
L	Lift acceleration (m/s^2)
L/D	Lift-to-drag ratio
m	Mass (kg)
m_p	Propellant mass (kg)
r	Radial distance (km)
r_{a0}	Apoapsis radius of post-aerocapture orbit (km)
r_{p0}	Periapsis radius of post-aerocapture orbit (km)
r_{tgt}	Radius of circular target orbit (km)
R_e	Earth's equatorial radius (km)
S	Reference area (m^2)
t	Time (s)

t_s	Switching time (s)
V	Earth-relative velocity (km/s)
V_c	Circular velocity (km/s)
V_i	Inertial velocity (km/s)
w	Frequency
γ	Flight-path angle (deg)
ΔV	In-plane velocity increment (m/s^2)
ΔV_i	Plane-change velocity increment (m/s^2)
ΔV_T	Summation of in-plane and plane change velocity increment (m/s^2)
θ	Longitude (deg)
μ	Earth's gravitational parameter (km^3/s^2)
ξ	Total mechanical energy per unit mass (km^2/s^2)
ρ	Atmospheric density (kg/m^3)
σ	Bank angle (deg)
σ_l	Upper bound of bang-bang bank control (deg)
σ_u	Lower bound of bang-bang bank control (deg)
ϕ	Latitude (deg)
ψ	Heading angle (deg)
ω	Earth's angular velocity (rad/s)

ABBREVIATIONS

APC	Analytical Predictor Corrector
CM	Crew Module
EC	Energy Controller
ECEF	Earth-Centered Earth-Fixed
EI	Entry Interface
FPA	Flight-Path Angle
HYPAS	Hybrid Predictor-Corrector Aerocapture Scheme
LVLH	Local-Vertical Local-Horizontal
MPCV	Multi-Purpose Crew Vehicle
NPC	Numerical Predictor Corrector
SDE	State Differential Equation
SM	Service Module
TPC	Terminal Point Controller

ABSTRACT

Aerocapture is a technique of employing a single atmospheric pass to inserts a spacecraft from a hyperbolic orbit, approaching from deep space, into an elliptical (captured) orbit around its destination planet. After atmospheric flight and energy dissipation, propulsive maneuvers are needed to be performed to place the spacecraft in a target orbit. The exo-atmospheric propulsive maneuvers require much less propellant consumption compared to conventional orbit capture methods. This research aims to develop a new analytical predictor-corrector (APC) guidance method for the Earth-aerocapture problem in order to provide near-optimal performance in terms of exo-atmopheric velocity impulses required to establish the desired target orbit. The optimal aerocapture problem is analyzed using the bang-bang bank control structure. This thesis presents a bank-modulation APC guidance algorithm consisting of two phases: descent phase (lift-up) and ascent phase (lift-down) to mimic the optimal bang-bang bank angle structure. The APC guidance relies on open-loop and closed-loop bank control laws during the descent and ascent phases, respectively. Using the parameterizations of the aerodynamic acceleration effects and the flight-path angle term as a function of altitude, a closed-form expression of atmospheric exit velocity is obtained. Two separate scenarios (Fourier curve fitting and exponential curve fitting) are implemented to parameterize the aerodynamic acceleration effects, while the flight-path angle is parameterized with a single term exponential function. After the bank-switching (from open-loop to closed-loop control) is reached, the bank angle is continuously commanded in the ascent phase to track the reference flight-path angle profile and achieve desired exit conditions. A bank-reversal logic is developed to minimize the difference between the inclination of the post-atmospheric orbit and the desired target

inclination. Using large dispersions in the vehicle parameters, entry state, and atmospheric density, Monte-Carlo simulations are executed to test the performance and robustness of the proposed APC guidance algorithm. The simulation results reveal that the well-developed APC guidance algorithm provides the robustness and near-optimal performance.

CHAPTER 1 - INTRODUCTION

1.1 Background and Motivation

Aerocapture is a cost-effective orbital insertion maneuver to capture a spacecraft using aerodynamic forces during a single atmospheric pass. For a successful aerocapture, the spacecraft should enter the atmosphere within the acceptable aerocapture entry corridor, and then it should be guided by utilizing aerodynamic forces during the atmospheric flight phase. The kinetic energy is reduced by flying the interplanetary spacecraft through the atmosphere because of aerodynamic drag force. Diminishing orbital energy enables the vehicle to transition from a higher-energy orbit to a lower-energy orbit. This lower-energy orbit has a periapsis radius that is within the planet's atmosphere. To prevent re-entry into the atmosphere (almost one revolution later), a propulsive maneuver is needed to raise the periapsis radius. If more orbit-insertion maneuvers, such as apoapsis correction and plane-change impulsive maneuvers, are required for achieving the desired target orbit, they are typically performed during the post-aerocapture orbit.

Aerocapture has been investigated for a few decades. Although aerocapture has not yet been applied on a space flight mission, it is one of the promising technologies for future science missions thanks to the fact that it requires less propellant mass to accomplish an orbit transfer task when compared to the conventional propulsive maneuver. This technology gives the opportunity to reduce the cost and mass of the interplanetary spacecraft. The use of aerocapture can result in saving significant amounts of propellant; hence, additional science payload mass could be delivered to the destination or total vehicle launch mass could be reduced by using a smaller launch vehicle for the mission.

References [1-7] present studies that demonstrate the potential benefits of using aerocapture for interplanetary missions.

Aerocapture is a subcategory of aeroassist maneuver, along with aerobraking. For a aerobraking mission, firstly a spacecraft is needed to be inserted into a highly elliptical capture orbit from a hyperbolic approach orbit by using a propulsive burn, and then multiple low-density atmospheric passes at periapsis causes the apoapsis to gradually shrink, and eventually make the orbit circular [8, 9]. Although both techniques utilize the atmospheric drag to slow down the spacecraft, aerocapture provides some advantages over aerobraking, such as better fuel efficiency, single pass (shorter operational time), and less chance of failure. Aerocapture applications are more suitable for the outer planet missions [6]. On the other hand, aerocapture requires a heavy aeroshell to protect the vehicle from heat. The previous works related to aerocapture guidance are represented in the following section.

1.2 Prior Work

In recent decades, aerocapture has been one of the most popular subjects among interplanetary mission researchers. Different guidance techniques have been developed for solving the aerocapture problem. There is no doubt that the onboard guidance system requires a closed-loop algorithm to successfully complete aerocapture mission in the presence of significant modelling and environmental dispersions. Closed-loop guidance techniques can be broadly classified as implicit and explicit guidance method [10]. Implicit guidance methods attempt to track a predefined reference trajectory, while explicit guidance methods solve repeatedly the system equations of motion onboard in order to re-compute an optimal or near-optimal trajectory from the present state to a target state. For

onboard computational cost, the use of the implicit guidance method has advantages over the explicit guidance method. This is because most of the guidance calculations are made for possible scenarios before a mission begins. The explicit guidance scheme, on the other hand, provide a better guidance accuracy for the more difficult scenarios with unpredictable modelling and atmospheric uncertainties. An implicit guidance scheme was developed by Gurley in the 1990s for Mars aerocapture [11]. Gurley examined the use of pitch attitude modulation to track the energy of a reference trajectory. Ro et al. [12] developed a Mars terminal-point controller (TPC) guidance method. TPC is based on a calculus of variation approach and uses a reference trajectory generated offline. In [12], the controller gains were computed in a feedback guidance loop to steer the vehicle to a desired target state. References [13, 14] present other TPC guidance methods that used angle-of-attach as a control variable for Neptune and Mars aerocapture, respectively.

The most common explicit aerocapture guidance algorithms studied in the past are Analytical Predictor Corrector (APC) and Numerical Predictor Corrector (NPC) methods. References [15-28] have employed APC guidance schemes that make use of analytical approaches to predict the exit condition of the current vehicle state. Peng et al. developed three different APC guidance schemes based on lift-modulation (via bank angle) [15] and drag-modulation (via ballistic coefficient) [15, 16] control systems for Mars aerocapture. The algorithm used in the lift modulation mode was divided in two phases: near-equilibrium glide and exit phases. The bank angle in lift modulation is commanded for tracking of the reference path determined according to drag and altitude-rate error feedback. Using a piecewise linear function between flight-path angle and velocity resulted in a closed-loop drag continuous control in [15], while the single- and two-ballistic

coefficient switching scenarios are analyzed in [16]. References [17-19] also present various semi-analytical predictor-corrector techniques that are based on drag error and altitude rate. The proposed semi-analytical guidance algorithm in [19] was tested for aerocapture at several planetary exploration destinations including Earth, Mars, Titan, Neptune, and Venus. References [21-23] employ Hybrid Predictor Corrector Aerocapture Scheme (HYPAS) that consists of two phases during atmospheric flight; equilibrium-glide phase where a spacecraft flies at a constant flight-path angle (FPA) by modulating bank angle, followed by a constant altitude-rate phase that corrected control variable to steer the spacecraft to desired predicted state. Hamel and Lafontaine [24] improved the robustness and accuracy of this APC guidance method for Mars aerocapture by running a scale height adaptation algorithm that used the density estimation. CNES and NASA teams developed an energy controller (EC) guidance for Mars Sample Return mission [25]. The purpose of the EC method is to minimize the difference between the target exit energy and the predicted exit energy by making analytical assumptions.

The NPC guidance designs rely on numerical integration of the governing equations of motion [29-38]. In order to predict the exit state, the on-board computer of the spacecraft numerically simulates the trajectory from the present point to an exit state. By using the PredGuide+A aerocapture guidance scheme, Lafleur [29] investigated the apoapsis targeting mode (single-impulsive maneuver) and ΔV-minimization mode (two-impulsive maneuver) for Lunar return cases. Both the apoapsis targeting and ΔV-minimization modes seek a constant bank angle profile for the remainder of atmospheric flight phase to achieve the desired exit state. Lu et al. [30] employed a bang-bang bank angle profile to minimize the post-exit propellant consumption for Earth aerocapture problem. The guidance

algorithm consists of two phases. They selected a 15-95 deg bang-bang bank profile instead of using a 0-180 deg (full lift-up during first phase and full lift-down during second phase) to balance between performance and guidance robustness. The bank angle remained constant (at 15 deg) during the first phase. The switching time from first phase to second phase was found by using Brent's and golden-section methods [39] for two different modes. In the second phase, a constant bank angle magnitude was sought at each guidance cycle to reach the desired apoapsis. In Ref. [31], this bang-bang control structure was tested using two Mars-aerocapture scenarios for three different entry vehicles. Putnam and Braun [33] developed three drag modulation control systems (single-stage jettison, two-stage jettison, and continuously-variable) for aerocapture at Venus, Mars, and Titan.

The APC, NPC, TPC, and EC guidance algorithms were compared by a CNES-NASA collaborative working group for accuracy, robustness, loads, and complexity criterions in Ref. [40]. According to the results of the comparison of four criterions, the TPC algorithm achieved the highest ranking, followed by the APC, EC, and NPC algorithms. The TPC was presented as the best general algorithm thanks to slightly better in robustness and complexity criterions. On the other side, the APC algorithm was ranked first in accuracy and loads criterions. The NPC guidance method have highest onboard computational requirements. It should be noted that the CNES/NASA study was published in 2012. Since then, a large number of studies has been conducted to improve these guidance algorithms. It is therefore useful to re-compare these methods by including newly developed guidance algorithms.

1.3 Thesis Outline

Chapter 2 describes the formulation of aerocapture guidance problem after giving a brief description of the spacecraft used in this thesis. This chapter includes Orion MPCV's equations of motion, transforming the Earth-relative state variables into inertial system, and impulsive in-plane and out-of-plane orbital maneuvers transporting the Orion MPCV's from a post-atmospheric orbit to a desired target orbit.

Chapter 3 focuses on the bang-bang aerocapture optimization problem. This chapter also introduces the Fmincon algorithm used to minimize the post-exit ΔV (required to achieve the target orbit) for the bang-bang bank control structure. The goal of this chapter is to figure out the optimal bang-bang solutions which will be compared to the proposed APC guidance scheme.

Chapter 4 presents the analytical aerocapture guidance algorithm. Atmospheric flight phase is separated into two phases: descent (open-loop bank) and ascent (closed-loop bank) phases. During the ascent phase, the analytical prediction of exit velocity is achieved by using a Fourier curve fitting (scenario 1) or an exponential curve fitting (scenario 2) method to parameterize the aerodynamic acceleration effects. This chapter also describe the switching point (from open-loop to closed-loop bank phase) and bank reversal criteria.

Chapter 5 presents numerical results of this research. This chapter begins with Monte-Carlo dispersions, followed by nominal and off-nominal simulated trajectories for scenario 1 and scenario 2. It then provides a comparison of APC and NPC methods for the same Earth aerocapture mission. Lastly, this chapter evaluates the response of the APC guidance method to the entry condition with a wide range of FPA.

Finally, Chapter 6 gives a summary and conclusion of the thesis. This chapter also includes some key findings of the proposed APC guidance algorithm.

The main objective of this study is to design a novel APC guidance algorithm that provides near-optimal performance in terms of post-exit propulsive burn. The secondary goal is to improve the robustness of the algorithm with respect to atmospheric modeling uncertainty. In addition to these goals, it is important to provide near-optimal performance at inexpensive computational resources.

CHAPTER 2 – SYSTEM MODELS

2.1 Vehicle Description

The spacecraft model used in the aerocapture guidance problem is the Orion multi-purpose crew vehicle (MPCV). The vehicle was built for manned exploration of the Moon and further interplanetary missions [41]. Figure 2.1 shows a concept of the Orion MPCV consisting of crew module (provides a safe habitat for the crew during spaceflight missions) and service module (provides support systems to the crew module in space). The crew module separated from the service module before the atmospheric entry is the only compartment that fulfill the aerocapture maneuver. While the crew module (CM) is a reusable space capsule, the service module (SM) usually burns up in the atmosphere before reaching the surface.

Fig. 2.1 Orion MPCV Model [42]

Table 2.1 represents some specifications of the Orion CM [29, 30]. The lift and drag coefficients of the vehicle were assumed to be constant for highly hypersonic Mach numbers [3, 43]. The Orion CM has a heavier and larger than Apollo command module. The capsule has bank angle rate and acceleration limits.

Table 2.1: Vehicle Specifications

Parameter	Value
Lift coefficient	0.3699
Drag coefficient	1.37
Mass	8983.4 kg
Reference area	19.86 m^2
Bank angle rate limit	15 deg/s
Bank angle acceleration limit	5 deg/s^2

2.2 Equations of Motion

The equations of three-dimensional motion of a spacecraft are described under the following assumptions: the Earth is an oblate spheroid and is rotating with constant angular velocity, and the atmosphere is at rest with respect to the Earth:

$$\dot{r} = V \sin\gamma \tag{1}$$

$$\dot{\theta} = \frac{V \cos\gamma \sin\psi}{r \cos\phi} \tag{2}$$

$$\dot{\phi} = \frac{V \cos\gamma \cos\psi}{r} \tag{3}$$

$$\dot{V} = -D - g_r \sin\gamma - g_\phi \cos\gamma \cos\psi + \omega^2 r \cos\phi(\sin\gamma \cos\phi - \cos\gamma \cos\psi \sin\phi) \tag{4}$$

$$\dot{\gamma} = \frac{1}{V}\left[L\cos\sigma + \left(\frac{V^2}{r} - g_r \right)\cos\gamma + g_\phi \sin\gamma \cos\psi + 2\omega V \sin\psi \cos\phi \right.$$
$$\left. + \omega^2 r \cos\phi(\cos\gamma \cos\phi + \sin\gamma \cos\psi \sin\phi) \right] \tag{5}$$

$$\dot{\psi} = \frac{1}{V}\left[\frac{L\sin\sigma}{\cos\gamma} + \left(\frac{(V\cos\gamma)^2 \tan\phi}{r} + g_\phi \right)\frac{\sin\psi}{\cos\gamma} - 2\omega V(\tan\gamma \cos\psi \cos\phi - \sin\phi) \right.$$
$$\left. + \frac{\omega^2 r}{\cos\gamma} \sin\psi \sin\phi \cos\phi) \right] \tag{6}$$

where r is the radial distance from the center of the Earth to the vehicle's center of mass, θ is the longitude, ϕ is the latitude, V is the Earth-relative velocity, γ is the flight-path angle of the Earth-relative velocity vector, ψ is the heading angle (measured clockwise from north to the projection of the Earth-relative velocity vector onto the local horizontal plane), σ is the bank angle (which is the only control variable), ω is the angular velocity of the Earth, and g_r and g_ϕ are the radial and latitudinal components of the acceleration of gravity, respectively. The aerodynamic lift and drag accelerations (L and D) are given by

$$L = \frac{1}{2}\rho V^2 \frac{S}{m} C_L \tag{7}$$

$$D = \frac{1}{2}\rho V^2 \frac{S}{m} C_D \tag{8}$$

where ρ is the atmospheric density, S is the reference area, C_L and C_D are the lift and drag coefficients, respectively, and m is the vehicle mass. The 1976 US Standard Atmosphere

is adopted for the nominal density model of Earth's atmosphere. The gravitational acceleration components are given by

$$g_r = \frac{\mu}{r^2}\left[1 + J_2\left(\frac{R_e}{r}\right)^2 (1.5 - 4.5\sin^2\phi)\right] \tag{9}$$

$$g_\phi = \frac{3\mu}{r^2} J_2\left(\frac{R_e}{r}\right)^2 \sin\phi\cos\phi \tag{10}$$

where μ is the gravitational parameter of the Earth, R_e is the equatorial radius of the Earth, and J_2 is the second zonal coefficient. The zonal variation occurs because of the oblateness. Other zonal coefficients are not included in the gravitational acceleration equations due to their small magnitudes compared to J_2. Before discussing impulsive orbital maneuver, it would be well at this point to describe the coordinate transformation which is necessary for transforming the Earth-relative-state variables to inertial-state variables.

2.3 Coordinate Transformations

The position and velocity vectors of the vehicle are shown in Figure 2.2. The position vector components are given in the Earth-centered Earth-fixed (ECEF) coordinate system as in equation (11). The three-dimensional cartesian coordinate system (X, Y, Z) is attached to the center of mass of Earth and rotates with the Earth around the Z-axis.

$$\begin{bmatrix} r_X \\ r_Y \\ r_Z \end{bmatrix} = \begin{bmatrix} r\cos\phi\cos\theta \\ r\cos\phi\sin\theta \\ r\sin\phi \end{bmatrix} \tag{11}$$

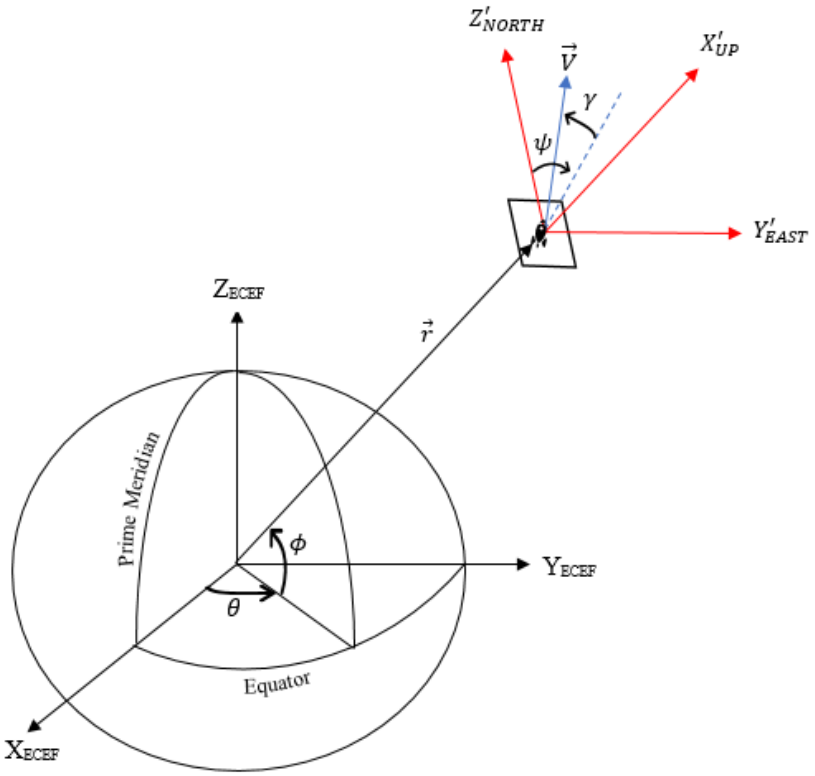

Fig. 2.2 ECEF and LVLH Coordinate Systems

The velocity vector components in the local-vertical local-horizontal (LVLH) coordinate system are

$$\begin{bmatrix} V_{UP} \\ V_{EAST} \\ V_{NORTH} \end{bmatrix} = \begin{bmatrix} V\sin\gamma \\ V\cos\gamma\sin\psi \\ V\cos\gamma\cos\psi \end{bmatrix} \tag{12}$$

Vectors can be transformed from one coordinate system to another by rotation matrices. For the velocity vector transformation from LVLH to ECEF coordinate system, two consecutive rotations are implemented. The first rotation is performed by rotating the $X'Y'Z'$ frame through $-\phi$ around Y' axis. The second one is performed by rotating through $-\theta$ about Z' axis. The velocity vector components in ECEF coordinate system can be obtained:

$$\begin{bmatrix} V_X \\ V_Y \\ V_Z \end{bmatrix} = \begin{bmatrix} \cos\theta & -\sin\theta & 0 \\ \sin\theta & \cos\theta & 0 \\ 0 & 0 & 1 \end{bmatrix} \begin{bmatrix} \cos\phi & 0 & -\sin\phi \\ 0 & 1 & 0 \\ \sin\phi & 0 & \cos\phi \end{bmatrix} \begin{bmatrix} V_{UP} \\ V_{EAST} \\ V_{NORTH} \end{bmatrix} \tag{13}$$

The inertial velocity vector $\mathbf{V}_i$ is the sum of the Earth-relative velocity vector $\mathbf{V}$ and the transport velocity vector, which is the cross product of the Earth's self-rotation angular velocity vector $\boldsymbol{\omega}$ and vehicle's position vector $\mathbf{r}$ as in equation (14):

$$\mathbf{V}_i = \mathbf{V} + \boldsymbol{\omega} \times \mathbf{r} \tag{14}$$

Detailed information about transforming the Earth-relative velocity, flight-path angle, and heading angle into the inertial system can be found in Ref [44].

2.4 Impulsive Orbital Maneuvers

The vehicle enters the Earth's atmosphere at entry interface (EI), which is defined at an altitude of 400,000 ft (121.92 km). The vehicle flies through the Earth's atmosphere while dissipating energy due to drag until the vehicle reaches the atmospheric exit altitude. EI and atmospheric exit occur at the same altitude. After atmospheric flight and energy dissipation, orbital mechanics comes into play.

In orbital mechanics, a spacecraft can be transferred from one orbit to another by impulses (propulsive burns). The impulsive velocity change (velocity increment) ΔV is a measure of the amount of propellant consumption. The relationship between ΔV and the propellant mass consumed m_p is described by the ideal (or classical) rocket equation [45]:

$$m_p = m_0 \left[1 - \exp\left(\frac{-\Delta V}{g_0 I_{sp}} \right) \right] \tag{15}$$

where m_0 is the initial mass of the vehicle before the propulsive burn, g_0 is the Earth's standard gravitational acceleration near sea level, and I_{sp} is the specific impulse of the propellant. It is considered that propulsion system provides ΔV instantly without change in the position of the vehicle. Impulses are performed to transfer a post-aerocapture orbit into a specified target orbit.

2.4.1 Coplanar Transfer with Tangential Impulses

When the apoapsis of the post-aerocapture ellipse orbit is tangent to the desired target circular orbit (case 1), one-impulsive maneuver is enough to get into the target circular orbit as shown in Figure 2.3. The velocity vectors of the tangential orbits are collinear. A single burn is applied at the apogee to raise the perigee to be the desired perigee. For case 1, the coplanar velocity increment is

$$\Delta V = \Delta V_1 = \sqrt{2\mu}\left(\sqrt{\frac{1}{2r_{\text{tgt}}}} - \sqrt{\frac{1}{r_{a0}} - \frac{1}{r_{p0}+r_{a0}}}\right) \tag{16}$$

where r_{tgt} is the radius of the target orbit, and r_{a0} and r_{p0} are the apogee and perigee radii of the exo-atmospheric orbit as determined by equations (17) and (18). Since the exo-atmospheric orbit is tangent to the desired target orbit at the apoapsis radius, $r_{a0} = r_{\text{tgt}}$ in equation (16), and the first term on the right-hand side of equation (16) expresses the circular speed of the target orbit.

$$r_{a0} = a(1+e) = a\left(1+\sqrt{1-\frac{V_{\text{exit}}^2 r_{\text{exit}}^2 \cos^2\gamma_{\text{exit}}}{\mu a}}\right) \tag{17}$$

$$r_{p0} = a(1-e) = a\left(1-\sqrt{1-\frac{V_{\text{exit}}^2 r_{\text{exit}}^2 \cos^2\gamma_{\text{exit}}}{\mu a}}\right) \tag{18}$$

where a and e are the semimajor axis and eccentricity of the post-aerocapture orbit, respectively, r_{exit} is the atmospheric exit radius, and V_{exit}, and γ_{exit} are the inertial velocity and flight-path angle at r_{exit}. Kinetic and potential energy evaluated at the exit conditions determines the semimajor axis of the post-aerocapture orbit:

$$a = \frac{-\mu}{2\xi} = \frac{\mu}{-V_{\text{exit}}^2 + 2\mu / r_{\text{EI}}} \tag{19}$$

where ξ is the total mechanical energy per unit mass which is constant during orbital flight according to the principle of conservation of energy.

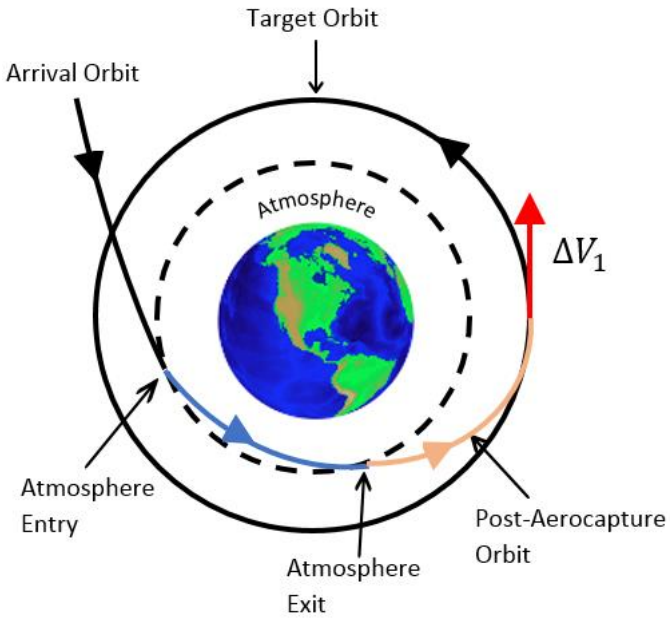

Fig. 2.3 Aerocapture Maneuver with One-Impulsive

When the apoapsis radius of the post-aerocapture orbit does not match the target circle radius (case 2), two impulsive maneuvers are required to establish target orbit as shown in

Figure 2.4. The attained r_{a0} is not restricted in case 2. The inequality relation might be $r_{a0} < r_{\text{tgt}}$ or $r_{a0} > r_{\text{tgt}}$.

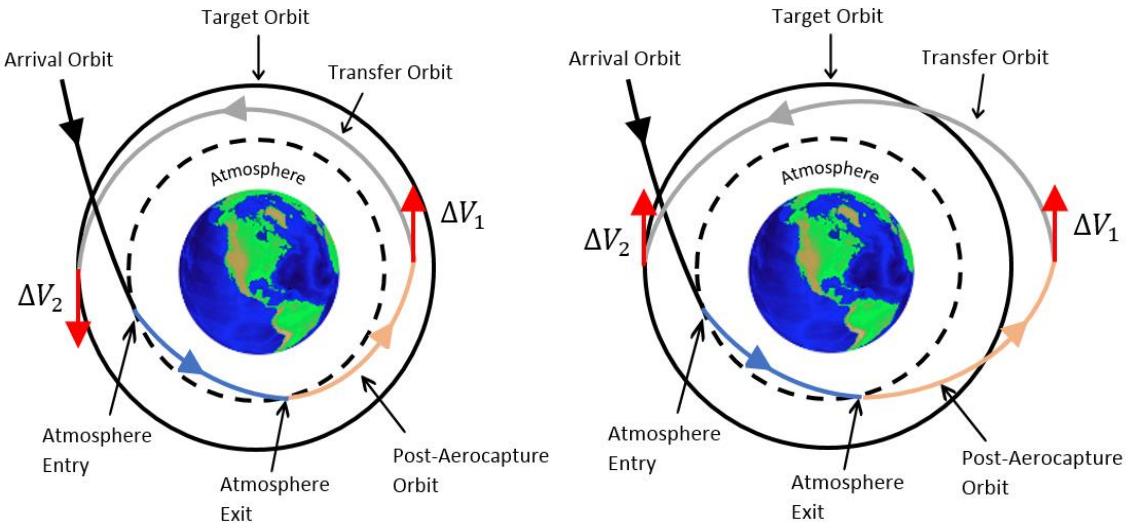

Fig. 2.4 Aerocapture Maneuvers with Two-Impulsive; (a) $r_{a0} < r_{tgt}$; (b) $r_{a0} > r_{tgt}$

The first impulse is performed at r_{a0} to raise r_{p0} to the target orbit, and then the second impulse is performed at r_{p0} to either raise the new periapsis to the target orbit (Figure 2.4a) or lowers apoapsis to the target orbit (Figure 2.4b). For case 2, the coplanar velocity increment is the sum of the magnitudes of the two impulses:

$$\Delta V = \Delta V_1 + \Delta V_2 = \sqrt{2\mu}\left(\sqrt{\frac{1}{r_{a0}} - \frac{1}{r_{\text{tgt}} + r_{a0}}} - \sqrt{\frac{1}{r_{a0}} - \frac{1}{r_{p0} + r_{a0}}}\right) + \sqrt{2\mu}\left|\sqrt{\frac{1}{2r_{\text{tgt}}} - \sqrt{\frac{1}{r_{\text{tgt}}} - \frac{1}{r_{\text{tgt}} + r_{a0}}}}\right| \tag{20}$$

The absolute value symbols should be used for the second term on the right-hand side of equation (20) in case of having $r_{a0} > r_{\text{tgt}}$.

2.4.2 Plane-Change Maneuver

To change the orientation of the orbital maneuver while its size remains the same, the direction of the velocity vector must be changed at either the ascending node or the descending node. Figure 2.5 shows a plane-change maneuver from a circular orbit (Orbit 1) to another circular orbit (Orbit 2). A velocity increment ΔV_i applied at the ascending node rotates the velocity vector V_{c1} through the dihedral angle Δi without changing its magnitude. By using the law of cosine, the required change in velocity ΔV_i can be computed by

$$\Delta V_i = 2V_c \sin\frac{\Delta i}{2} \tag{21}$$

where V_c is the circular speed (i.e., $V_c = V_{c1} = V_{c2}$) and Δi is the magnitude of the inclination change.

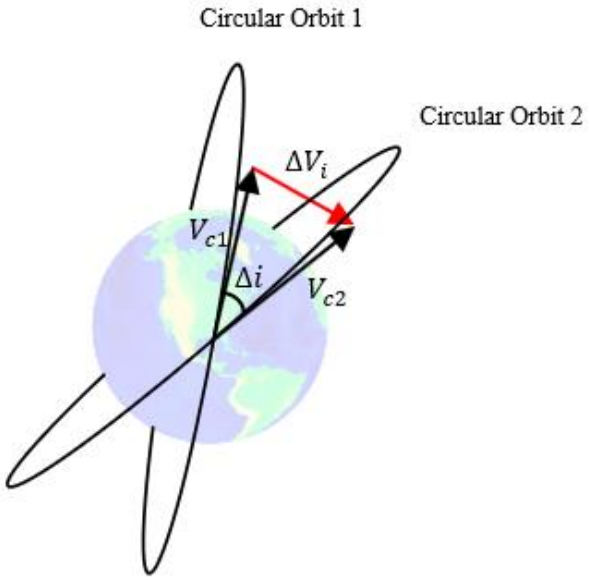

Fig. 2.5 Inclination-Change Maneuver

CHAPTER 3 – OPTIMAL AEROCAPTURE

3.1 Optimization Problem

The goal of the optimization problem is to minimize the impulsive velocity change of the aerocapture maneuver. The Orion MPCV is used as a spacecraft model in the optimization problem. The initial condition at entry interface is taken from [29, 30]. Table 3.1 shows the initial state for a nominal entry. The target orbit is circular with an altitude of 200 km and inclination of 88 deg.

Table 3.1: Nominal entry conditions

EI state	Value
Altitude	121.92 km
Longitude	−116.5 deg
Latitude	−46.67 deg
Inertial velocity	11.02 km/s
Inertial flight-path angle	−5.91 deg
Inertial heading angle	0.00 deg
Orbital inclination	90 deg

Two-impulsive velocity increment formula in equation (20) is used as a cost function in the optimization problem (note that plane-change maneuver is ignored in this chapter). When the apogee of the post-aerocapture orbit is equal to the radius of the desired target orbit, the equation (20) converts into the equation (16) (because ΔV_2 will be zero in equation (20) to achieve the desired final orbit). In most instances, one-impulsive

maneuver case provides a better performance in terms of ΔV than two-impulsive maneuver case.

The problem statement is

$$\text{Minimize:} \quad F(x) = \sqrt{2\mu}\left(\sqrt{\frac{1}{r_{a0}} - \frac{1}{r_{\text{tgt}} + r_{a0}}} - \sqrt{\frac{1}{r_{a0}} - \frac{1}{r_{p0} + r_{a0}}}\right) + \sqrt{2\mu}\left|\sqrt{\frac{1}{2r_{\text{tgt}}}} - \sqrt{\frac{1}{r_{\text{tgt}}} - \frac{1}{r_{\text{tgt}} + r_{a0}}}\right| \tag{22}$$

$$\text{Subject to:} \quad \begin{cases} \dot{y}_1 = \dot{r}, & r(0) = r_{\text{EI}} \Rightarrow \text{fixed} \\ \dot{y}_2 = \dot{\theta}, & \theta(0) = \theta_{\text{EI}} \Rightarrow \text{fixed} \\ \dot{y}_3 = \dot{\phi}, & \phi(0) = \phi_{\text{EI}} \Rightarrow \text{fixed} \\ \dot{y}_4 = \dot{V}, & V(0) = V_{\text{EI}} \Rightarrow \text{fixed} \\ \dot{y}_5 = \dot{\gamma}, & \gamma(0) = \gamma_{\text{EI}} \Rightarrow \text{fixed} \\ \dot{y}_6 = \dot{\psi}, & \psi(0) = \psi_{\text{EI}} \Rightarrow \text{fixed} \end{cases} \tag{23}$$

$$\text{Inequality constraints:} \quad c = r_{a0} > r_{\text{exit}} \tag{24}$$

It is assumed that initial condition of state variables is known for the nominal model, so it is fixed. The system needs an inequality equation (24) so that the apoapsis radius of the post-aerocapture orbit must be greater than atmospheric exit radius in order to correctly compute the cost function in equation (22).

3.2 Fmincon Algorithm

Fmincon is an optimization solver in MATLAB [46]. It attempts to find the local minimum value of a constrained nonlinear multivariable function. The syntax of the Fmincon algorithm is defined as:

$$\texttt{x = fmincon (fun, x0, A, b, } A_{eq}\texttt{, } B_{eq}\texttt{, lb, ub, nonlcon)}$$

where `x` is a solution of the optimization; `fun` is a function M-file that evaluates cost function value; `x0` is the initial estimations for `x` to begin the optimization; `A` and `b`, respectively, are the matrix and vector for linear inequality constraints; A_{eq} and B_{eq} are the matrix and vector for linear equality constraints; `lb` and `ub,` respectively, are the lower and upper bounds for the variables, and `nonlcon` is a function M-file that contains nonlinear equality and inequality constraints.

Fmincon algorithm minimizes the cost function value in equation (22). State differential equations (SDEs) in equation (23) should be integrated to assess the cost function value. Therefore, the ode45 solver in MATLAB [47] is chosen as an integration method to solve the SDEs. It integrates the system of the SDEs from initial time to final time by using the initial condition of the state variables. The syntax of the ode45 solver is

```
[t, y] = ode45(odefun, tspan, y0)
```

where `t` is evaluation points on time span; `y` is the solution of the state variables; `odefun` is a function M-file that determines the right-hand sides of the SDEs; `tspan` is the interval of integration [`t0 tf`]; `y0` is the initial condition of the state variables.

3.3 Bang – Bang Control

The impulsive velocity change can be minimized by using instantaneous bang-bang bank control when constraints on final orbital inclination are omitted (i.e., no bank reversal is necessary through the trajectory). First the spacecraft flies with full lift-up ($\sigma = 0$) during the descent phase and then full lift down ($\sigma = 180$) during the ascent phase. The bank angle transition from 0 to 180 deg happens instantaneously at the switching time t_s. The time at the atmospheric exit is free parameter and the switching time is the only variable that must be determined in the optimization problem. The optimal switching time, which minimizes the velocity increment of the aerocapture problem, can be found by using the Fmincon optimization solver. It is crucial to state that the Fmincon algorithm requires the inequality constraint ($c = r_{a0} > r_{\text{exit}}$) to define the optimal aerocapture problem correctly. Otherwise, the cost function might not converge to the solution more effectively. For instance, if the inequality constraint ($c = r_{a0} > r_{\text{exit}}$) is ignored in the optimization algorithm and a small value of the switching time is used for the initial estimation, the Fmincon algorithm might find a minimal cost value with an apoapsis altitude h_{a0} which is less than the atmospheric exit altitude r_{exit}. This means that the coplanar velocity increment equations (16) or (20) cannot be applied because the spacecraft is still in the Earth's atmosphere, and energy dissipation still exists due to drag. Thus, the inequality constraint should be included in the optimization problem to gain the optimal solution in the right way. Figures 3.1 and 3.2 present the bank angle and altitude time histories for optimal bang-bang control. The optimal switching time is $t_s = 107.307$ s, and the minimum insertion ΔV is 39.6 m/s with a single impulse where $r_{a0} = r_{\text{tgt}}$ for the nominal

model. Figure 3.3 shows the optimal FPA vs altitude profile for bang-bang control structure (σ = 0-180 deg).

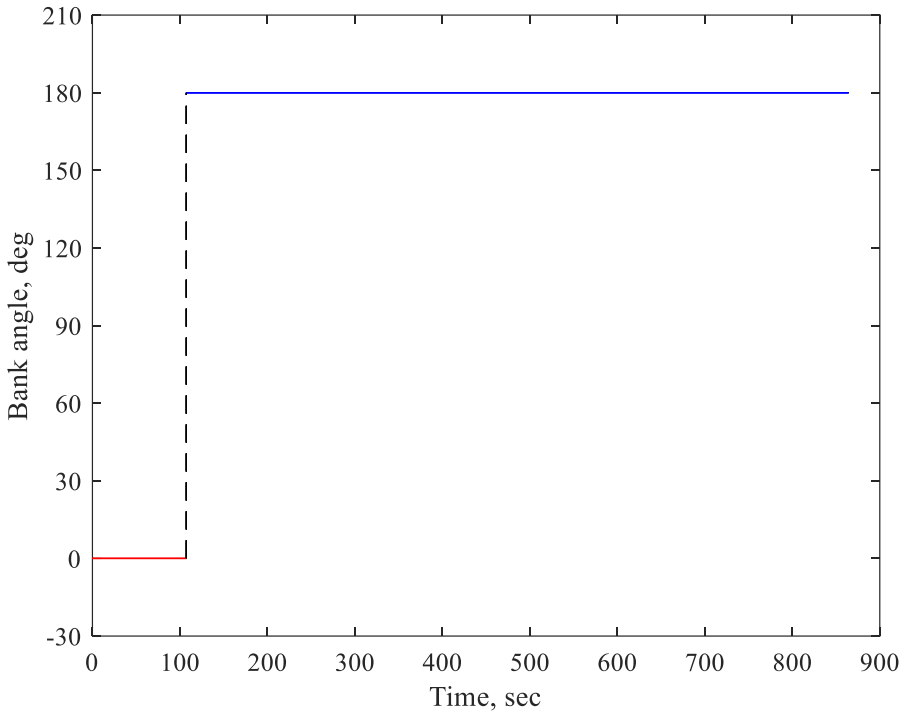

Fig. 3.1 Bank Angle vs. Time for Optimal Bang-Bang Control Problem

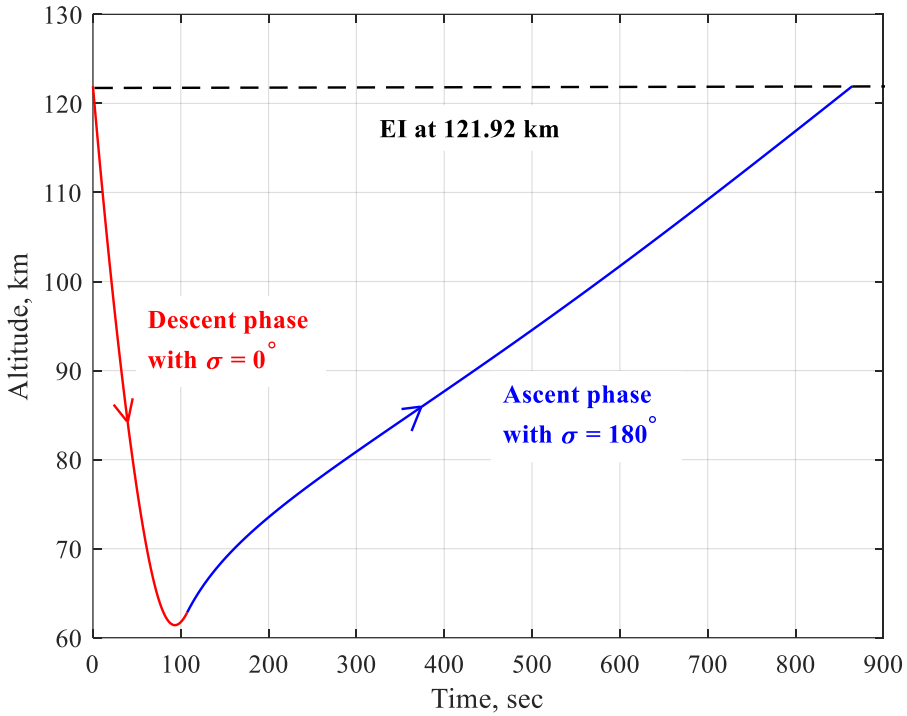

Fig. 3.2 Altitude vs. Time for Optimal Bang-Bang Control Problem

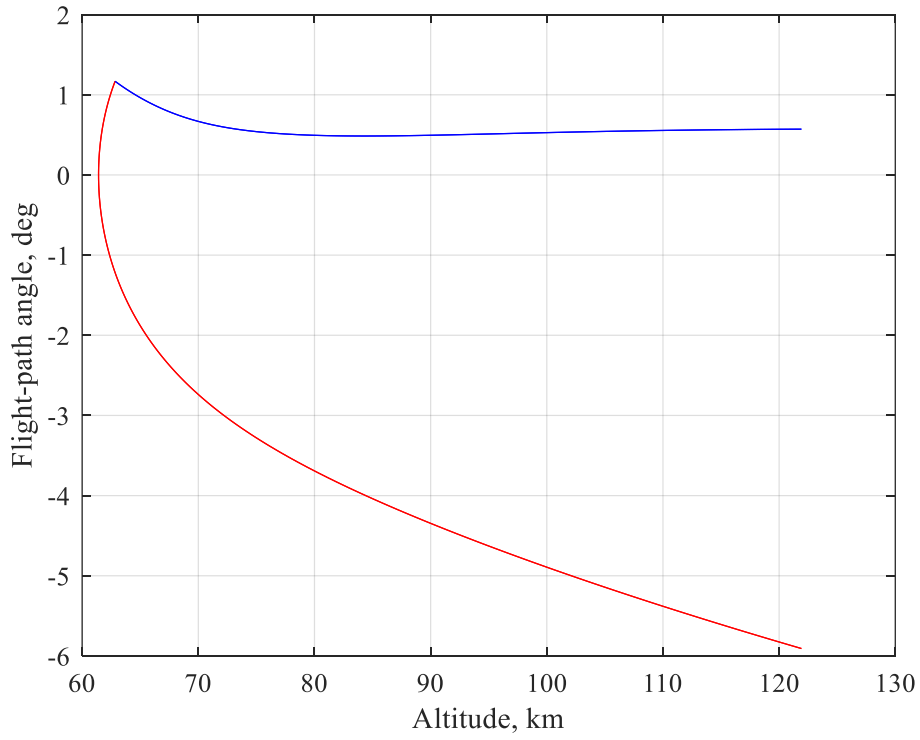

Fig. 3.3 Flight-Path Angle vs. Altitude for Optimal Bang-Bang Control Problem

The sensitivity of the aerocapture problem with respect to switching time, initial flight-path angle, and lift-to-drag ratio is investigated in this section. The most important factor on the velocity increment is the switching time. Figure 3.4 presents the total ΔV vs. switching time for bang-bang bank angle control problem. It should be noted that the total ΔV solutions in Figure 3.4 are not obtained from optimized trajectories. Changing the optimal switching time (107.307 s) by about 0.04 s doubles the total ΔV.

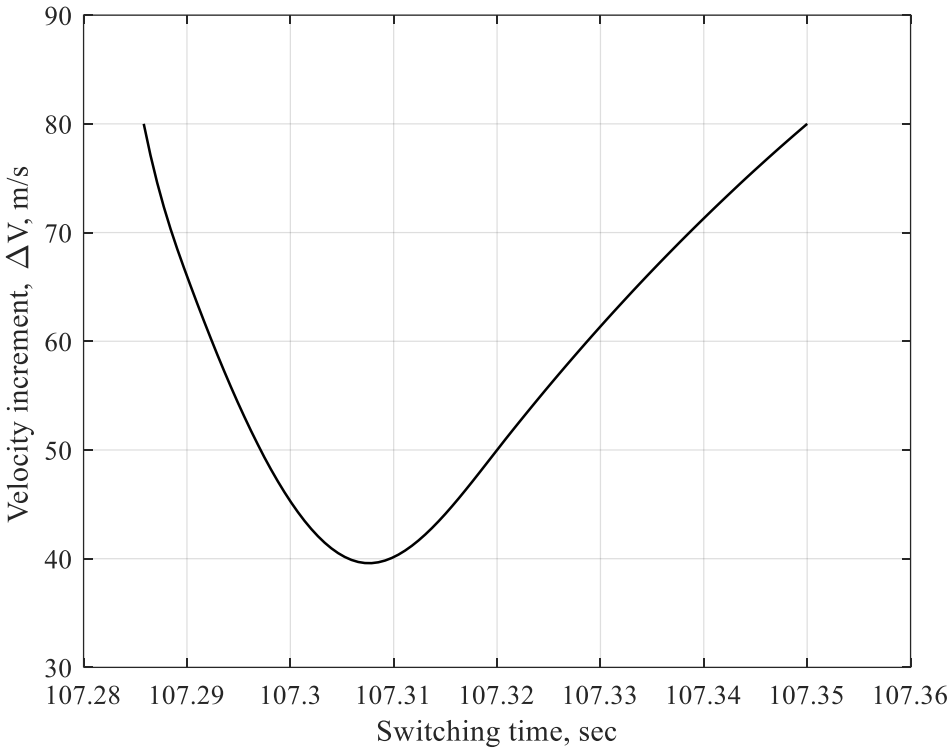

Fig. 3.4 The Effect of Switching Time on Bang-Bang Aerocapture Problem

The other two important factors on the optimal ΔV-minimization are initial flight-path angle and the lift-to-drag ratio. Figure 3.5 shows the surface plot of minimal-ΔV solutions vs. initial flight-path angle and lift-to-drag ratio. The highest values of ΔV are in the far corner of the plot, which corresponds with low values of initial flight-path angle γ_0 and

L/D ratio. As γ_0 and L/D increase, the minimum ΔV decreases. The lowest value of ΔV (36.91 m/s which is only 0.08 m/s is less than the ΔV value in the near corner of the plot) occurs at approximately $\gamma_0 = 5.85$ deg and $L/D = 0.32$. When the vehicle has a higher L/D ratio, switching the bank angle from 0 to 180 deg should be made early. This allows the vehicle to have a higher velocity and a lower flight-path angle at the exit in order to reach the desired apoapsis of target orbit. These exit variables minimize the optimal ΔV.

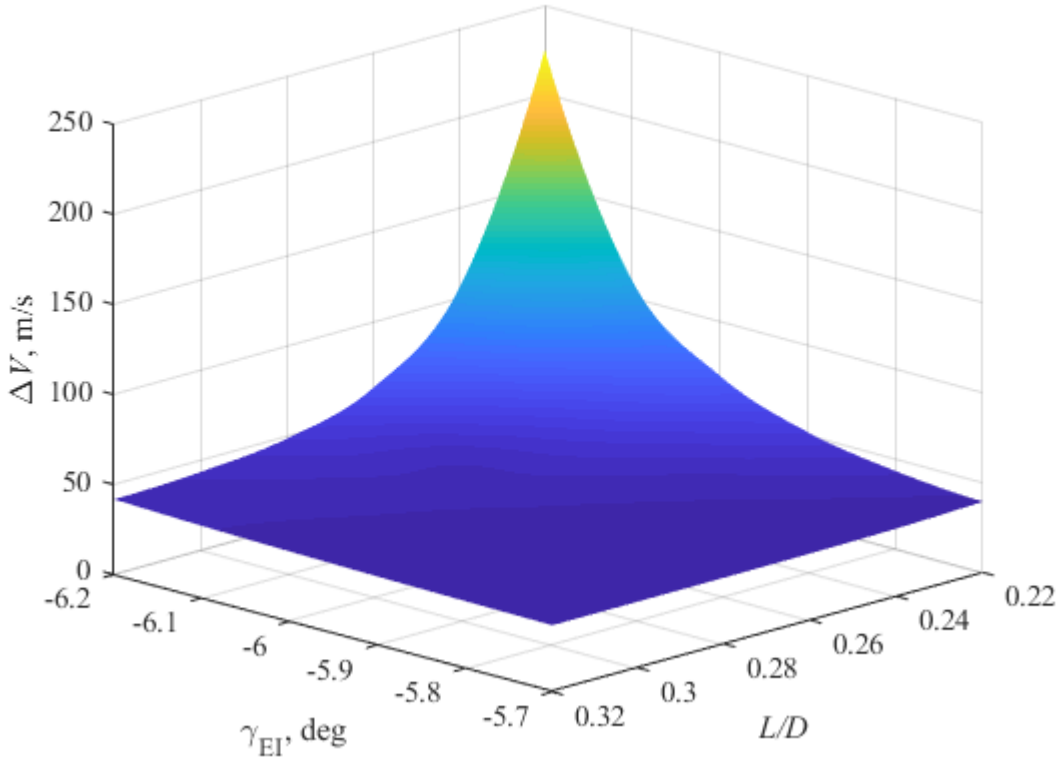

Fig. 3.5 The Effects of Initial Flight-Path Angle and Lift-to-Drag Ratio on Bang-Bang Aerocapture Problem

Lastly, several optimal bang-bang aerocapture maneuver are analyzed by running the optimization algorithm with a range of upper bound of bank angle σ_u, while the lower bound σ_l remains the same. Table 3.2 presents minimum-ΔV solutions for a range of the

upper bound. Because a constant bank angle of 56.7 deg is minimum value for a nominal aerocapture corridor, the upper bound of the bang-bang bank angle control is limited to 60 deg. While a single-impulse maneuver is required for the first 9 scenarios (0-180 to 0-100 deg) in Table 3.2, two propulsive burns are applied for the last 4 scenarios (0-90 to 0-60 deg) to establish 200×200 km target orbit. Decreasing the upper bound of the bang-bang bank angle causes early switching and some degradation in optimal velocity increment ΔV.

Table 3.2: Fmincon Optimization Results for Bang-Bang Scenarios

Bang-bang bank (deg)	Switching time (sec)	Apogee Altitude (km)	ΔV (m/s)
0-180	107.307	200.00	39.59
0-170	107.133	200.00	39.80
0-160	106.634	200.00	40.54
0-150	105.793	200.00	41.97
0-140	104.587	200.00	44.36
0-130	102.981	200.00	49.50
0-120	100.906	200.00	53.87
0-110	98.293	200.00	62.32
0-100	95.002	200.00	74.37
0-90	90.877	217.97	90.28
0-80	85.537	248.32	108.28
0-70	77.968	281.71	127.80
0-60	64.071	318.07	148.22

Figures 3.6 shows the time histories of the three bang-bang bank angle control scenarios ($\sigma = \sigma_l$-σ_u; 0-180; 0-120; and 0-60 deg) and the resulting flight-path angle and relative

velocity vs. altitude profiles are plotted in Figures 3.7 and 3.8. As shown in Table 3.2 and Figure 3.6, the higher upper bound of bank angle increases the switching time and total atmospheric flight time. As the upper bound decreases, the vehicle has a higher FPA and a lower velocity at the atmospheric exit conditions.

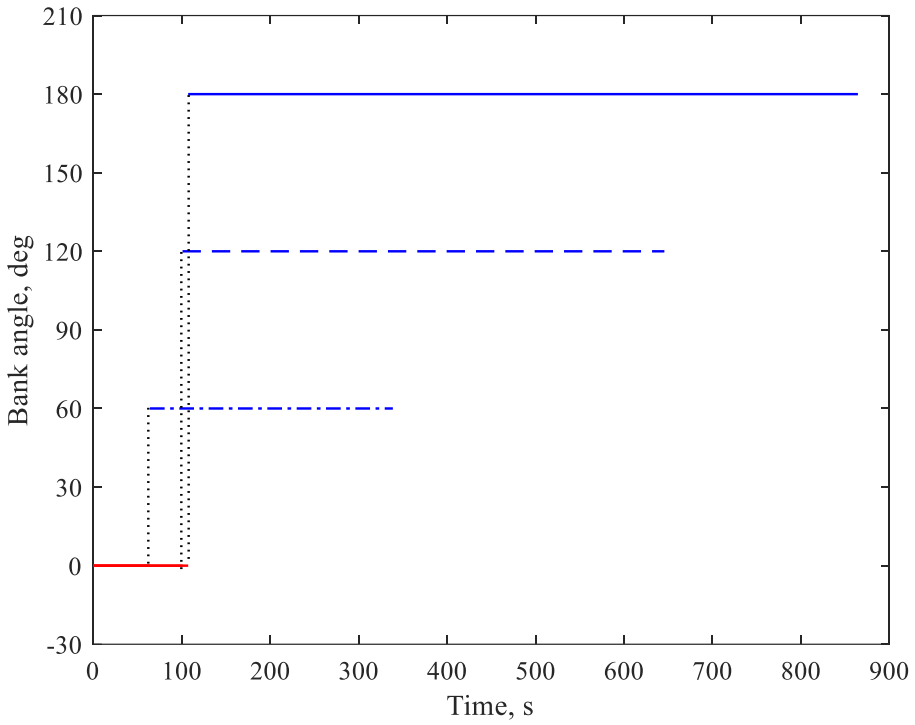

Fig. 3.6 Bank Angle Profile for Three Sample Values of σ_u

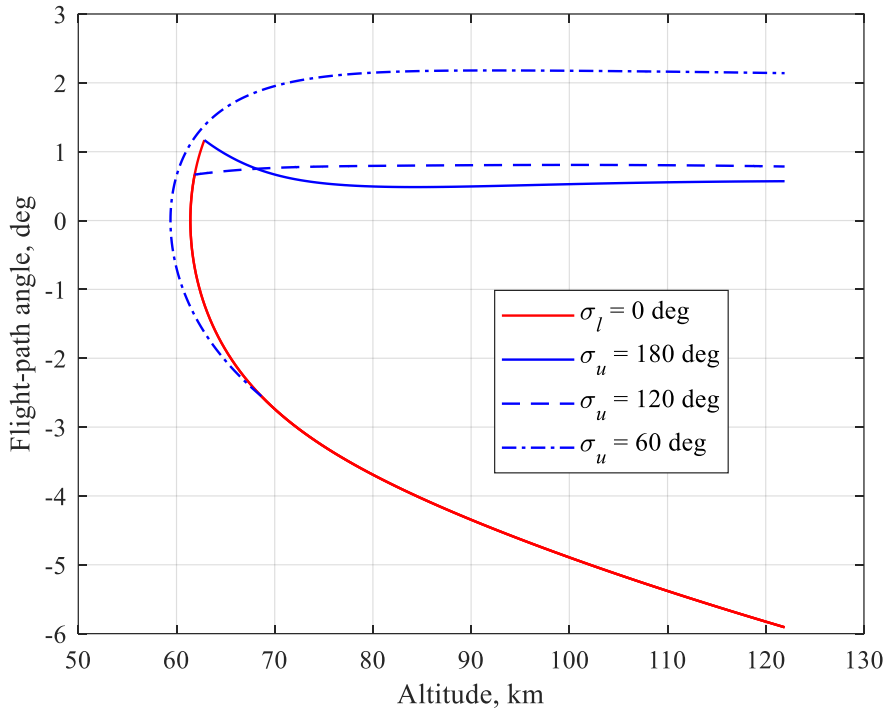

Fig. 3.7 Flight-Path Angle vs. Altitude for Three Sample Values of σ_u

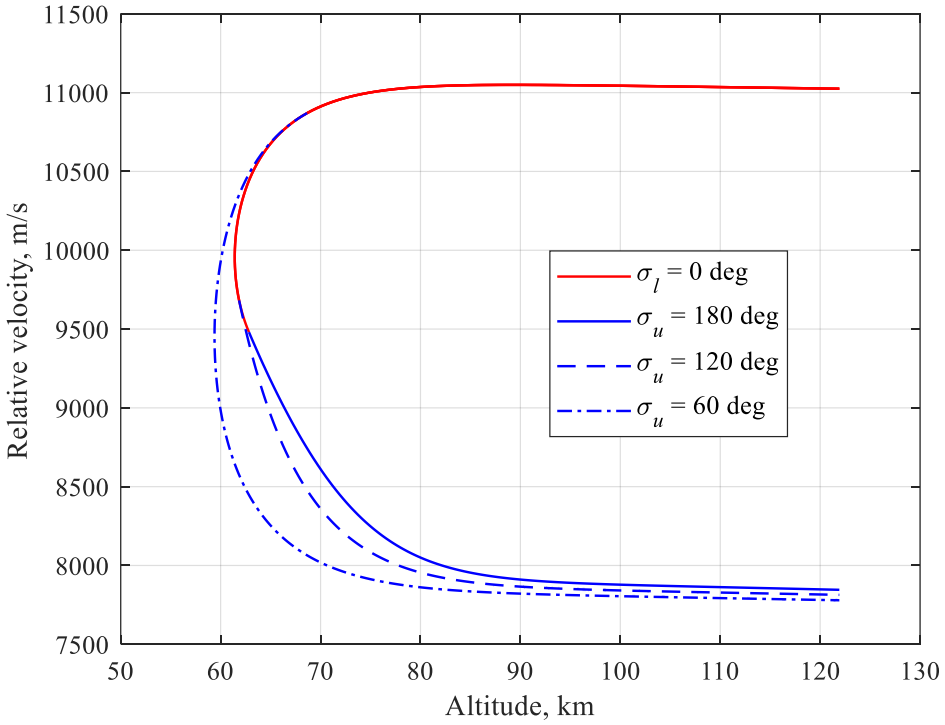

Fig. 3.8 Relative Velocity vs. Altitude for Three Sample Values of σ_u

In this chapter, optimal trajectories are achieved with instantaneous bang-bang bank angle transitions. In reality, this is not possible because of limits on the attitude dynamics. Optimal aerocapture results are presented for comparison and evaluation purposes only; the real aerocapture problem will use an on-board guidance scheme, bank angle rate and acceleration limits, and an orbital-plane target.

CHAPTER 4 – AEROCAPTURE GUIDANCE LAW

Aerocapture guidance algorithm can be separated into two phases: descent and ascent phases. Open-loop and closed-loop bank angle commands are used in descent and ascent phases, respectively, as shown in Figure 4.1.

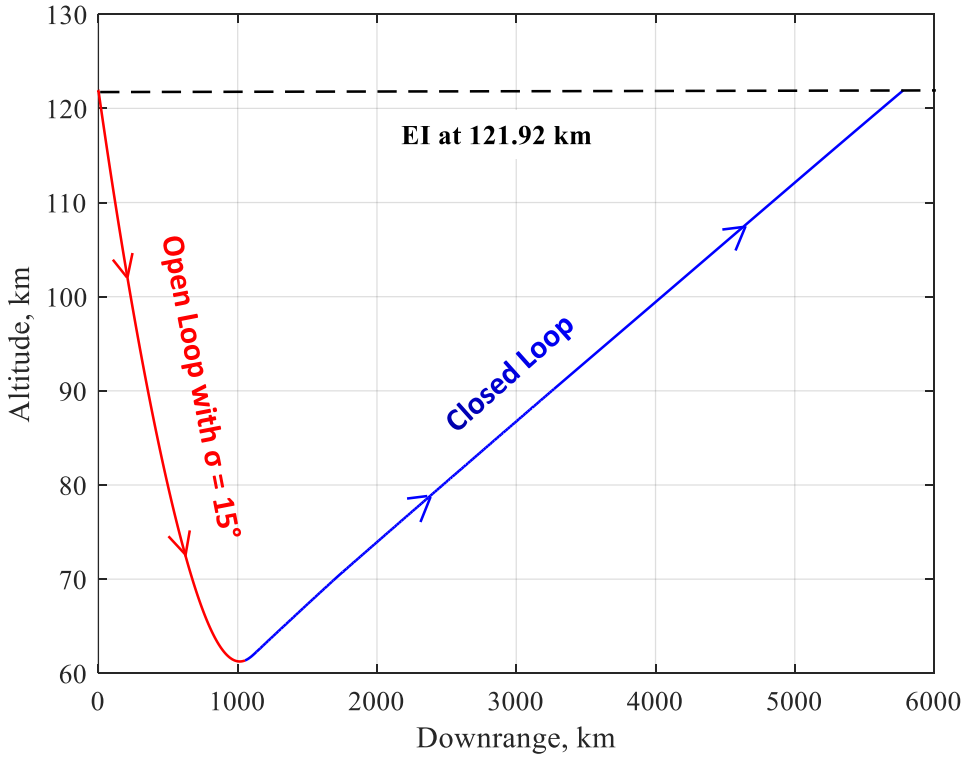

Fig. 4.1 Nominal Aerocapture Trajectory

4.1 Descent Phase

Descent phase starts at the EI and lasts until the switching point that usually occurs around the pull-up point ($\gamma = 0$). During the descent phase, the vehicle flies with a constant open-loop bank angle at 15 deg. The reason behind choosing σ = 15 deg instead of full lift-up in descent phase is that it is the same bank angle magnitude used by the Apollo entry guidance [48] and Lu et al. [30]. As discussed in chapter 3, the minimized ΔV is obtained

by following full lift-up in the descent phase and then full lift down during the ascent phase. Thus, using σ = 15 deg instead of σ = 0 in descent phase results in very little performance degradation in terms of impulsive ΔV. When the flight-path angle is greater than −0.5 deg, the guidance algorithm begins seeking the switching point. Further details about how to determine the switching point will be provided in Section 4.2.3.

4.2 Ascent Phase

4.2.1 Analytical Prediction of Atmospheric Exit Velocity

Analytical prediction of the exit state is made in the ascent phase after completing the open-loop atmospheric flight. The analytical guidance scheme is based on a simplified version of the equations of motion in a vertical plane. Since radial distance is the sum of the Earth's radius and altitude *h*, it can be said that the radial velocity and the time-rate of altitude are equal by assuming that the Earth's radius has negligible change during the aerocapture maneuver. The longitudinal equations of motion, equations (1), (4), and (5), repeated without the Earth-rotation effects and oblateness:

$$\dot{r} = \dot{h} = V \sin\gamma \tag{25}$$

$$\dot{V} = -D - \frac{\mu}{r^2}\sin\gamma \tag{26}$$

$$\dot{\gamma} = \frac{1}{V}\left[L\cos\sigma + \left(V^2 - \frac{\mu}{r} \right)\frac{\cos\gamma}{r} \right] \tag{27}$$

Altitude is used as an independent variable in the algorithm. By applying the chain-rule method for the vertical-place equations of motion (dividing equations (26) and (27) by

equation (25)), the independent variable is changed from time t to altitude h. The derivatives of velocity and flight-path angle with respect to altitude are

$$\frac{dV}{dh} = \frac{-D}{V \sin\gamma} - \frac{\mu}{Vr^2} \tag{28}$$

$$\frac{d\gamma}{dh} = \frac{1}{V^2 \sin\gamma}\left[L\cos\sigma + \left(V^2 - \frac{\mu}{r} \right)\frac{\cos\gamma}{r} \right] \tag{29}$$

It is assumed that the aerodynamic lift L and drag D, which are defined by equations (7) and (8), accelerations are measured accurately by onboard sensors. The velocity is known through navigation, and the reference area S is constant. The density, lift and drag coefficients, and mass are unknown individually due to the trajectory dispersions and modeling uncertainties; however, the combination of density, lift (or drag) coefficient, and mass can be determined from the onboard acceleration sensors. The lift and drag sensor data obtained from the descent phase allow us to create two parameters that are the products of density and lift (or drag) coefficient divided by mass. A least-squares curve-fitting scheme then processes these data. Two different scenarios, Fourier and exponential curve fitting schemes, are separately investigated to define the analytical prediction of atmospheric exit velocity.

4.2.1.1 Fourier Curve Fitting

The lift- and drag-acceleration terms, $\rho C_L/m$ and $\rho C_D/m$, are fitted using MATLAB's Curve Fitting Toolbox, `cftool`, by the 3rd order Fourier functions of altitude:

$$\frac{\rho C_L}{m} = a_0 + \sum_{n=1}^{3} a_n \cos(nhw) + b_n \sin(nhw) \tag{30}$$

$$\frac{\rho C_D}{m} = c_0 + \sum_{n=1}^{3} c_n \cos(nhw) + d_n \sin(nhw) \tag{31}$$

where a_0 and c_0 are constants, a_n and c_n are the amplitudes of the cosine waves, b_n and d_n are the amplitudes of the sine waves, and w is the frequency of the sinusoidal functions. Let us define $\sin\gamma$ as an exponential function of altitude, so that FPA vs altitude profile is comparable to the optimal bang-bang control problem for ascent phase as shown in Figure 3.1c:

$$\sin\gamma = A_0 \exp(-A_1 h) \tag{32}$$

where A_0 and A_1 are constants. The reference trajectory is based on the FPA term in equation (32). Substituting equations (8), (31) and (32) into equation (28) and neglecting the gravity term ($\mu/V\,r^2$) in equation (28) for now, the derivative of velocity with respect to altitude can be expressed as

$$\begin{aligned}\frac{dV}{dh} &= \frac{-D}{V\sin\gamma} = \frac{-\frac{1}{2}\rho V^2 \frac{S}{m} C_D}{VA_0 \exp(-A_1 h)} = \frac{-VS\frac{\rho C_D}{m}}{2A_0 \exp(-A_1 h)} \\ &= \frac{-VS\left(c_0 + \sum_{n=1}^{3} c_n \cos(nhw) + d_n \sin(nhw)\right)}{2A_0 \exp(-A_1 h)}\end{aligned} \tag{33}$$

To solve the equation (33), we can write the equation in the separated form:

$$\frac{dV}{V} = \frac{B\left(c_0 + \sum_{n=1}^{3} c_n \cos(nhw) + d_n \sin(nhw)\right)}{\exp(-A_1 h)} dh \tag{34}$$

where $B = -S/(2A_0)$ is the new constant term. Next, integrating both sides of equation (34) from the current conditions $(h_{\text{now}}, V_{\text{now}})$ to the exit conditions $(h_{\text{exit}}, V_{\text{exit}})$ yields

$$\ln\left(\frac{V_{\text{exit}}}{V_{\text{now}}}\right) = B\exp(A_1 h)\left[\frac{c_0}{A_1} + \sum_{n=1}^{3}\frac{c_n\left(nw\sin(nhw) + A_1\cos(nhw)\right) + d_n\left(-nw\cos(nhw) + A_1\sin(nhw)\right)}{n^2w^2 + A_1^2}\right]_{h_{\text{now}}}^{h_{\text{exit}}} \tag{35}$$

Solving equation (35), we obtain the *drag-only* exit velocity

$$V_{\text{exit}}^{\text{drag\_Fourier}} = V_{\text{now}}\exp\left[B\exp(A_1 h)\left[\frac{c_0}{A_1} + \sum_{n=1}^{3}\frac{c_n\left(nw\sin(nhw) + A_1\cos(nhw)\right) + d_n\left(-nw\cos(nhw) + A_1\sin(nhw)\right)}{n^2w^2 + A_1^2}\right]_{h_{\text{now}}}^{h_{\text{exit}}}\right] \tag{36}$$

Now, we can include the neglected gravity term ($\mu/V\,r^2$) to improve the estimate for exit velocity. The derivative of velocity with respect to altitude for the gravity term is

$$\frac{dV}{dh} = \frac{-\mu}{Vr^2} = \frac{-\mu}{V\left(R_E + h\right)^2} \tag{37}$$

To solve the equation (37), using the technique of separating variables:

$$VdV = \frac{-\mu}{\left(R_E + h\right)^2}dh \tag{38}$$

Integrating the both sides of this equation from the current conditions ($h_{\text{now}}, V_{\text{now}}$) to the exit conditions ($h_{\text{exit}}, V_{\text{exit}}$) yields

$$\frac{1}{2}V^2\Big|_{V_{\text{now}}}^{V_{\text{exit}}} = \frac{\mu}{R_E + h}\Big|_{h_{\text{now}}}^{h_{\text{exit}}} \tag{39}$$

The exit velocity for a drag-free environment is found as

$$V_{\text{exit}}^{\text{grav}} = \sqrt{V_{\text{now}}^2 + \frac{2\mu}{R_E + h_{\text{exit}}} - \frac{2\mu}{R_E + h_{\text{now}}}} \tag{40}$$

Equation (40) is an expression for constant total energy along a two-body orbit. Exit-velocity gravity correction is calculated by

$$\Delta V_{\text{grav}} = V_{\text{exit}}^{\text{grav}} - V_{\text{now}} \tag{41}$$

By adding the exit-velocity gravity correction ΔV_{grav} to the *drag-only* exit velocity $V_{\text{exit}}^{\text{drag}}$, we finally obtain more accurate velocity at the atmospheric exit. Thus, the analytical exit velocity for Fourier curve fitting scenario is given by

$$V_{\text{exit}}^{\text{Fourier}} = V_{\text{exit}}^{\text{drag\_Fourier}} + \Delta V_{\text{grav}} \tag{42}$$

4.2.1.2 Exponential Curve Fitting

In this scenario, the lift- and drag-acceleration terms, $\rho C_L/m$ and $\rho C_D/m$, are defined by a single-term exponential function:

$$\frac{\rho C_L}{m} = k_0 \exp(k_1 h) \tag{43}$$

$$\frac{\rho C_D}{m} = x_0 \exp(x_1 h) \tag{44}$$

where k_0, k_1, x_0, and x_1 are constants, which are obtained by MATLAB's `cftool` using the accumulated lift- and drag-acceleration data. In a similar fashion, we can substitute equations (8), (32) and (44) into equation (28) and neglect the gravity term ($\mu/V\,r^2$) in equation (28) for now, the derivative of velocity with respect to altitude is

$$\frac{dV}{dh} = \frac{-VS\,\dfrac{\rho C_D}{m}}{2A_0 \exp(-A_1 h)} = \frac{-VS\,x_0 \exp(x_1 h)}{2A_0 \exp(-A_1 h)} = \frac{-VS\,x_0 \exp\left[(x_1 + A_1)h\right]}{2A_0} \tag{45}$$

Separating variables in equation (45) yields

$$\frac{dV}{V} = C\exp\left[(x_1 + A_1)h\right]dh \tag{46}$$

where the new constant is $C = -Sx_0/(2A_0)$. Similarly, integrating both sides of equation (46) from the current conditions $(h_{\text{now}}, V_{\text{now}})$ to the exit conditions $(h_{\text{exit}}, V_{\text{exit}})$, we obtain

$$\ln\left(\frac{V_{\text{exit}}}{V_{\text{now}}}\right) = \left[\frac{C\exp\left[(x_1 + A_1)h\right]}{x_1 + A_1}\right]_{h_{\text{now}}}^{h_{\text{exit}}} \tag{47}$$

Then, solving equation (47) for the *drag-only* exit velocity yields

$$V_{\text{exit}}^{\text{drag\_Exponential}} = V_{\text{now}}\exp\left[\frac{C\left[\exp\left[(x_1 + A_1)h_{\text{exit}}\right] - \exp\left[(x_1 + A_1)h_{\text{now}}\right]\right]}{x_1 + A_1}\right] \tag{48}$$

The exit-velocity gravity correction ΔV_{grav} (41) can be added to the drag-only estimate of exit velocity by following the same procedure (equations (37-41)) employed in the previous section. Therefore, the exit velocity for exponential curve fitting scenario is expressed analytically as

$$V_{\text{exit}}^{\text{Exponential}} = V_{\text{now}}\exp\left[\frac{C\left[\exp\left[(x_1 + A_1)h_{\text{exit}}\right] - \exp\left[(x_1 + A_1)h_{\text{now}}\right]\right]}{x_1 + A_1}\right] + \Delta V_{\text{grav}} \tag{49}$$

The analytical solution for atmospheric exit velocity is now complete for both scenarios. The current states $(h_{\text{now}}, V_{\text{now}})$ is known, and the exit altitude h_{exit} is also known. Eight Fourier-series coefficients (c_0, c_n, d_n, w) and two exponential-function coefficients (x_0 and x_1) are separately required in the drag-only solutions (36) and (48). The Fourier-series and exponential-function coefficients are individually obtained by a least-squares fit of the

accumulated drag-acceleration data as measured by the vehicle's onboard sensors. During the descent phase, the onboard navigation system measures and stores drag acceleration $D = \rho V^2 S C_D/(2m)$ as a function of altitude. Using the known reference area S and velocity V (from the navigation system), the drag-acceleration term $\rho C_D/m$ can be determined and stored vs. altitude. A least-squares curve-fitting scheme then processes this data to determine the eight Fourier-series coefficients (or the two exponential-function coefficients). The ability to analytically predict exit velocity using equation (42) or (49) is now possible in the ascent phase.

The drag-only exit velocity equations (36) and (48) also need the two constants A_0 and A_1, which are required to parameterize the sine of flight-path angle as a function of altitude. Boundary value conditions can be used to solve for A_0 and A_1. We know the current FPA γ_{now}, so guessing the exit FPA γ_{exit} allows us to determine the coefficients A_0 and A_1. Taking the natural logarithm of both sides of equation (32) yields

$$\ln(\sin\gamma) = \ln\left(A_0 \exp(-A_1 h)\right) = \ln A_0 - A_1 h \tag{50}$$

For the last equation, let us define $z_{\text{now}} = \ln(\sin\gamma_{\text{now}})$, $z_{\text{exit}} = \ln(\sin\gamma_{\text{exit}})$, $q_0 = \ln(A_0)$, and $q_1 = -A_1$. Two linear simultaneous equations (corresponding current and exit conditions) can be written in matrix form as

$$\begin{bmatrix} z_{\text{now}} \\ z_{\text{exit}} \end{bmatrix} = \begin{bmatrix} 1 & h_{\text{now}} \\ 1 & h_{\text{exit}} \end{bmatrix} \begin{bmatrix} q_0 \\ q_1 \end{bmatrix} \Leftrightarrow \mathbf{Z} = H\mathbf{Q} \tag{51}$$

where **Z**, H, and **Q** represent the matrix and vectors on the left side of equation (51). Multiplying both sides by the inverse of matrix H yields

$$\begin{bmatrix} q_0 \\ q_1 \end{bmatrix} = \begin{bmatrix} 1 & h_{\text{now}} \\ 1 & h_{\text{exit}} \end{bmatrix}^{-1} \begin{bmatrix} z_{\text{now}} \\ z_{\text{exit}} \end{bmatrix} \tag{52}$$

After finding the **Q** vector, the unknown constants A_0 and A_1 are computed by

$$A_0 = \exp(q_0), \; A_1 = -q_1 \tag{53}$$

Knowledge of the atmospheric exit conditions and equations (17) and (19) are used to determine the post-aerocapture apogee altitude. Hence, exit FPA can be adjusted until the predicted apogee matches the altitude of the target circular orbit. Five trial values of exit FPA are used in the search scheme to determine five trial apogee radii. The five trial values of apogee altitude are interpolated by using cubic-spline interpolation in order to find the exit FPA that results in a post-aerocapture trajectory with an apogee that matches the target orbit altitude. This search scheme is robust because the trial exit flight-path angles are selected to ensure apogees that undershoot and overshoot the target circle. Figure 4.2 presents an example of the spline interpolation for the given trial values and apogee altitudes of the exo-atmospheric orbit h_{a0}. According to the above-shown example, the vehicle can reach the apogee altitude of 200 km with the exit flight-path angle of ~0.825 deg. The closed-loop bank command is computed from tracking the exponential function ($\sin\gamma = A_0 \exp(-A_1 h)$), which needs knowledge of current and exit flight-path angles. This predictor-corrector scheme is repeated at each guidance cycle, which has a frequency of 1 Hz.

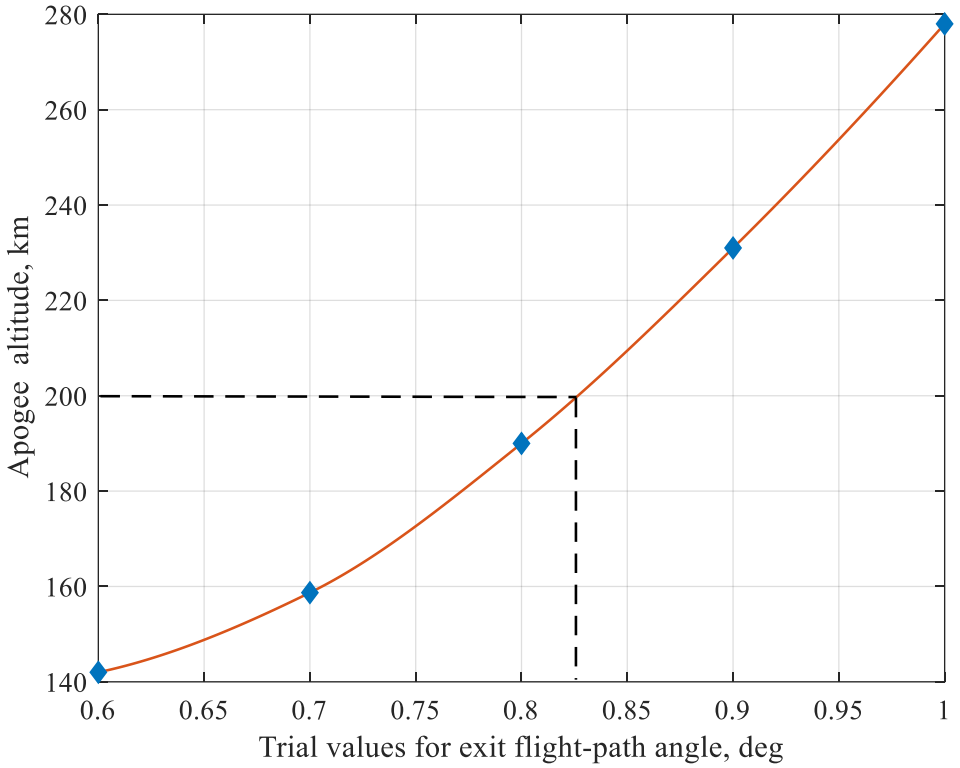

Fig. 4.2 Spline Interpolation Example for Exit Flight-Path Angle

4.2.2 Bank Angle Command

Once the atmospheric exit conditions (V_{exit} and γ_{exit}) have been found, the guidance algorithm computes the commanded bank angle for tracking the reference trajectory in the ascent phase. The refence bank profile is derived from equation (29): solving for bank angle σ, we get

$$\sigma = \cos^{-1}\left(\frac{1}{L}\left[\frac{d\gamma}{dh}V^2\sin\gamma - \left(V^2 - \frac{\mu}{r}\right)\frac{\cos\gamma}{r}\right]\right) \tag{54}$$

To compute the bank angle, equation (54) needs the derivative $d\gamma/dh$. Taking the derivative of the reference FPA term ($\sin\gamma = A_0\exp(-A_1 h)$) with respect to altitude and using the chain rule, respectively, yield

$$\frac{d(\sin\gamma)}{dh} = -A_1 A_0 \exp(-A_1 h) = -A_1 \sin\gamma \tag{55}$$

$$\frac{d(\sin\gamma)}{dh} = \frac{d(\sin\gamma)}{d\gamma}\frac{d\gamma}{dh} = \cos\gamma\frac{d\gamma}{dh} \tag{56}$$

Solving equations (55) and (56) for $d\gamma/dh$ yields

$$\frac{d\gamma}{dh} = -A_1 \tan\gamma \tag{57}$$

The commanded bank angle equation (54) also requires the lift acceleration, $L = \rho V^2 S C_L/(2m)$, where the term $\rho C_L/m$ is parameterized by either equation (30) for the Fourier curve fitting scenario or equation (43) for the exponential fitting scenario. Substituting equations (7), (30), and (57) or equations (7), (43), and (57) into equation (54), respectively, yield

$$\sigma_{\text{cmd}}^{\text{Fourier}} = \cos^{-1}\left(\frac{-A_1 V^2 \sin\gamma\tan\gamma - \left(V^2 - \frac{\mu}{r}\right)\frac{\cos\gamma}{r}}{\frac{1}{2}V^2 S\left(a_0 + \sum_{n=1}^{3} a_n \cos(nhw) + b_n \sin(nhw)\right)}\right) \tag{58}$$

$$\sigma_{\text{cmd}}^{\text{Exponential}} = \cos^{-1}\left(\frac{-A_1 V^2 \sin\gamma\tan\gamma - \left(V^2 - \frac{\mu}{r}\right)\frac{\cos\gamma}{r}}{\frac{1}{2}V^2 S\, k_0 \exp(k_1 h)}\right) \tag{59}$$

Equations (58) and (59) are the commanded bank angle of the Fourier and exponential curve fitting scenarios, respectively, for tracking the flight-path profile in the ascent phase.

4.2.3 Switching Point Criteria

Chapter 3 and Lu et al. [30] have revealed that the optimal aerocapture maneuver consists of a bang-bang bank-angle profile when attitude dynamics are ignored. Moreover, the sensitivity of the optimal aerocapture problem with respect to the bank-angle switching time has been investigated in chapter 3. In the optimal aerocapture problem, instantaneous bang-bang bank-angle transition from 0 to 180 deg occurs at the optimal switching time; however, a realistic spacecraft can change the bang angle within the limits on the attitude dynamics. Therefore, it is crucial to design a proper bank-switching algorithm.

The bank-switching strategy is based on trends observed from running several trial trajectories using the analytical predictive guidance algorithm. The best way to explain how to determine the switching point would be to use sample control profiles from these trials. Figure 4.3 shows three sample bank angle profiles (Fourier series parameterizes the drag acceleration term $\rho C_D/m$ to obtain these profiles). The switching time is varied by 0.2 s. Using the nominal density model and initial entry states, a high initial closed-loop bank angle (such as 120 deg near the pull-up altitude) is commanded by equation (58). Some time later the closed-loop bank is saturated at $\sigma = 0$ or $\sigma = 180$. Once the bank angle saturates, the vehicle flies with constant bank angle until atmospheric exit altitude. The main reason for the saturation is a combination of the loss of aerodynamic control authority with decreasing air density and the inability to track equation (32), which parameterizes $\sin\gamma$ as an exponential function of altitude. If we select the switching time too early, the saturation occurs at $\sigma = 0$ deg (lift vector is up) at an altitude of about 91 km as shown in Figure 4.3. On the other side, the switching done later causes the saturation at $\sigma = 180$ deg (lift vector is down) at an altitude of about 77 km. The velocity increment

decreases until we reach a certain switching point. After that point, the switching is delayed, and apogee altitude of the post-aerocapture and the impulsive ΔV increase. The solid curve in Figure 4.3 presents the predicted bank profile vs. altitude for the optimal switching time. The bank angle saturates at $\sigma = 180$ deg (lift vector is down) at an altitude of about 85 km. The optimal switching time leads to a total ΔV of 50.98 m/s which is only 11.4 m/s greater than the optimal single-impulse ΔV (39.6 m/s) for the bang-bang aerocapture maneuver. Note that the total ΔV for the early- and late-switching cases shown in Figure 4.3 are within 5 m/s from the nominal ΔV value.

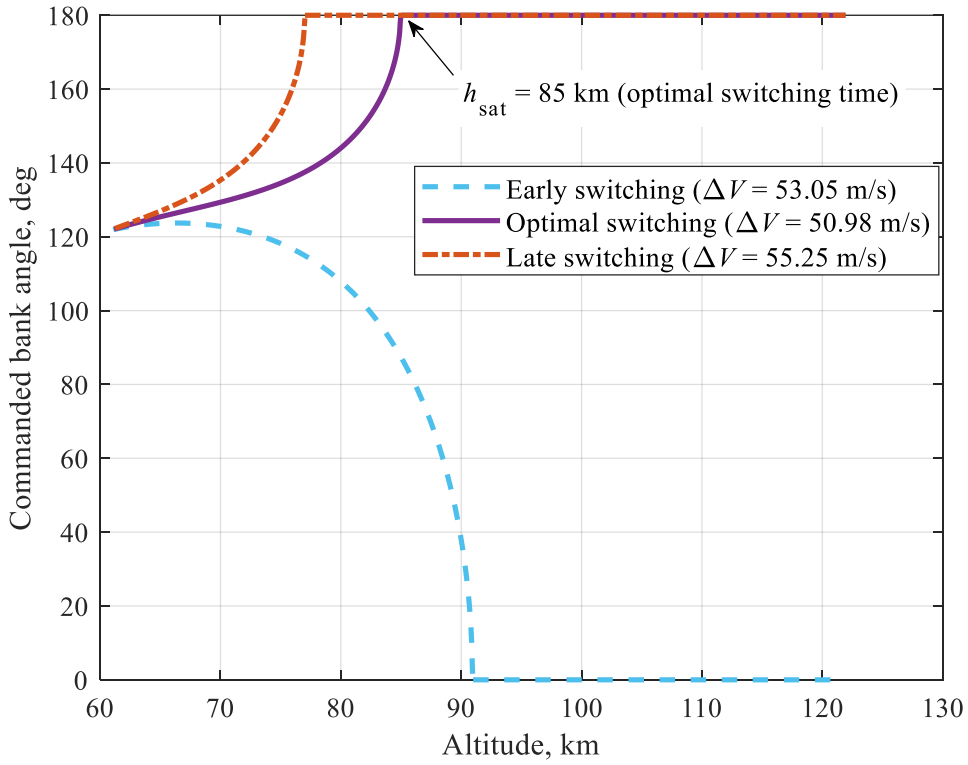

Fig. 4.3 Predicted Bank Angle Variation with Switching Point

Once the terms $\rho C_L/m$ and $\rho C_D/m$ are parameterized by either the three-term Fourier series or a single-term exponential functions at $\gamma > -0.5$ deg, the search for bank-angle

switching time begins. The predictive guidance algorithm determines the correct exit FPA and velocity to achieve the desired target apogee, and then the ascent trajectory is analytically propagated forward in altitude to determine γ and V at an altitude of 85 km. Next, the closed-loop bank angle is computed by using these propagated states in either equation (58) or (59). If the predicted bank angle saturates at $\sigma = 0$ deg at an altitude of 85 km, this means that it is still too early for the switching point time. Once the saturated bank angle command goes to 180 deg at an altitude of 85 km, the switching is initiated because it is the best time to move from the descent phase to the ascent phase to minimize the total ΔV. The bank-saturation altitude h_{sat} presented in Figure 4.3 is 85 km for the optimal switching time with nominal *L/D* = 0.27.

Additional bank-switching point analysis are executed to observe the effect of *L/D* ratio on the bank-saturation altitude. Seven trial values are selected in a range between low (0.22) and high (0.32) for *L/D* ratios. The optimal bank profiles and the corresponding bank saturation altitudes are determined for these trials. The relationship among the seven data indicated by black diamonds in Figure 4.4 is nearly linear. Thus, a linear model is generated for h_{sat} by taking advantage of a linear least-squares method. The switching point of the guidance algorithm is determined by evaluating the bank command at a predefined altitude based on a linear function of the *L/D* ratio:

$$h_{\text{sat}} = H_0 + H_1(L/D) \tag{60}$$

where coefficients are found as H_0 = 103.3 km and H_1 = –68.571 km. Again, the guidance algorithm initiates the bank-switching process when the commanded bank angle computed

by either equation (58) or (59) saturates at 180 deg at an altitude of h_{sat}, equation (60), (recall that *L/D* ratio is known thanks to onboard sensors).

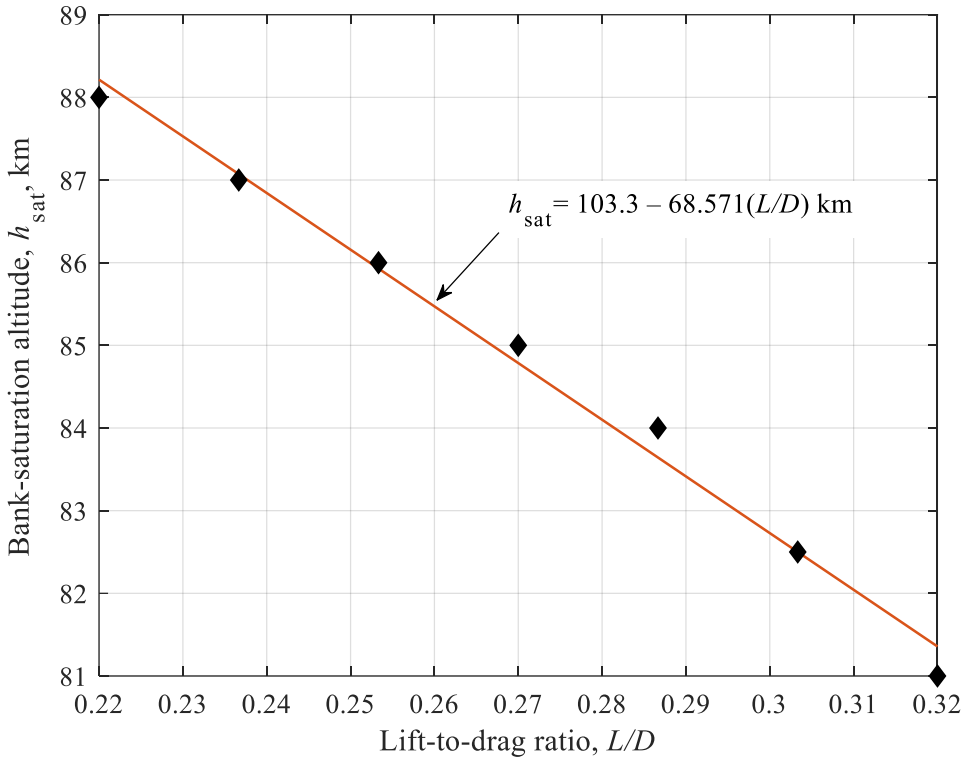

Fig. 4.4 Linear Least-Square Fitting for h_{sat}

4.2.3.1 Propagation of Bank Maneuver

The bank maneuver from the open-loop bank at 15 deg to the initial closed-loop bank around 120 deg (which based on an analytical flight profile) takes about 8.5 s with the bank-angle rate limit of 15 deg/s and acceleration limit of 5 deg/s^2. The bank-attitude dynamics should be included in the aerocapture guidance to better predict the switching point. Therefore, when searching the bank-switching point, a second-order Euler integration method is used to propagate the states h, V, γ ahead in time as the bank angle rotates from 15 deg to 120 deg using the maximum acceleration and rate limits:

$$h(t+\Delta t) \approx h(t) + \dot{h}(t)\Delta t + 0.5\ddot{h}(t)\Delta t^2 \tag{61}$$

$$V(t+\Delta t) \approx V(t) + \dot{V}(t)\Delta t + 0.5\ddot{V}(t)\Delta t^2 \tag{62}$$

$$\gamma(t+\Delta t) \approx \gamma(t) + \dot{\gamma}(t)\Delta t + 0.5\ddot{\gamma}(t)\Delta t^2 \tag{63}$$

where Δt is the step size, $h(t)$, $V(t)$, and $\gamma(t)$ are the current state values, $\dot{h}(t)$, $\dot{V}(t)$, and $\dot{\gamma}(t)$ are the first-time derivatives of the states, and $\ddot{h}(t)$, $\ddot{V}(t)$, and $\ddot{\gamma}(t)$ are the second-time derivatives. A single time step Δt = 8.5 s is used in the integration method to estimate the roll maneuver. The vertical-plane equations of motion, equations (25-27), are simplified once again by making some assumptions: neglecting the gravity term ($\mu \sin\gamma / r^2$), $\cos\gamma = 1$ (for small flight-path angles), r is constant, and σ is taken as 60 deg (an average bank angle is used). Upon the simplifications, the first-time derivatives of the states become

$$\dot{h}(t) = V \sin\gamma \tag{64}$$

$$\dot{V}(t) = -D \tag{65}$$

$$\dot{\gamma} = \frac{1}{V}\left[L\cos\sigma + \left(\frac{V^2}{r} - \frac{\mu}{r^2} \right) \right] \tag{66}$$

To take the second derivatives, equations (65) and (66) need a density model, so the terms $\rho C_L/m$ and $\rho C_D/m$ in lift and drag accelerations (using a small amount of accumulated lift and drag acceleration data near pull-up) are parameterized by a single-term exponential functions of altitude:

$$\frac{\rho C_L}{m} = M_0 \exp(M_1 h) \tag{67}$$

$$\frac{\rho C_D}{m} = N_0 \exp(N_1 h) \tag{68}$$

where M_0, M_1, N_0, and N_1 are constants. Substituting equations (67) and (68) into equations (65) and (66), and then taking the second-time derivatives yields

$$\ddot{h}(t) = -D \sin\gamma + \dot{\gamma} V \cos\gamma \tag{69}$$

$$\ddot{V}(t) = \frac{2D^2}{V} - \dot{h} N_1 D \tag{70}$$

$$\ddot{\gamma}(t) = \left(\dot{h} M_1 - \frac{D}{V} \right) \frac{L \cos\sigma}{V} - \left(1 + \frac{\mu}{r V^2} \right) \frac{D}{r} \tag{71}$$

Finally, we can compute the first and second derivatives using current states. The second-order Euler integration method (with a step size of 8.5 s) finds the predicted states at the end of the bank maneuver (15 to 120 deg) from current state. Using this approximate state (h, V, γ at $t + \Delta t$), the analytical guidance method selects correct exit conditions first and then checks the bank angle command at the predefined h_{sat}. If the bank angle has the desired value, then the switch point has been determined.

4.2.4 Bank Angle Reversal Criteria

Inclination *i* is the dihedral angle between the equatorial plane and the orbital plane, and it varies from 0 to 180 deg. The inclination is one of the six classical orbital elements [45]. It can be computed using the angular momentum vector **h (**which is the cross product of inertial position vector $\mathbf{r}_i$ and inertial velocity vector $\mathbf{V}_i$):

$$\cos i = \frac{\mathbf{K}\cdot\mathbf{h}}{\|\mathbf{h}\|} \tag{72}$$

where **K** is the unit vector in the positive direction of Earth's north polar axis. In this study, the angular momentum vector at EI is in the equatorial plane (i.e., $h_z = \mathbf{K}\cdot\mathbf{h} = 0$ with an initial heading angle of 0 deg), so the initial inclination is computed as 90 deg from equation (72). The target orbital inclination is taken as $i_{\mathrm{tgt}} = 88$ deg, as used in reference [30].

Bank angle magnitude other than 0 deg (lift vector is up) or 180 deg (lift vector is down) induces inclination changes during the aerocapture maneuver. Therefore, one bank-reversal maneuver is required to correct the plane change in the atmospheric flight phase. The bank-reversal logic is based on the search for the intermediate inclination where a bank-reversal would result in exit conditions with an inclination of 88 deg. The closed-loop predictive guidance algorithm is run for this search scheme. Using trial-and-error, the intermediate inclination is determined for starting the bank reversal maneuver so that the inclination meets the target value of 88 deg at the end of the atmospheric flight. Figures 4.5 and 4.6 present the inclination and bank angle profiles for three sample minimum-ΔV aerocapture trajectories with low, nominal, and high L/D ratios. These trajectories are determined by numerically integrating the complete equations of motion, equations (1-6), with Earth-rotation effects, oblateness, and roll dynamics. Red and blue curves in Figures 4.5 and 4.6 indicate open-loop ($\sigma = 15$ deg) and closed-loop guidance (the bank angle command is obtained by using the tracking control law in the analytical guidance scheme) phases, respectively. The switching and bank-reversal points are apparent in Figures 4.5 and 4.6. The lift-to-drag ratio has a direct impact on the bank-reversal inclination

overshoot of the target inclination. Decreasing L/D ratio diminishes the inclination overshoot of the target value because the vehicle has less control authority which results in less change in inclination. To complete the bank reversal maneuver from approximately 130 deg to –130 deg as shown in Figure 4.6, the vehicle performs clockwise rotation in the quickest way without exceeding the limits on the attitude dynamics. Feedback control system is not active during the bank reversal. By following the reference bank angle profiles in Figure 4.6, the vehicle achieves the desired apogee altitude of 200 km with the desired 88-deg inclination.

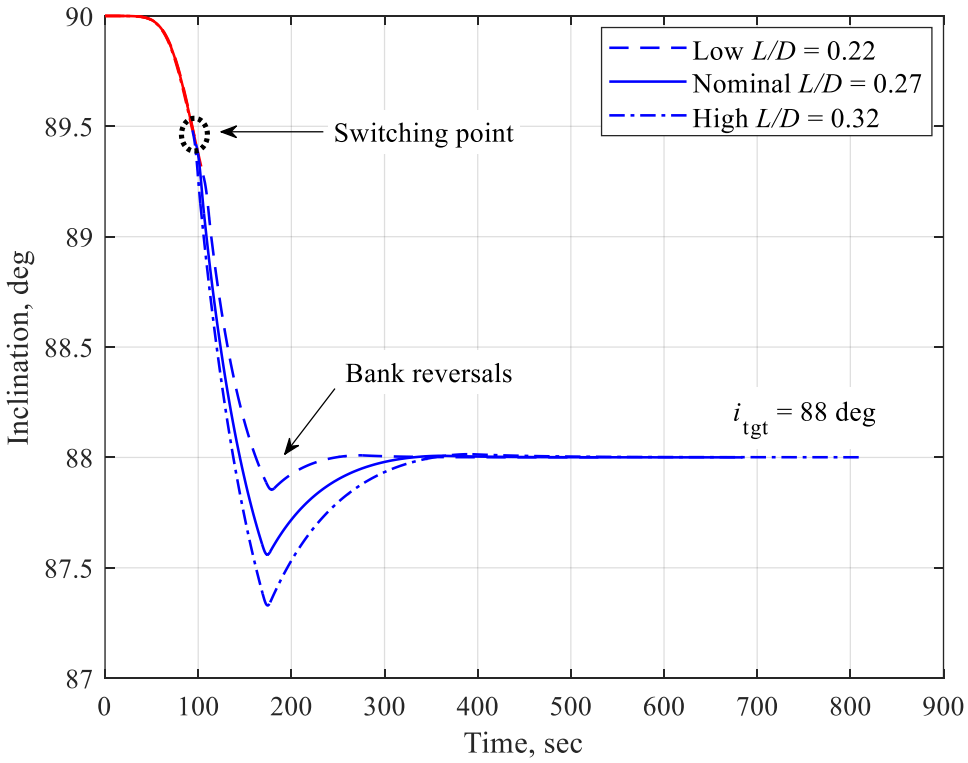

Fig. 4.5 Inclination Time History for Three Sample L/D Ratios

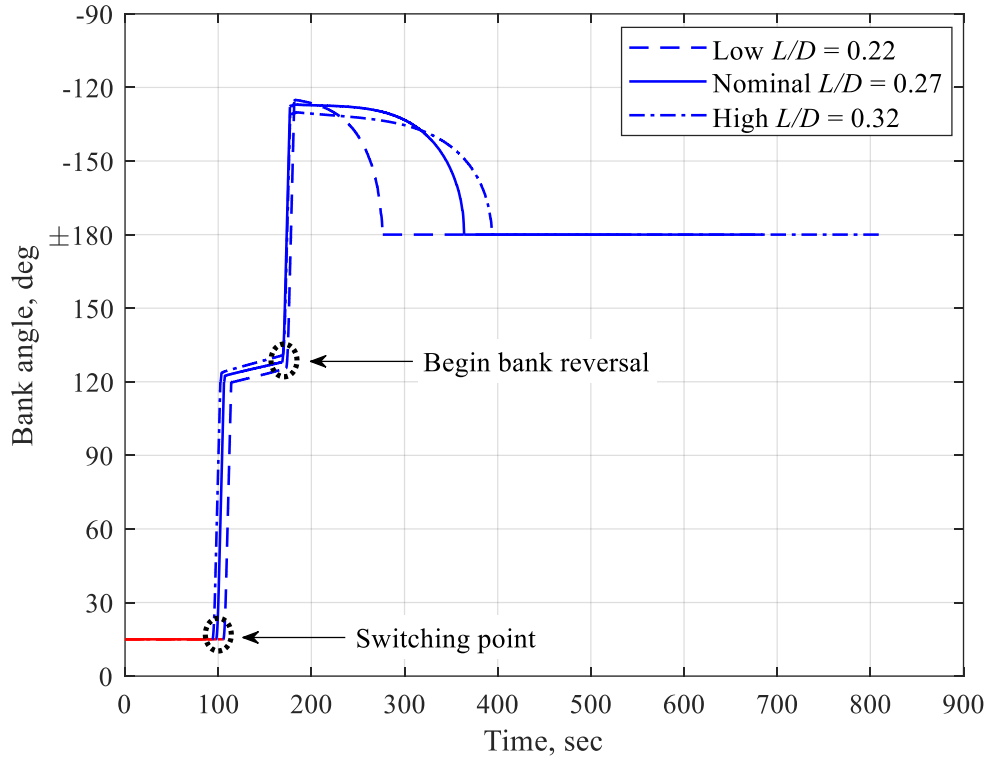

Fig. 4.6 Bank Angle Time History for Three Sample L/D Ratios

In a similar way to the switching point criteria, additional bank-reversal point analysis has been implemented for seven trial values of *L*/*D* ratio. These values are chosen between low (0.22) and high (0.32) for *L*/*D* ratio. Figure 4.7 shows the bank-reversal inclination i_{rev} values for these seven trials, and that a simple linear model fits the data (*L*/*D*, i_{rev}) quite well. Therefore, the bank-reversal inclination i_{rev} is determined from a least-square fit:

$$i_{\text{rev}} = I_0 + I_1(L/D) \tag{73}$$

where coefficients are I_0 = 88.9682 deg and I_1 = –4.9884 deg. A single bank reversal is performed when the current orbital inclination crosses the bank-reversal inclination i_{rev} threshold. As *L*/*D* ratio increases, i_{rev} values decrease linearly.

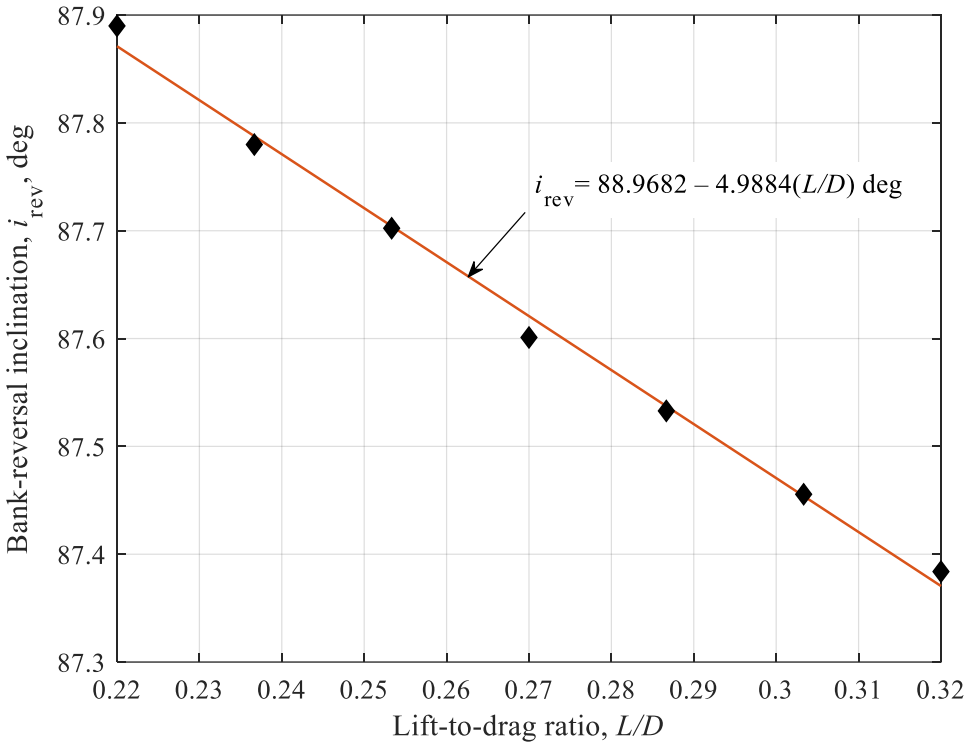

Fig. 4.7 Linear Least-Square Fitting for i_{rev}

Figure 4.8 presents the flowchart of the APC guidance method. The flowchart begins with open-loop aerocapture phase at the atmospheric entry. Right after the terms $\rho C_L/m$ and $\rho C_D/m$ in equations (7) and (8) are parameterized by either the Fourier or exponential functions at $\gamma = -0.5$ deg, the guidance algorithm makes the first decision on the bank-switching condition. If the commanded bank angle saturates at 180 deg at a predefined altitude h_{sat}, the closed-loop aerocapture phase starts. The second decision of the guidance algorithm is the bank-reversal maneuver. If the current orbital inclination i is less than or equal to the bank-reversal inclination i_{rev}, the bank-reversal logic commands a reversal maneuver. Then the bank angle is computed using the tracking control law for the remainder of the ascent phase. To establish the desired target orbit, the total ΔV and orbital inclination are determined at the atmospheric exit.

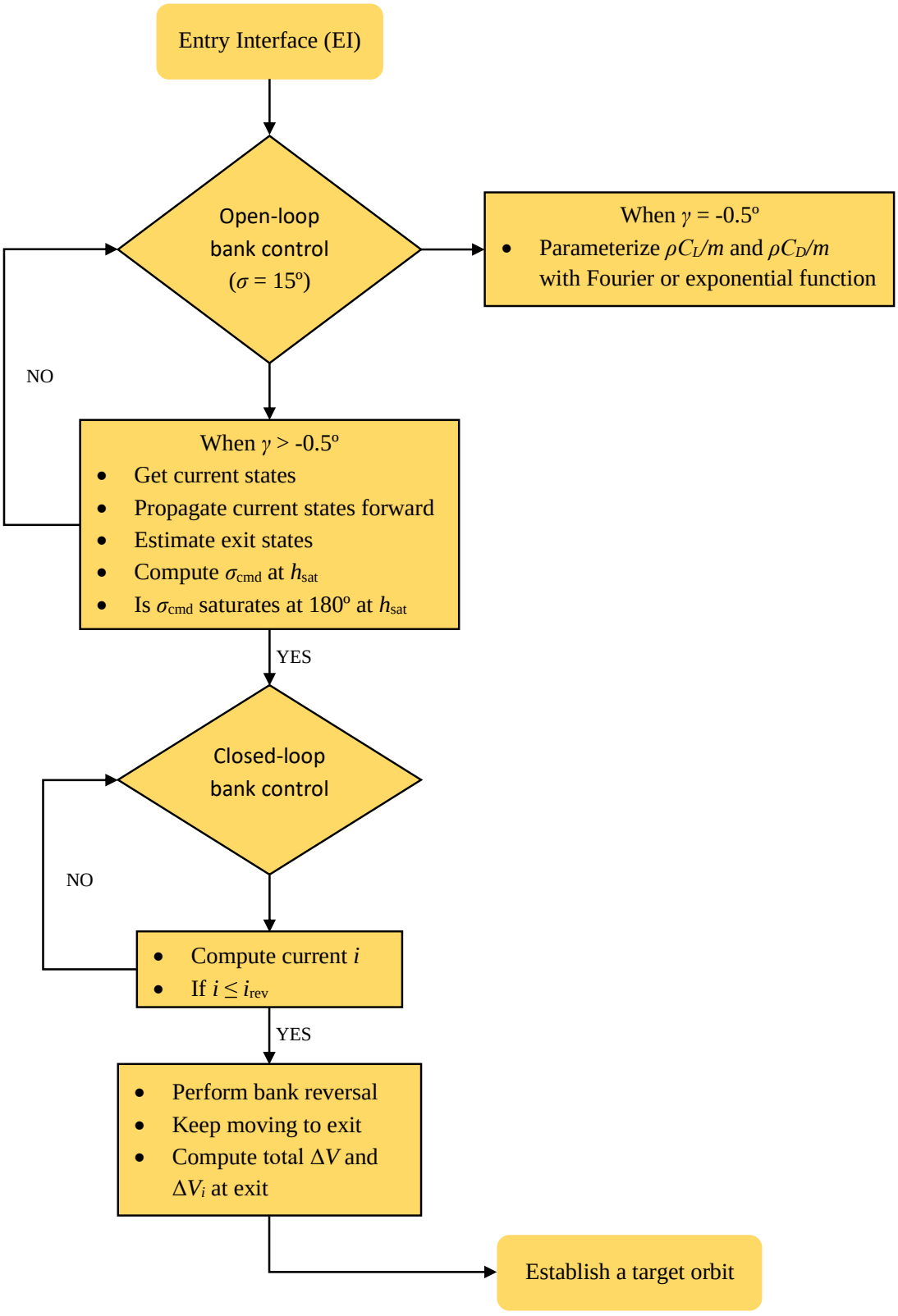

Fig. 4.8 Schematic Flowchart of Analytical Aerocapture Guidance

CHAPTER 5 – NUMERICAL RESULTS

5.1 Monte-Carlo Dispersions

5.1.1 Vehicle Dispersions

The only three vehicle parameters (lift coefficient, drag coefficient, and mass of the vehicle) are dispersed in the Monte-Carlo simulations. Recall that there is almost no change in the lift and drag coefficients at very high Mach numbers, so they are considered to be constant along the aerocapture trajectory. Table 5.1 shows the dispersions in the vehicle parameter. While the normal distributions (with zero mean) are used for lift and drag coefficients, C_L and C_D, the dispersions for vehicle mass are uniformly distributed with a range from 8534.2 kg to 9432.6 kg. Note that the 15% 3σ dispersions for aerodynamic coefficients used in Ref. [29] are increased to 20% for this study.

Table 5.1: Vehicle Dispersions for the Monte-Carlo Simulation

Parameter	Nominal value	Distribution	Dispersion
Lift coefficient	0.3699	Gaussian	$3\sigma = 0.07398(20\%)$
Drag coefficient	1.37	Gaussian	$3\sigma = 0.274(20\%)$
Mass	8983.4 kg	Uniform	$\pm 5\%$

5.1.2 Entry State Dispersions

Initial states (longitude, latitude, velocity, flight-path angle, and heading angle) are randomly distributed in the Monte-Carlo simulations. Note that the entry interface altitude is not a random variable because it is the trigger for aerocapture trajectory. Table 5.2 presents the nominal values and dispersions in the initial state. Gaussian distributions with

zero mean are applied to the entry states. It should be pointed out that 3σ dispersions for the initial states implemented in Ref. [29] are doubled for this study.

Table 5.2: Inertial Entry State Dispersions for the Monte-Carlo Simulation

State	Nominal value	Distribution	Dispersion
Altitude (km)	121.92	NA	NA
Longitude (deg)	-116.5	Gaussian	$3\sigma = 0.4$
Latitude (deg)	-46.67	Gaussian	$3\sigma = 0.4$
Velocity (km/s)	11.02	Gaussian	$3\sigma = 0.06$
Flight-path angle (deg)	-5.91	Gaussian	$3\sigma = 0.02$
Heading angle (deg)	0.00	Gaussian	$3\sigma = 0.1$

5.1.3 Atmospheric Density Dispersions

Air density is often regarded as the most effective factor for the accuracy of the aerocapture guidance algorithm because the air density is not uniform all over the Earth. During the atmospheric flight phase, the lift and Drag accelerations directly depend on the air density. Small errors in atmospheric density model, especially at lower altitudes, can result in significant errors in targeting exit conditions. In this study, the 1976 US Standard Atmosphere is used for the nominal density model. Nominal atmospheric density model is perturbed by Earth Global Reference Atmospheric Model (Earth GRAM 2010) [49]. Figure 5.1 shows the ratio of the dispersed density model to the nominal density model for altitudes between 50 and 121.92 km. Because the vehicle's lowest pull-up altitude is around 60 km, Figure 5.1 only presents the density ratios for altitudes above 50 km. While

the relative atmospheric dispersions at higher operating altitudes are between $\pm 60\,\%$, these values are less than 30% at the lower altitudes.

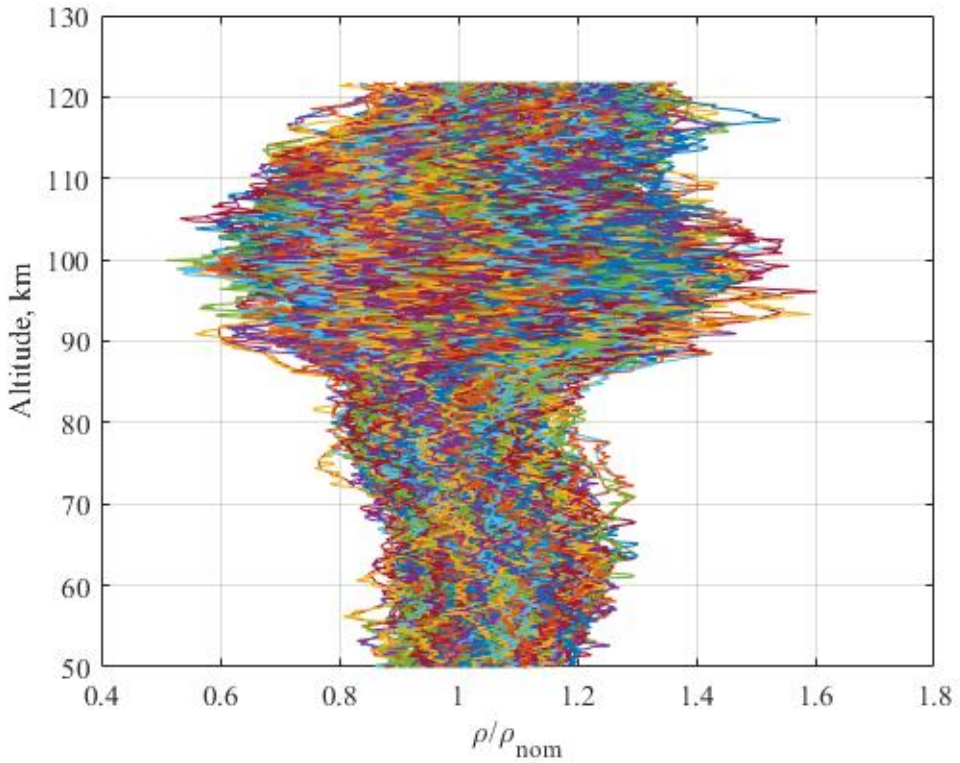

Fig. 5.1 Ratio of GRAM 2010 Dispersed Density Relative to US 1976 Standard Atmosphere

Atmospheric density in the GRAM 2010 perturbed density model is only a function of altitude. In addition to the GRAM 2010 density perturbations, a small random variation should be added to the density during the ascent phase so that the density varies with longitude and latitude as well as altitude. The density during the ascent phase at altitude h, $\rho_A(h)$, is obtained by multiplying the (GRAM 2010 dispersed) density for the descent phase $\rho_D(h)$ at altitude h with an exponentially growing sinusoidal multiplier:

$$\rho_A(h) = \rho_D(h)\left[1 + G_1 \exp\left(G_2\left(h - h_{\text{PU}}\right)\right)\sin\left(\Omega\left(h - h_{\text{PU}}\right)\right)\right] \tag{74}$$

where h_{PU} is the pull-up altitude, G_1 and G_2 are constants, and Ω is the frequency of the sine function. Coefficients G_1 and G_2 are determined from random values for the ascent-to-descent density ratios, (ρ_A/ρ_D), at exit altitude and at the midway altitude between pull-up and exit. Evaluating the amplitude of sine function in equation (74) at exit altitude and at the midway altitude between pull-up and exit produces a set of exponential equations

$$G_1 \exp\left(G_2\left(h_{\mathrm{exit}} - h_{\mathrm{PU}}\right)\right) = C_1 \tag{75}$$

$$G_1 \exp\left(G_2\left(h_{\mathrm{mid}} - h_{\mathrm{PU}}\right)\right) = C_2 \tag{76}$$

where C_1 and C_2 are random variables with unity mean and a uniform dispersion of ± 0.1 for C_1, while a uniform dispersion of 20-30% of C_1 for C_2. Solving equations (75) and (76) for G_1 and G_2 yields

$$G_2 = \frac{\ln\left(\frac{C_1}{C_2}\right)}{h_{\mathrm{exit}} - h_{\mathrm{mid}}} \tag{77}$$

$$G_1 = C_1 \exp\left(-G_2\left(h_{\mathrm{exit}} - h_{\mathrm{mid}}\right)\right) \tag{78}$$

The frequency of the sine function Ω is uniformly distributed with limits that correspond to one-quarter and two cycles during the ascent phase (the sign of frequency is also random). Figure 5.2 shows the ascent-to-descent density ratios for 1000 Monte-Carlo simulations. The density ratio is between $\pm$ 10% at exit, and this ratio is less than 3% at the midway altitudes. Equation (74) models density deviations between the descent and ascent paths at a common altitude, e.g., density variations with latitude and longitude.

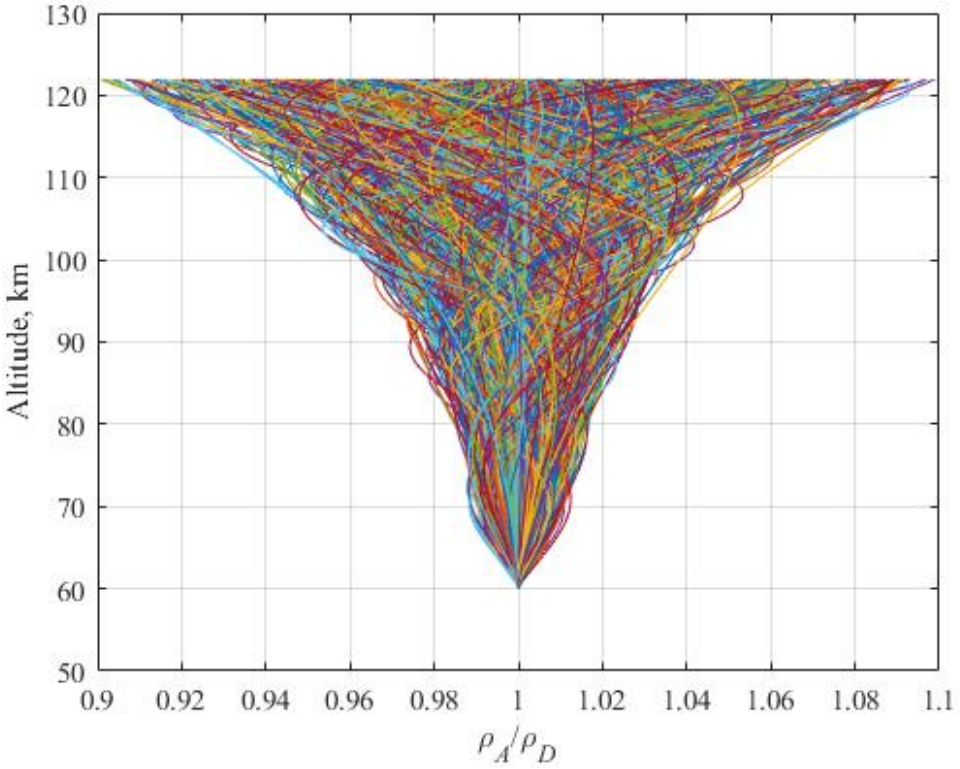

Fig. 5.2 Ratio of Ascent Density to Descent Density

5.2 Scenario 1 – Fourier Curve Fitting Simulation Results

Closed-form solutions for exit velocity in the first scenario are obtained by using Fourier curve fitting method as described in section 4.2.1.1. A three-term Fourier series with altitude as the independent variable is used to parameterize the terms $\rho C_L/m$ and $\rho C_D/m$ in equations (7) and (8). Nominal and off-nominal (Monte-Carlo) results for scenario 1 will be provided in this section.

5.2.1 Nominal Results for Scenario 1

A nominal guided aerocapture trajectory is achieved by using the nominal vehicle parameters (see Table 2.1), entry states (see Table 3.1), and density model (US 1976 Standard Atmosphere). The accumulated lift- and drag-acceleration data from EI to $\gamma =$

-0.5 deg are nondimensionalized by a scaling factor of 10^8 m^3 and the accumulated altitude data is nondimensionalized by a scaling factor of 60 km^{-1}. At $\gamma = -0.5$ deg, a nonlinear least-squares fitting technique is performed to fit three-term Fourier models to the dimensionless lift- and drag-acceleration data, respectively. The least-square solution for each data is done only once during the atmospheric flight phase. Table 5.3 presents the coefficients gained from fitting three-term Fourier models for the dimensionless $\rho C_L/m$ and $\rho C_D/m$ vs. dimensionless altitude data. CPU time required for the nonlinear least-squares solver is computed by MATLAB's `tic/toc` command as 0.6 s. Recall that the switching to the closed-loop guidance is always several seconds after the pull-up point ($\gamma > 0$ deg). The computer used for analyses in this research has following system specifications:

- Intel® Core™ i7-7700HQ CPU @ 2.8 GHz
- 8 GB RAM
- 64-bit Operating System
- Windows 10 Home

Figures 5.3 and 5.4 show the accumulated dimensionless data and Fourier-fit curves for dimensionless altitudes between 1.025 (≡61.5 km) and 2.032 (≡121.92 km). According to goodness-of-fit statistics, R-squared values for both fitted curves are 1, which indicates perfect fit.

Table 5.3: Nominal Fourier-Series Coefficients for Scenario 1

Data	Coefficients	Value
$\rho C_L/m$ vs. altitude	a_0	2.81245×10^5
	a_1	-3.72257×10^5
	a_2	0.94075×10^5
	a_3	-0.02874×10^5
	b_1	1.98375×10^5
	b_2	-1.39991×10^5
	b_3	0.27947×10^5
	w	-0.29322
$\rho C_D/m$ vs. altitude	c_0	2.00061×10^6
	c_1	-2.71638×10^6
	c_2	0.76686×10^6
	c_3	-0.05039×10^6
	d_1	1.27475×10^6
	d_2	-0.92285×10^6
	d_3	0.19342×10^6
	w	-0.26275

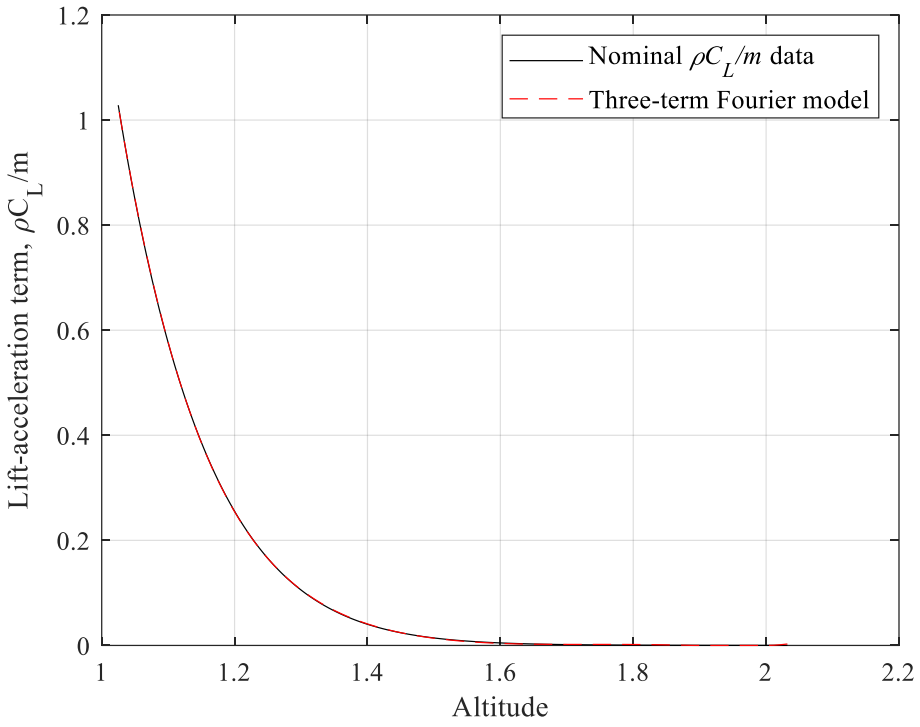

Fig. 5.3 Curve Fit on Dimensionless $\rho C_L/m$ vs Altitude for Scenario 1

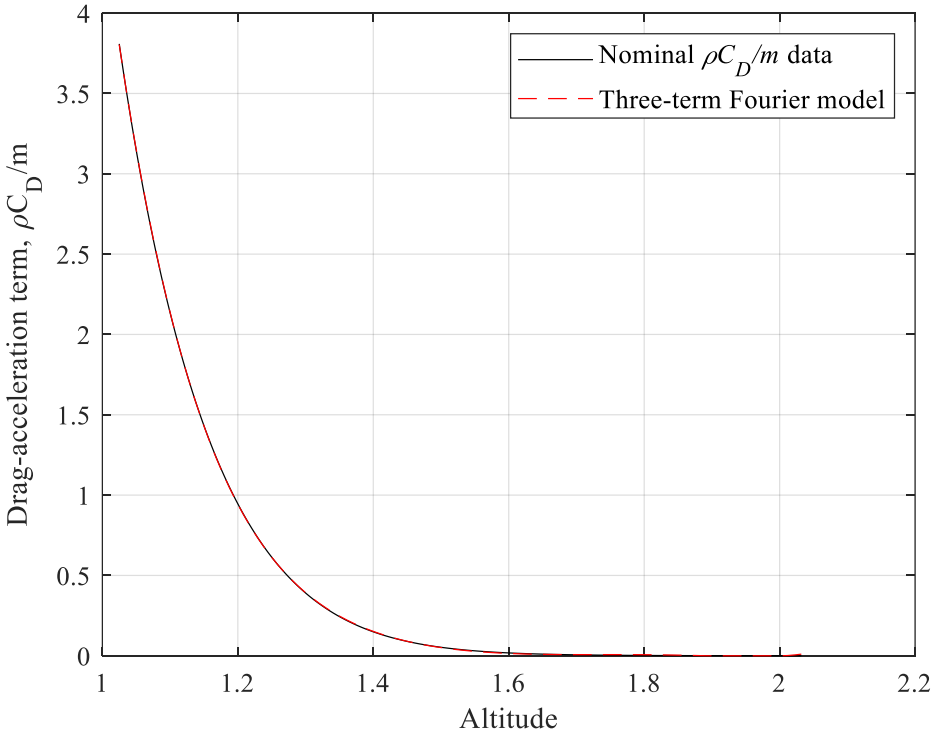

Fig. 5.4 Curve Fit on Dimensionless $\rho C_D/m$ vs Altitude for Scenario 1

Figures 5.5 and 5.6 present the nominal trajectory simulation results for inclination and bank angle profiles, respectively. These two profiles are the same as those shown for $L/D = 0.27$ in Figures 4.5 and 4.6. Initiation of the bank-switching from open-loop to closed-loop control is 97.7 s, which is about 4 seconds after the pull-up time. Closed-loop bank command usually varies between +120 and +130 deg until a single bank reversal is initiated at $i = 87.6$ deg. Due to "right turn" atmospheric flight with the positive bank angle, inclination angle decreases from 90 to 87.56 deg until the bank angle reaches to full lift-down position ($\sigma = 180$ deg). "Left turn" flight provides to increase the decreasing inclination angle to the target value of 88 deg. Because the nominal apogee altitude of the exo-atmospheric trajectory is 200.12 km, the vehicle requires a total of two coplanar velocity increments of 49.04 m/s.

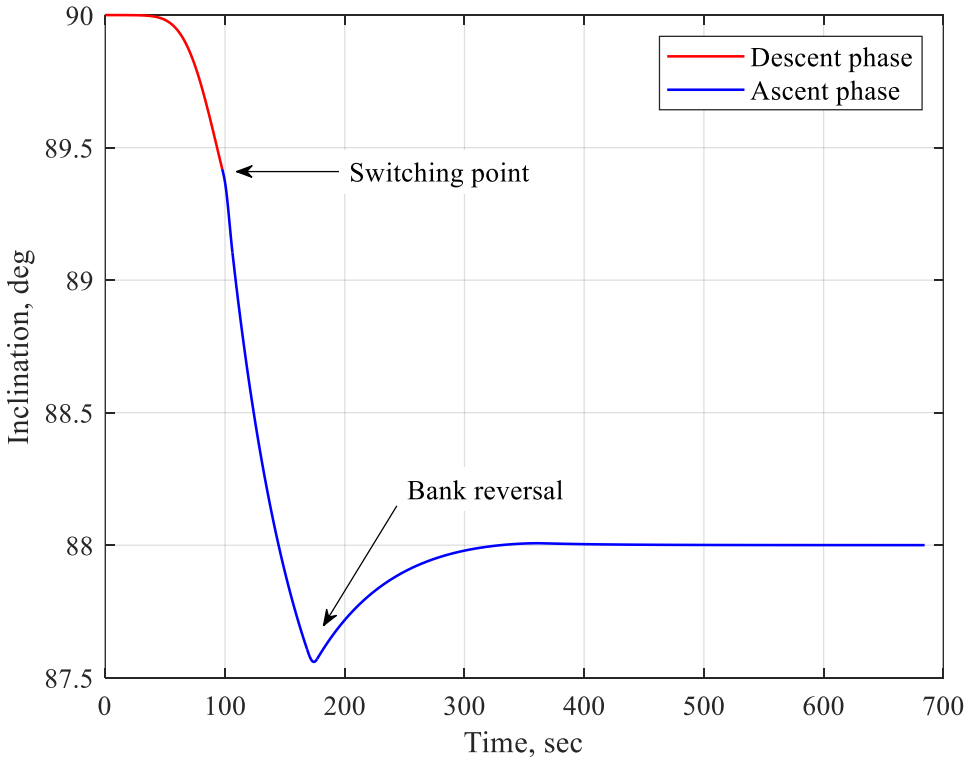

Fig. 5.5 Nominal Inclination Time History for Scenario 1

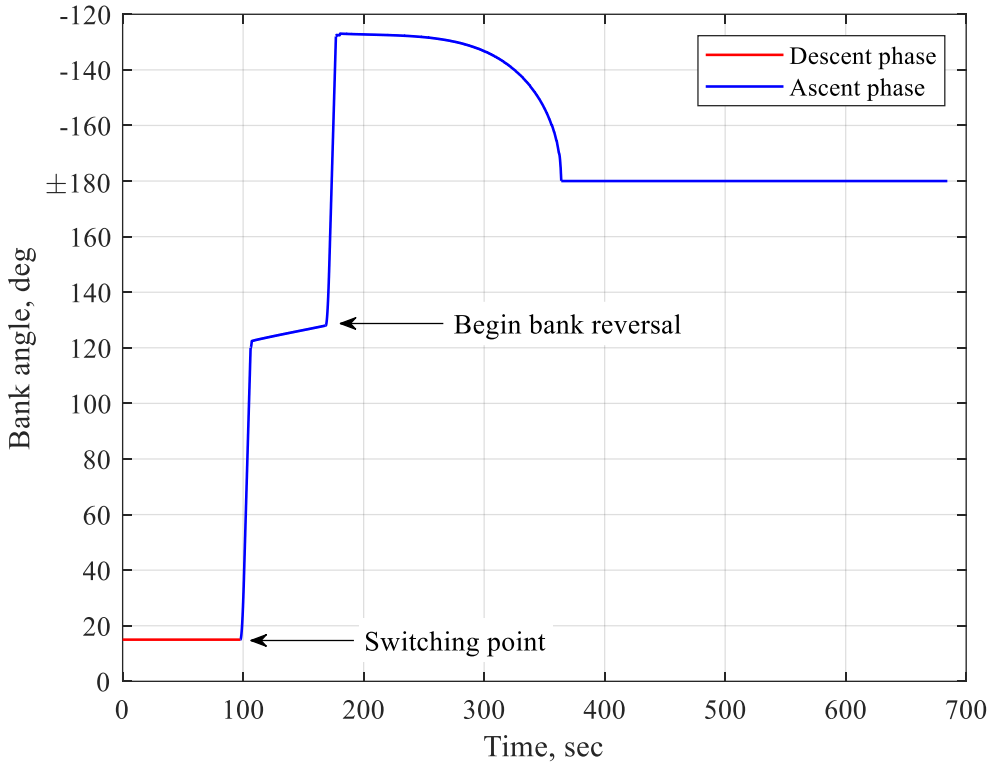

Fig. 5.6 Nominal Bank Angle Time History for Scenario 1

Figure 5.7 represents the latitude and longitude coordinates of the spacecraft between atmospheric entry and exit locations. The spacecraft enters the atmosphere at a latitude of 46.67º S and a longitude of 116.5º W. The latitude and longitude of spacecraft's ground track at atmospheric exit are 4.43º N and 117.67º W as seen in Figure 5.7. Since the heading angle is around the zero during the atmospheric flight phase, spacecraft's longitude only changes less than 1.2º, while its latitude ranges from 46.67º S to 4.43º N.

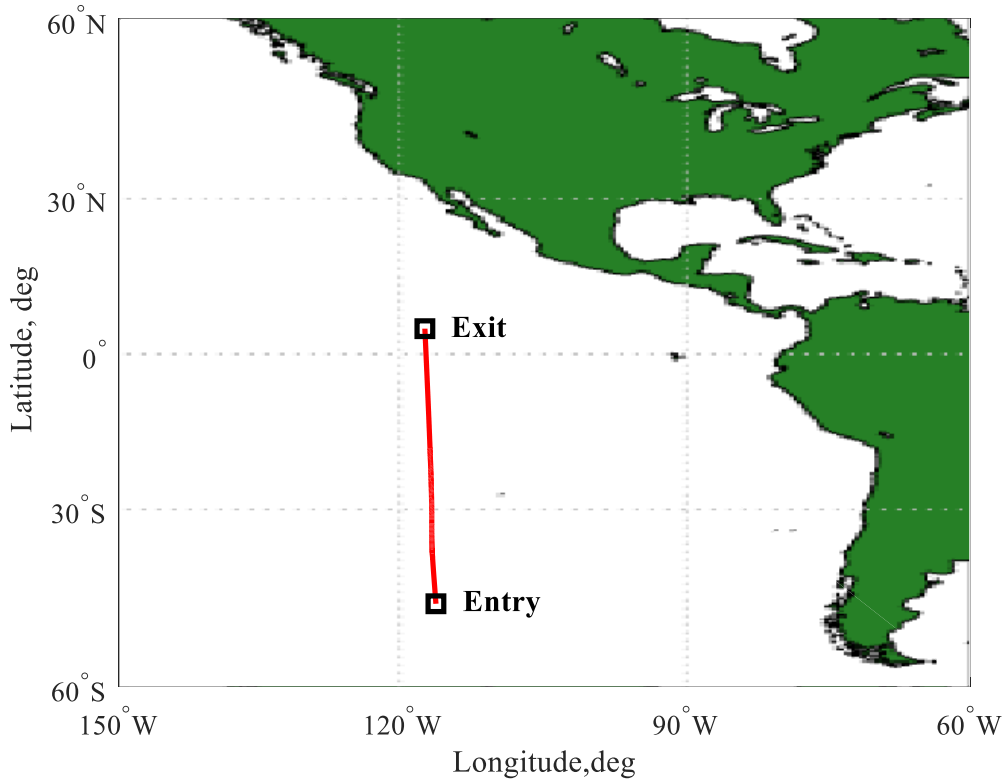

Fig. 5.7 Ground Track of Atmospheric Flight Phase for Scenario 1 on a Mercator Map

5.2.2 Monte-Carlo Simulation Results for Scenario 1

Dispersions described in section 5.1 for vehicle parameters, initial states, and atmospheric density are applied to the nominal model. For the first scenario, 1000 Monte-Carlo simulations are executed to evaluate aerocapture robustness. Figures 5.8 and 5.9 show the Monte-Carlo simulation results of the flight-path angle and relative velocity vs. altitude for scenario 1. For the remainder of the figures, red curves indicate open-loop aerocapture phase and blue curves closed-loop aerocapture phase. Switching from open-loop to closed-loop bank control typically happens at flight-path angles between 0.5 and 1.6 deg and the exit FPA range is between 0.5 and 1.3 deg as seen in Figure 5.8. The FPA range at the bank-switching position depends on the *L*/*D* ratio range in the simulations. As *L*/*D* ratio

decreases, the bank-switching time increases, so does the FPA at the switching point. Figure 5.9 shows that the speed is reduced by about 30% from entry interface (EI) to exit. The majority of the speed reduction takes place in a narrow 15-km altitude band between 75 and 60 km. The main reason for the rapidly decreasing speed at these altitudes is that the vehicle is exposed to higher drag forces. As altitude decreases, drag force goes up with increasing air density. In addition, the longer the vehicle flies at the lower altitudes, the faster the speed reduces.

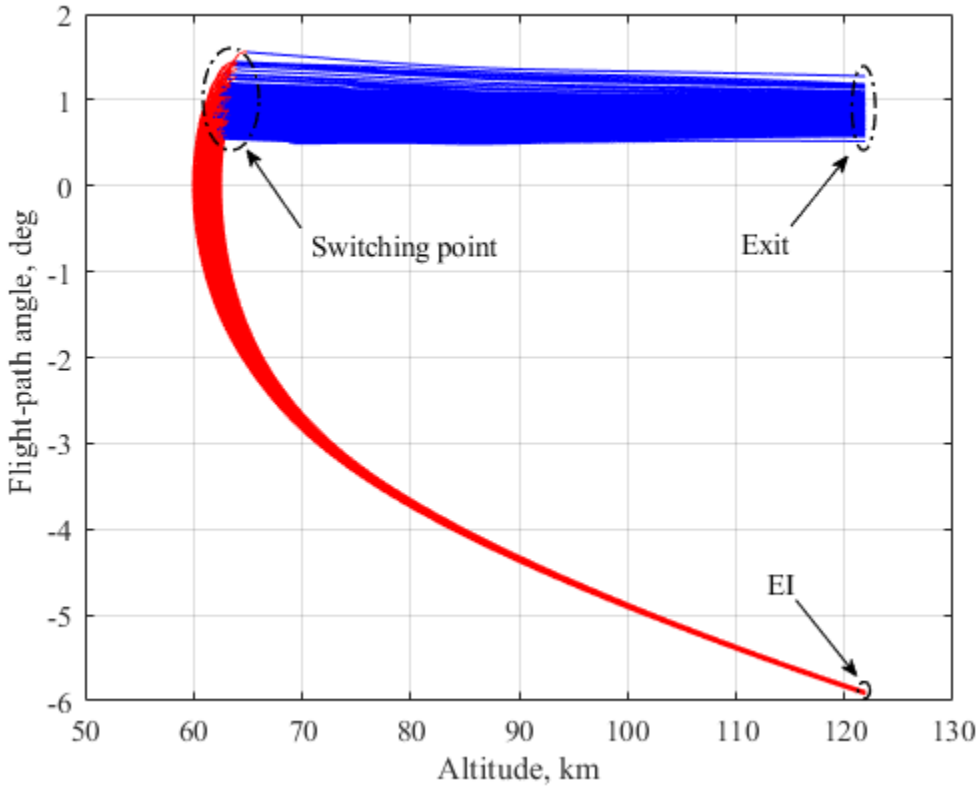

Fig. 5.8 Flight-Path Angle vs. Altitude for 1000 Monte-Carlo Simulations of Scenario 1

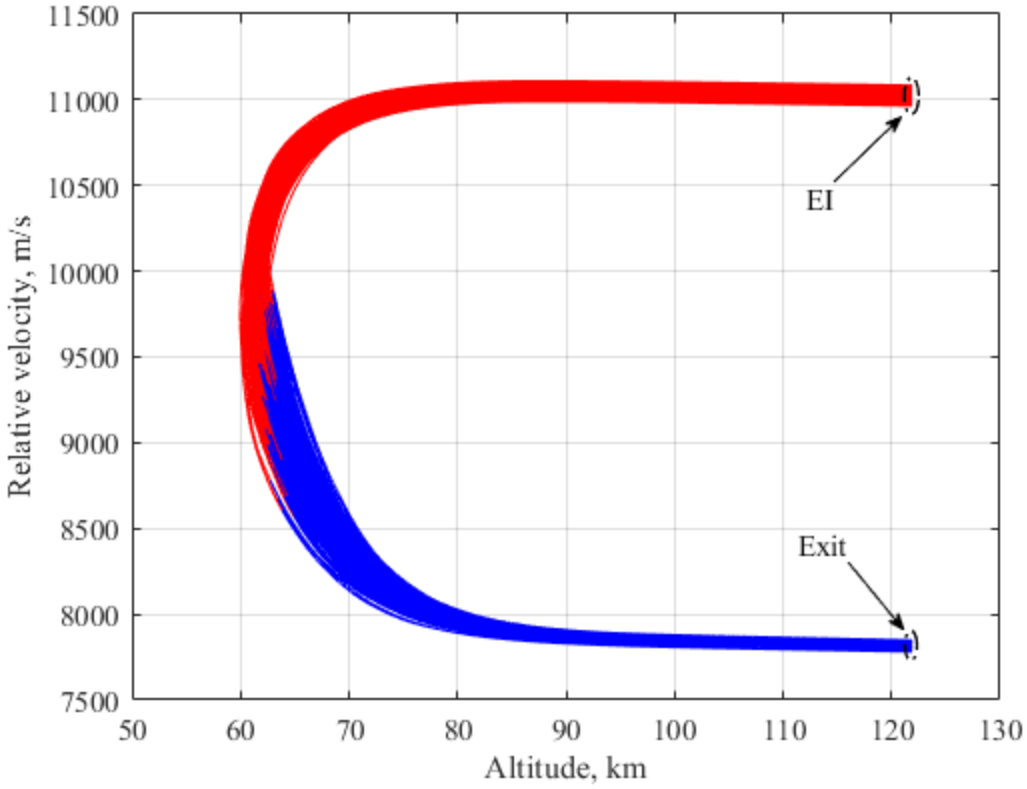

Fig. 5.9 Relative Velocity vs. Altitude for 1000 Monte-Carlo Simulations of Scenario 1

Figure 5.10 presents the 1000 bank angle profiles for scenario 1. Open-loop bank angle remains constant at 15 deg for the first 90-110 s after entry interface. Once the switching point is found, the vehicle performs bank angle transition from 15 deg (open loop) to ~120 deg (initial closed loop) in 8.5 s with maximum bank rate and acceleration limits. Closed-loop bank angle magnitudes range between 115 and 135 deg before starting bank reversal. The bank reversal takes about 9-10 s for near-nominal L/D with a shortest rotation direction (total bank angle change is about 120 deg) but is much shorter for vehicles with extremely low L/D. In such a case, the bank reversal starts at 162 deg and it takes 3.5 sec to go to -162 deg. The closed-loop bank is governed by equation (58) until saturation occurs at either full lift up or down. Even though the switching prediction is based on the bank

saturation at $\sigma = 180$ deg, the closed-loop bank occasionally saturates at $\sigma = 0$ deg due to inaccuracies in propagating the initial roll dynamics and because guidance has neglected the roll-reversal dynamics. Once the bank angle saturates, the bank angle stays constant at $\sigma = 0$ or $\sigma = 180$ deg until reaching exit.

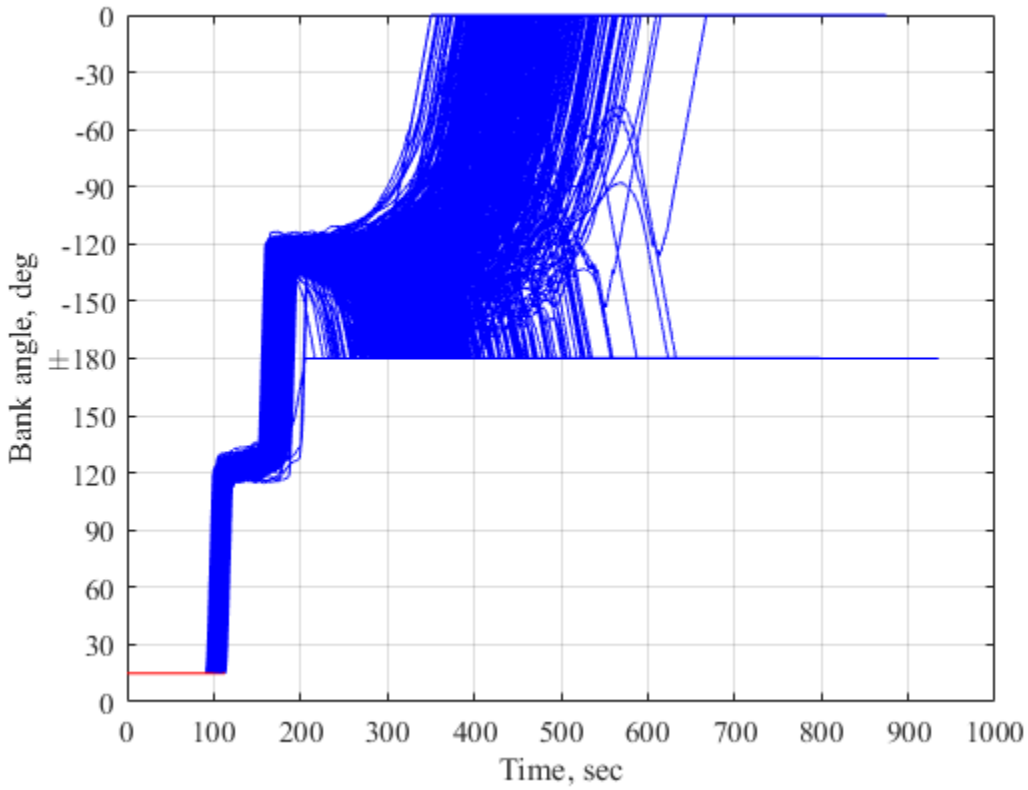

Fig. 5.10 Bank Angle vs. Time for 1000 Monte-Carlo Simulations of Scenario 1

Figure 5.11 illustrates inclination profiles from the simulation results. Since the initial heading angle is random, the initial inclination varies around 90 deg. Initially, flying right turn with a positive bank angle decreases inclination until the full lift down ($\sigma = 180$ deg) is reached. Then the left turn flight with a negative bank angle raises inclination. Recall that increasing *L*/*D* increases the bank-reversal inclination overshoot of the desired target

inclination and the flight time. All trajectories exit the atmosphere with inclinations within 0.25 deg from the target inclination of 88 deg.

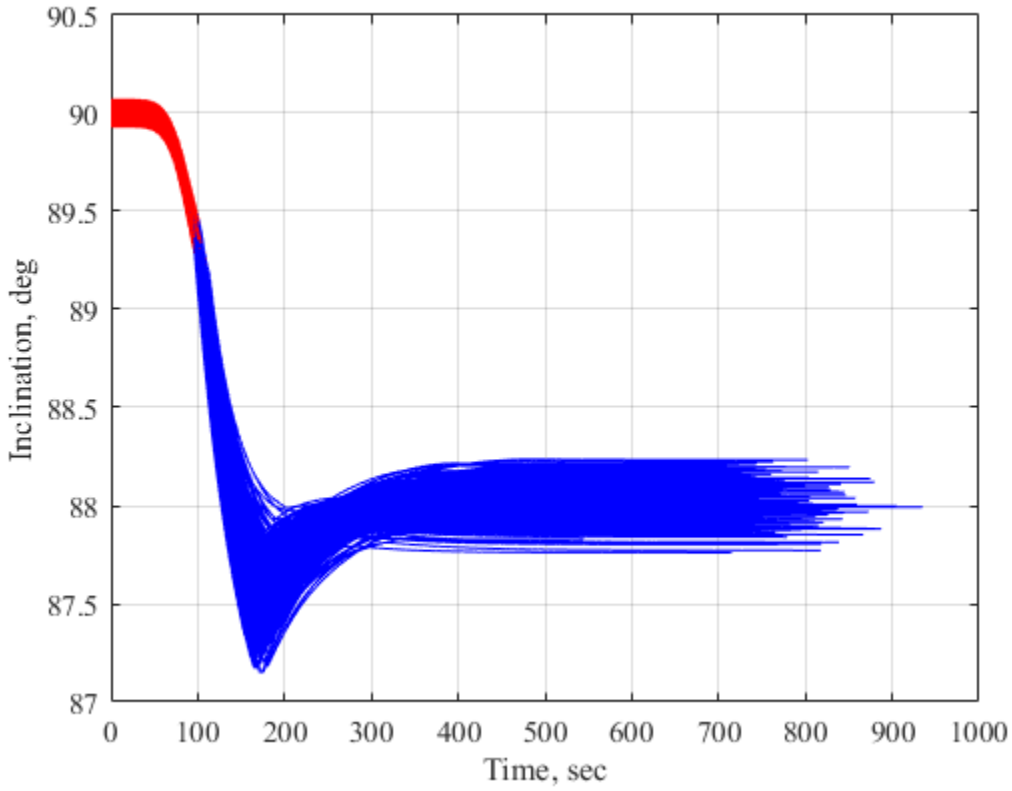

Fig. 5.11 Inclination vs. Time for 1000 Monte-Carlo Simulations of Scenario 1

Figure 5.12 presents the 1000 altitude time histories for scenario 1. The closed-loop guidance control (blue curves in Figure 5.12) always begins after the pull-up point. The Orion MPCV's the atmospheric flight time roughly between 400 and 900 s for a 1000-run Monte-Carlo simulation. The atmospheric flight time is directly proportional to the *L*/*D* ratio.

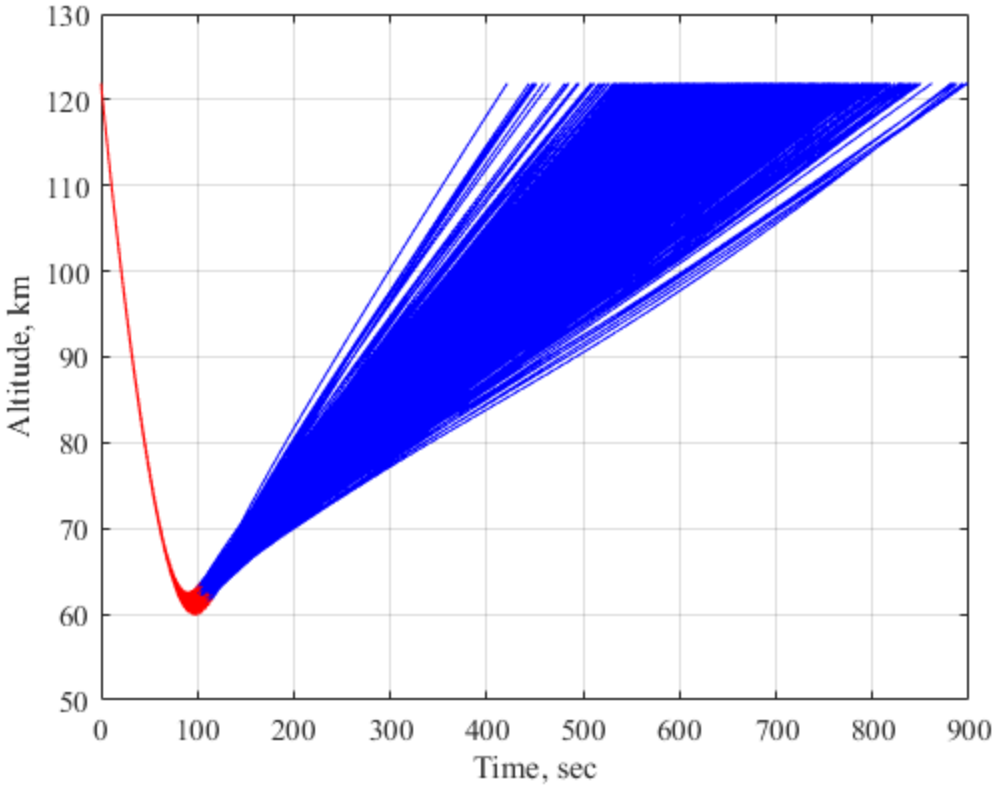

Fig. 5.12 Altitude vs. Time for 1000 Monte-Carlo Simulations of Scenario 1

Table 5.4 and Figures 5.13-5.15 present the statistics of the 1000 dispersed trajectories from the Monte-Carlo simulations for scenario 1. Apogee altitude of the post-aerocapture orbit is very accurate, with a mean value within 750 m of the target and a small standard deviation (< 10 km). Orbital inclination at exit conditions is also very close to inclination targeting value, and the standard deviation is less than 0.1 deg. The required impulsive orbital maneuvers to establish the target orbit are summarized in Table 5.4 into three categories, coplanar ΔV (single- or two-impulsive maneuver), plane-change ΔV_i, and total $\Delta V_T = \Delta V + \Delta V_i$. Mean coplanar ΔV is 54.64 m/s, which is only 15 m/s greater than the optimal single-impulse ($\Delta V = 39.6$ m/s) for the bang-bang aerocapture maneuver, while mean plane-change ΔV_i is 8.71 m/s. Although inclination errors are very small for all

trajectories, the inclination clean-up ΔV_i cost is high for a final orbit insertion maneuver. For example, the absolute maximum error for inclination is 0.23926 deg, which corresponds to an inclination-correction maneuver of 32.51 m/s. Despite the fact that mean total ΔV_T is equal to the sum of mean coplanar ΔV and mean plane-change ΔV_i, the minimum and maximum total ΔV_T values depend on in-plane maneuver and plane-change corrections for each trial case in Monte-Carlo simulations. Figures 5.13-5.14 show histograms of the apogee altitude of the exo-atmospheric trajectory, inclination at exit conditions, and the required total ΔV_T. In Figures 5.13-5.15, the fitted red curves for the normal distributions follow the heights of the histogram bars adequately. Figure 5.13 illustrates that there are some outliers around 240 km.

Table 5.4: Statistical Results from the Monte-Carlo Simulations for Scenario 1

Parameter	Mean	Standard deviation	Minimum	Maximum
Apogee altitude	200.710 km	9.852 km	171.247 km	243.676 km
Exit inclination	88.015^o	0.077^o	87.761^o	88.233^o
Coplanar ΔV	54.64 m/s	6.91 m/s	39.85 m/s	94.51 m/s
Plane-change ΔV_i	8.71 m/s	6.10 m/s	0 m/s	32.51 m/s
Total ΔV_T	63.35 m/s	9.76 m/s	40.31 m/s	99.85 m/s

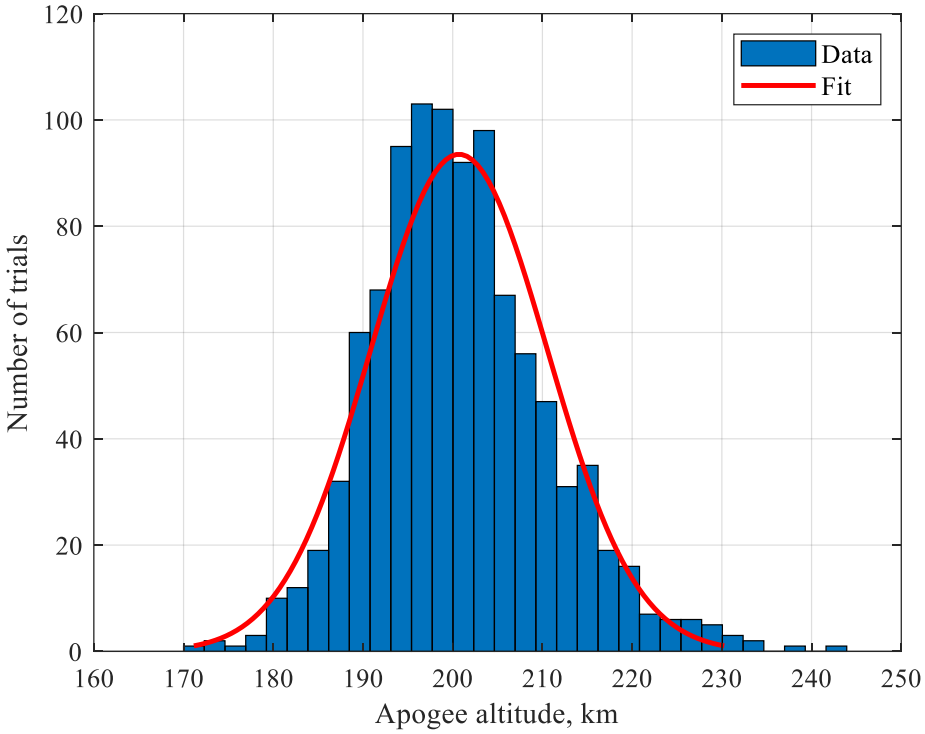

Fig. 5.13 Histogram of Apogee Altitude from 1000 Trails for Scenario 1

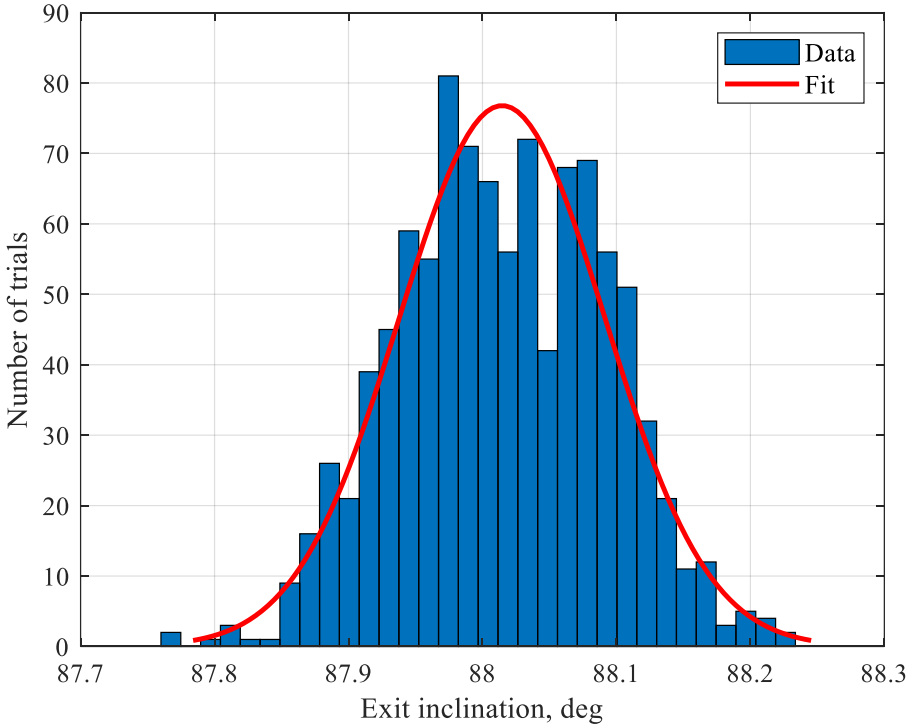

Fig. 5.14 Histogram of Exit Inclination from 1000 Trails for Scenario 1

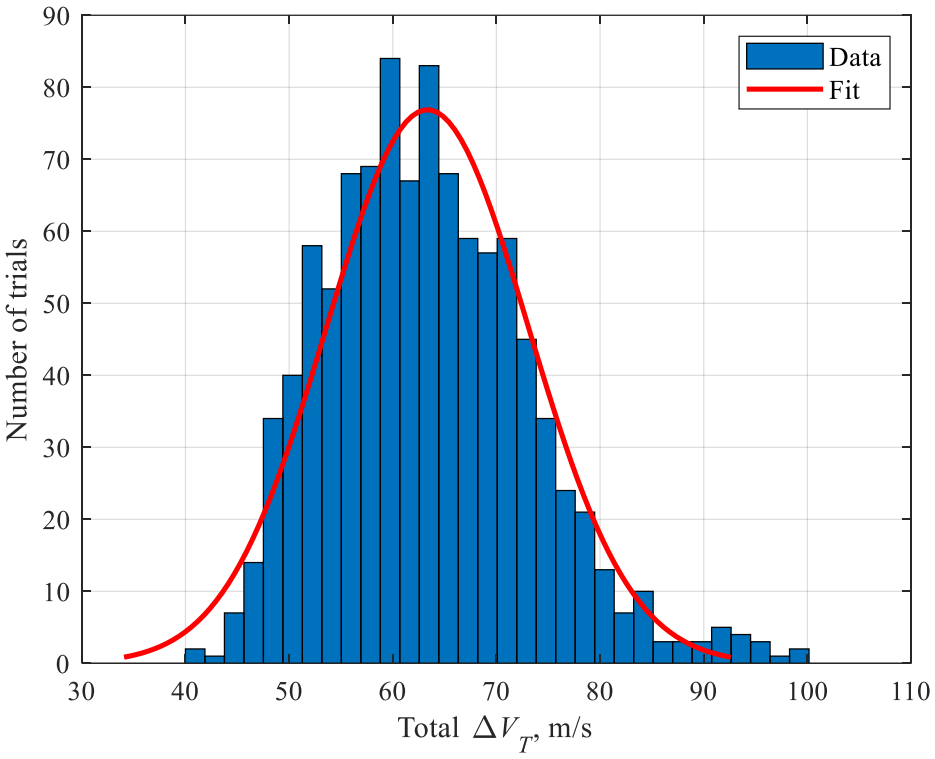

Fig. 5.15 Histogram of Total ΔV_T from 1000 Trails for Scenario 1

5.2.2.1 Comparison of Different-Term Fourier Curve Fitting Models

In this section, the performance and robustness of the analytical aerocapture guidance algorithm is compared among different-term Fourier curve fitting models. As has been presented in chapter 4, the products of density and lift (or drag) coefficient divided by mass, $\rho C_L/m$ and $\rho C_D/m$, are fitted by a three-term Fourier series in order to find an analytical solution for atmospheric exit velocity and closed-loop bank command. MATLAB's `cftool` can fit data with Fourier-series function up to 8th order. It should be pointed out that a one-term Fourier series cannot provide an adequate fit for $\rho C_L/m$ and $\rho C_D/m$ data. Also, a higher computational cost is required for seven- and eight-term Fourier series. Therefore, we only ran four additional 1000-dispersed Monte-Carlo simulation for Fourier-

series functions with two, four, five, and six terms. Tables 5.5-5.9 compare the statistical results from the 1000-dispersed Monte-Carlo simulation for the post-atmospheric apogee altitude, pre-burn orbital inclination, coplanar (or in-plane) ΔV, plane-change ΔV_i, and total ΔV_T (the statistical results from the baseline three-term Fourier series are also included). As can be seen in Tables 5.5, 5.7, and 5.9, the velocity increment and post-atmospheric apogee accuracy significantly degrade with the two-term Fourier series when compared to other higher-term Fourier series. Tables 5.5-5.9 demonstrate that for post-atmospheric apogee altitude, pre-burn orbital inclination, and velocity increment, the Fourier scenarios with three, four, five, and six terms have quite similar mean values. Table 5.9 shows that the mean total ΔV_T-minimization slightly goes down with the increasing the number of terms in Fourier series. On the other hand, as the number of terms in Fourier series increases, so does the computational complexity in the guidance algorithm. From these simulation results it is obvious that the three-term Fourier series offers very good performance at the lowest computational cost for the analytical aerocapture guidance scheme.

Table 5.5: Statistics for Apogee Altitude vs. Modeling Order for $\rho C_L/m$ and $\rho C_D/m$

Fourier series order	Mean value (km)	Standard deviation (km)	Minimum value (km)	Maximum value (km)
Two-term	170.7270	11.7138	136.1576	212.7329
Three-term	200.7099	9.8524	171.2472	243.6761
Four-term	199.1382	9.2179	167.4453	236.6728
Five-term	199.3314	8.7365	171.2249	240.9807
Six-term	200.3845	8.8472	173.7859	242.5521

Table 5.6: Statistics for Exit Inclination vs. Modeling Order for $\rho C_L/m$ and $\rho C_D/m$

Fourier series order	Mean value (deg)	Standard deviation (deg)	Minimum value (deg)	Maximum value (deg)
Two-term	88.0987	0.0621	87.8619	88.3171
Three-term	88.0147	0.0769	87.7607	88.2332
Four-term	88.0308	0.0696	87.7501	88.2408
Five-term	88.0152	0.0747	87.7670	88.2352
Six-term	88.0206	0.0704	87.7875	88.2424

Table 5.7: Statistics for Coplanar ΔV vs. Modeling Order for $\rho C_L/m$ and $\rho C_D/m$

Fourier series order	Mean value (m/s)	Standard deviation (m/s)	Minimum value (m/s)	Maximum value (m/s)
Two-term	71.4539	7.3068	49.2675	107.4301
Three-term	54.6368	6.9113	39.8462	94.5084
Four-term	54.7237	7.0588	39.7795	92.1993
Five-term	54.3128	6.7110	39.8742	91.0326
Six-term	53.9854	6.8387	39.6423	91.1412

Table 5.8: Statistics for Plane-Change ΔV_i vs. Modeling Order for $\rho C_L/m$ and $\rho C_D/m$

Fourier series order	Mean value (m/s)	Standard deviation (m/s)	Minimum value (m/s)	Maximum value (m/s)
Two-term	13.8441	7.6825	0.0019	43.0814
Three-term	8.7099	6.1985	0.0025	32.5115
Four-term	9.1001	6.4162	0.0051	33.9516
Five-term	8.6395	6.2061	0.0070	31.9545
Six-term	8.7231	6.2847	0.0032	32.9327

Table 5.9: Statistics for Total ΔV_T vs. Modeling Order for $\rho C_L/m$ and $\rho C_D/m$

Fourier series order	Mean value (m/s)	Standard deviation (m/s)	Minimum value (m/s)	Maximum value (m/s)
Two-term	85.2980	12.2607	53.7576	127.1587
Three-term	63.3467	9.7556	40.3124	99.8472
Four-term	63.8238	9.9162	41.8284	104.9169
Five-term	62.9523	9.3107	40.3919	101.8883
Six-term	62.7085	9.3325	41.0776	102.7299

5.3 Scenario 2 – Exponential Curve Fitting Simulation Results

In the second scenario, closed-form solutions for exit velocity are acquired by using exponential curve fitting method as described in section 4.2.1.2. A single-term exponential function parameterizes the lift and drag terms, $\rho C_L/m$ and $\rho C_D/m$, in equations (7) and (8). Nominal and off-nominal (Monte-Carlo) simulation results for scenario 2 will be provided in the following subsections.

5.3.1 Nominal Results for Scenario 2

A nominal aerocapture trajectory is developed for the second scenario by using the same nominal models as in the first scenario. Four exponential coefficients (k_0, k_1, x_0, and x_1) for both dimensionless nominal lift- and drag-acceleration vs. altitude data are found from the least-square fitting technique as summarized in Table 5.10. Because the ratio of $\rho C_L/m$ to $\rho C_D/m$ is equal to *L/D,* the coefficients k_1 and x_1 has the same value, and the ratio of k_0 to x_0 must be equal to 0.27.

Table 5.10: Nominal Exponential-Functions Coefficients for Scenario 2

Data	Coefficients	Value
$\rho C_L/m$ vs. altitude	k_0	3.78491×10^4
	k_1	-8.00316
$\rho C_D/m$ vs. altitude	x_0	1.40189×10^4
	x_1	-8.00316

Figures 5.16 and 5.17 show the dimensionless nominal data (note that these data are the same as in Figures 5.3 and 5.4) and exponential-fit curves. For both fitted curves in this scenario, R-squared values are found as 0.997 from the goodness-of-fit statistics. As seen in Figures 5.16 and 5.17, a single-term exponential fitting curve does not follow closely the dimensionless nominal lift and drag data at the dimensionless altitude of between 1.25 (≡75 km) and 2.032 (≡121.92 km). This curve fitting method will result in relatively poor apoapsis accuracy when compared to the baseline three-term Fourier series.

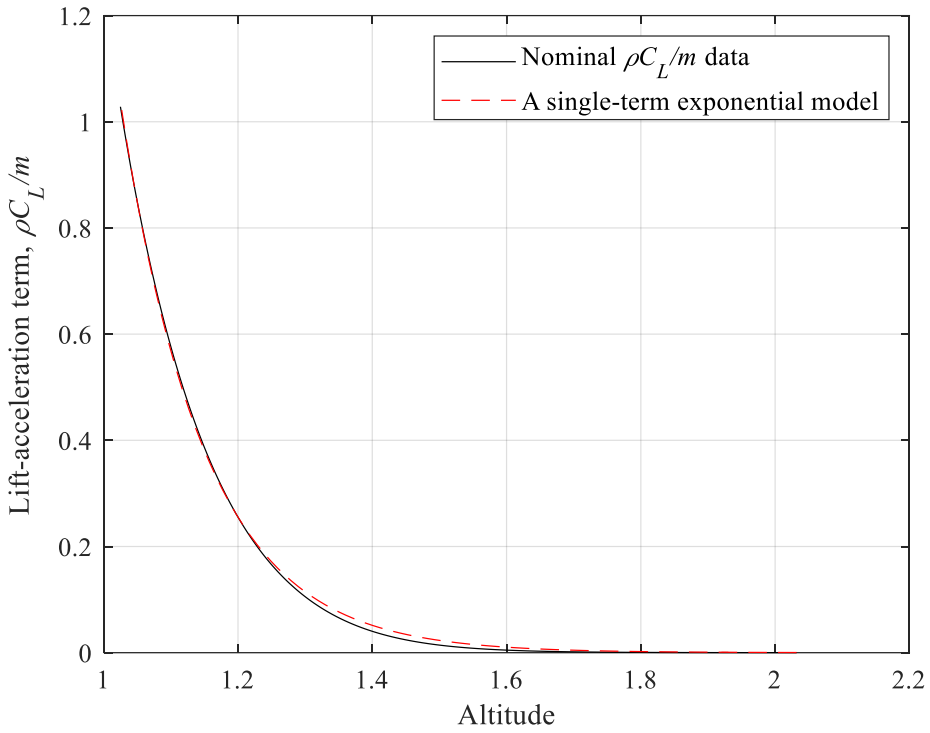

Fig. 5.16 Curve Fit on Dimensionless $\rho C_L/m$ vs Altitude for Scenario 2

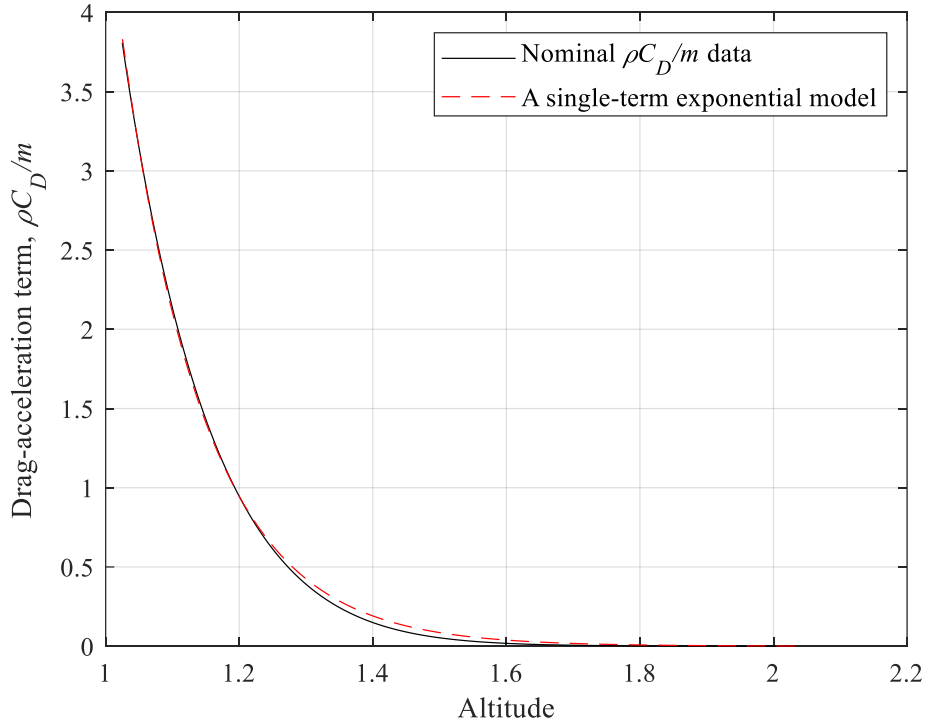

Fig. 5.17 Curve Fit on Dimensionless $\rho C_D/m$ vs Altitude for Scenario 2

For the second scenario, Figures 5.18 and 5.19 present the nominal trajectory simulation results for inclination and bank angle profiles, respectively. The nominal bank-switching begins at t = 96.7 s (recall that the nominal bank-switching time is 97.7 s for the first scenario). The nominal apogee altitude of the post-aerocapture orbit is 241.24 km with an orbital inclination of 88 deg., the vehicle needs a periapsis raise burn ($\Delta V_1 = 44.63$ m/s) and then a apogee clean-up burn ($\Delta V_2 = 12.15$ m/s). The sum of the two coplanar velocity increments is 56.78 m/s for the nominal second scenario (recall that the total $\Delta V = 49.04$ m/s for the nominal first scenario). Although both scenarios have similar nominal inclination and bank angle profiles, the apoapsis targeting accuracy for scenario 2 is much worse than scenario 1 due to inaccuracies in the exponential curve fitting model.

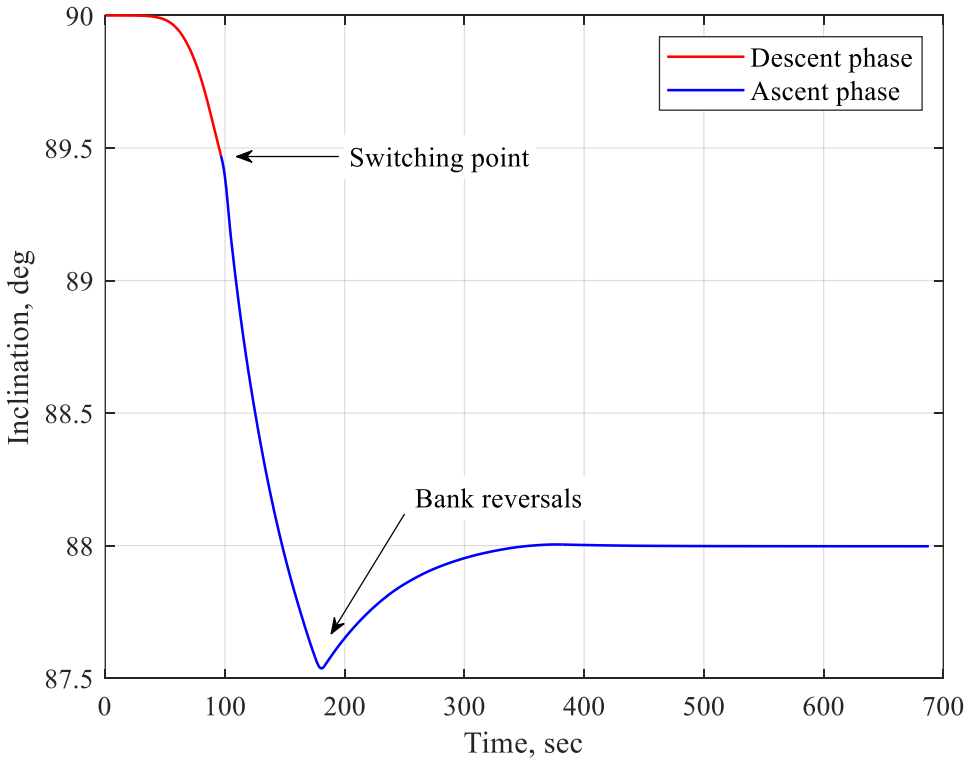

Fig. 5.18 Nominal Inclination Time History for Scenario 2

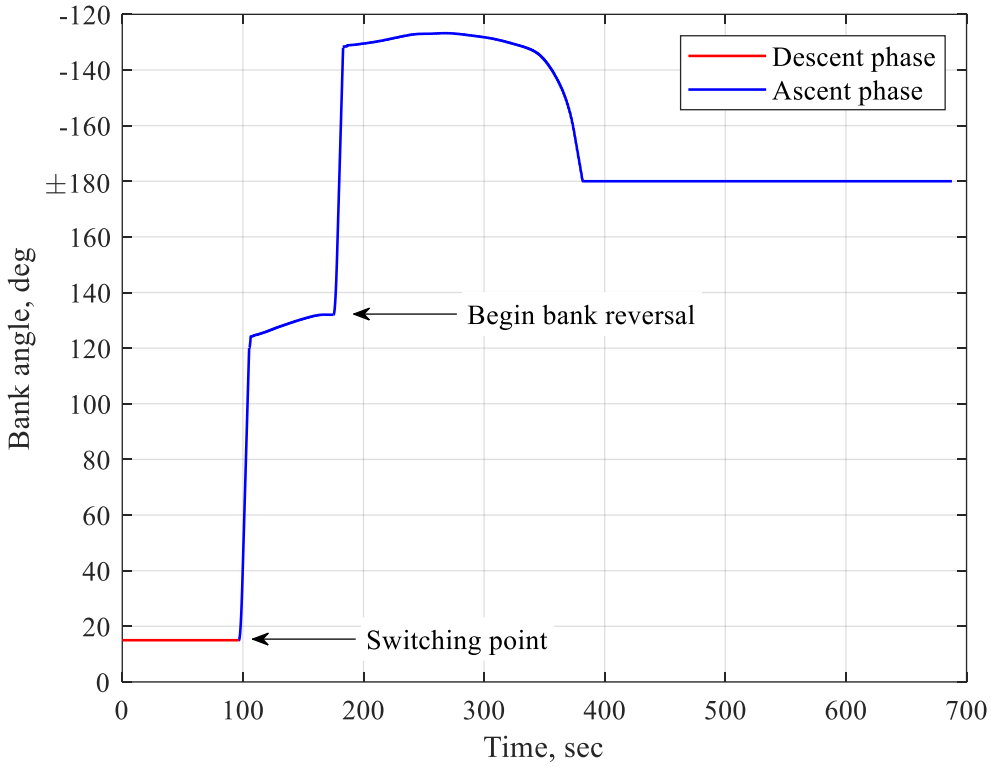

Fig. 5.19 Nominal Bank Angle Time History for Scenario 2

5.3.2 Monte-Carlo Simulation Results for Scenario 2

For the second scenario, we use the same 1000 dispersed cases investigated in the first scenario. A similar set of figures will be given to compare the results between two scenarios. Figures 5.20 and 5.21 present flight-path angle and relative velocity vs. altitude profiles from the Monte-Carlo simulations for scenario 2 (again, red and blue curves indicate open- and closed-loop aerocapture phase). The exit FPAs of the 1000 dispersed trajectories are between 0.5 and 1.4 deg, and the exit velocity band is between 7795 and 7883 m/s. Figures 5.22-5.24 show the bank angle, inclination, and altitude histories of 1000 aerocapture trajectories for scenario 2. The closed-loop bank usually saturates at $\sigma = 180$ deg as seen in Figure 5.22.

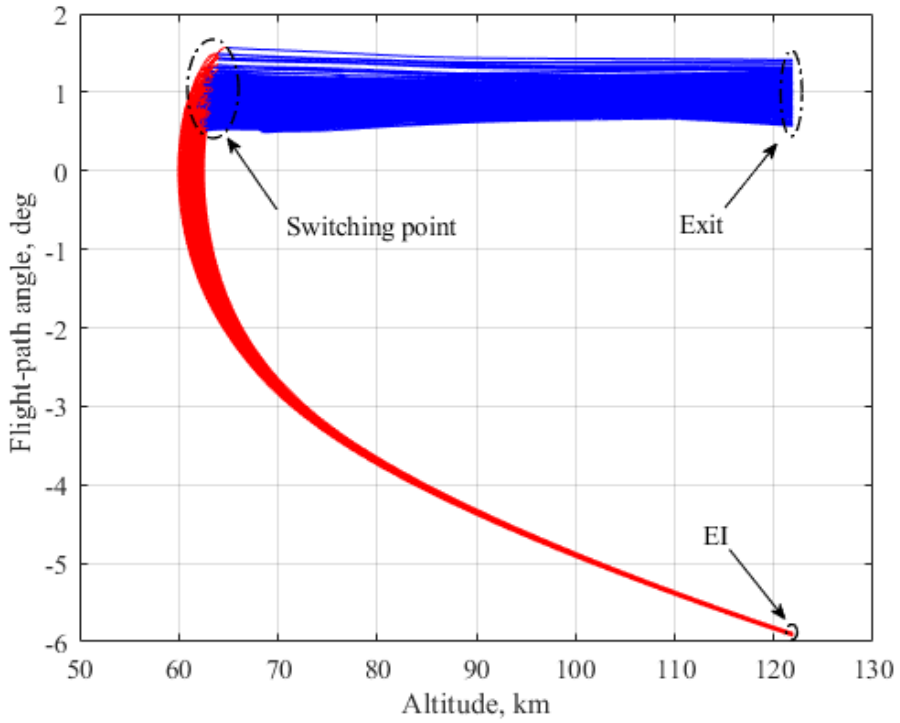

Fig. 5.20 Flight-Path Angle vs. Altitude for 1000 Monte-Carlo Simulations of Scenario 2

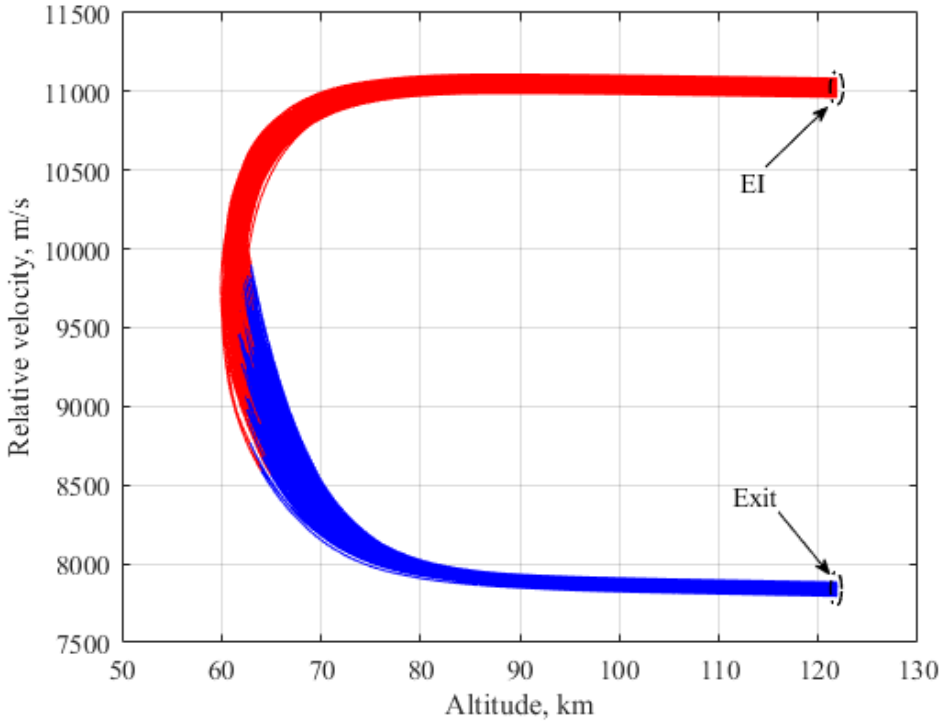

Fig. 5.21 Relative Velocity vs. Altitude for 1000 Monte-Carlo Simulations of Scenario 2

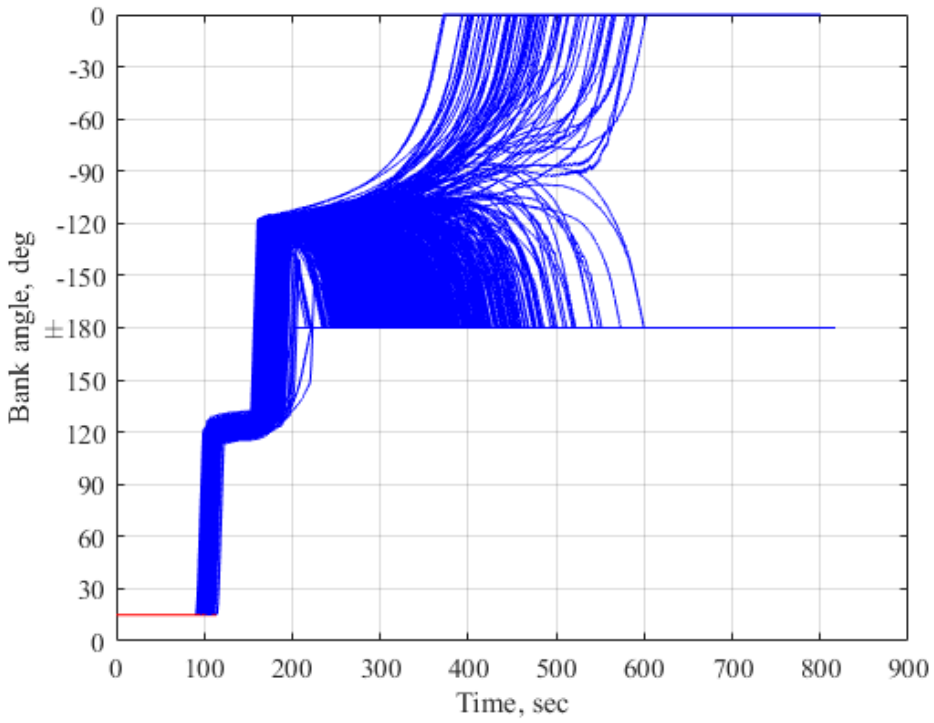

Fig. 5.22 Bank Angle vs. Time for 1000 Monte-Carlo Simulations of Scenario 2

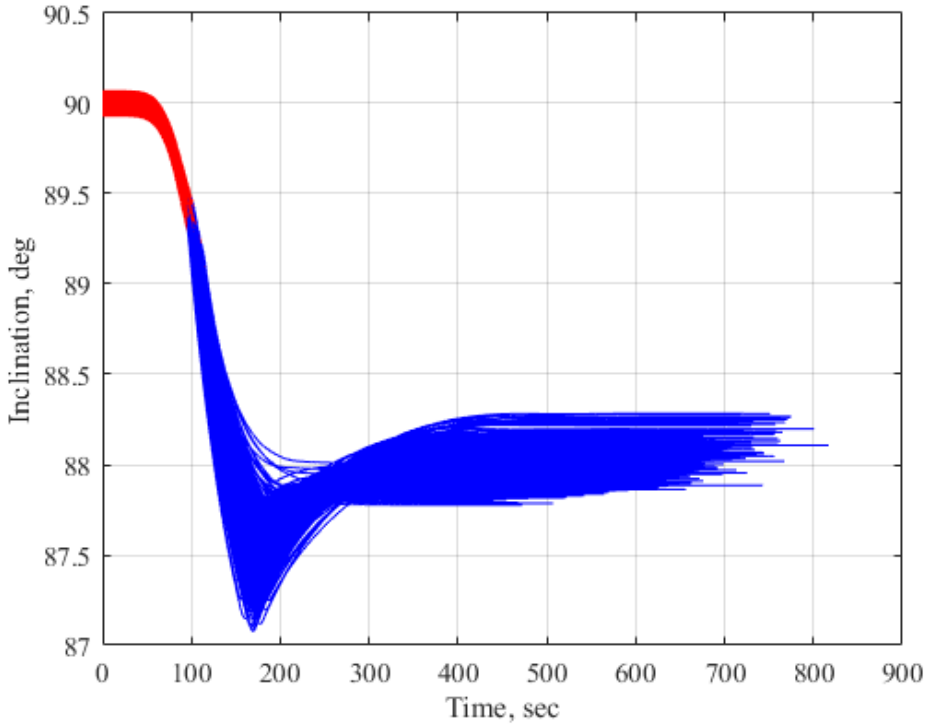

Fig. 5.23 Inclination vs. Time for 1000 Monte-Carlo Simulations of Scenario 2

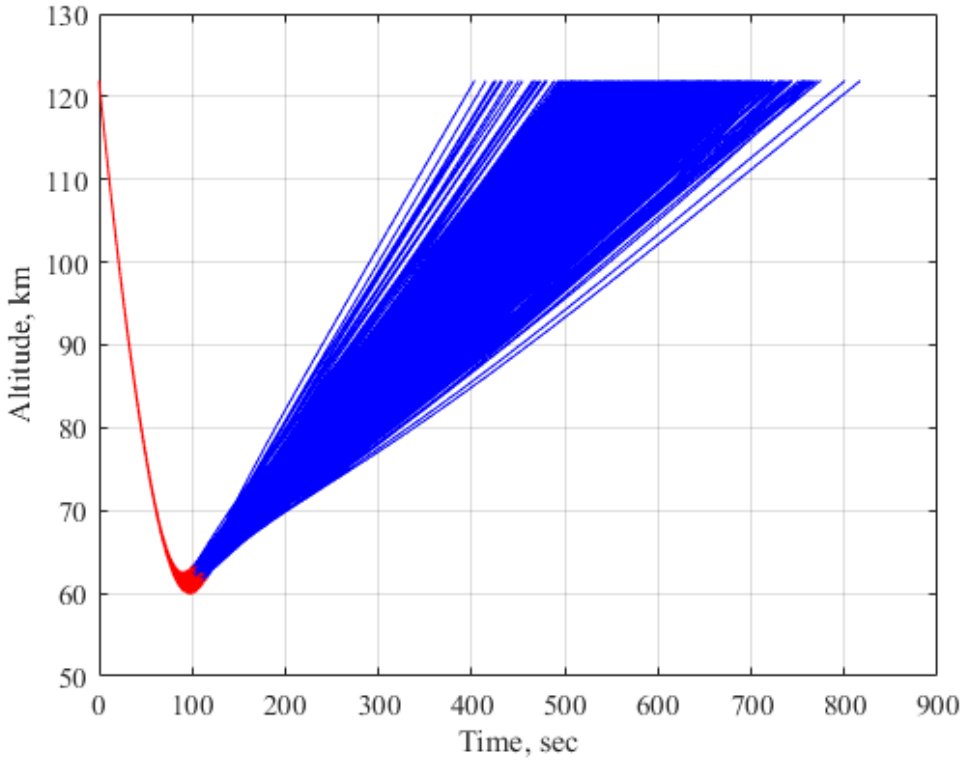

Fig. 5.24 Altitude vs. Time for 1000 Monte-Carlo Simulations of Scenario 2

Table 5.11 and Figures 5.25-5.27 present the statistical results from the 1000 Monte-Carlo simulations in the second scenario. The mean apogee altitude of the exo-atmospheric orbit is 56.5 km higher than the target altitude. The large spread in the apogee altitude causes a high standard deviation of 38.86 km. Pre-burn orbital inclination is still very close to inclination targeting value of 88 deg, and all exit inclinations are within 0.29 deg from the target inclination. Mean in-plane ΔV and plane-change ΔV_i values for the second scenario is approximately 20% greater than ones for the first scenario. Figures 5.25-5.27 show histograms of the apogee altitude of the post-aerocapture orbit, pre-burn orbital inclination, and the total post-exit ΔV_T. Figure 5.25 gives an impression of a normal distribution, but more than 92% apogees overshoot the target circle. In Figures 5.26 and 5.27, the data appear as a right skewed distribution. The medians are less than the mean in there. These

demonstrate that more than 50% of the pre-burn inclination and total ΔV_T data are located less than their mean values of 87.971 deg and 76.51 m/s, respectively.

Table 5.11: Statistical Results from the Monte-Carlo Simulations for Scenario 2

Parameter	Mean	Standard deviation	Minimum	Maximum
Apogee altitude	256.462 km	38.860 km	150.867 km	377.711 km
Exit inclination	87.971º	0.086º	87.777º	88.282º
Coplanar ΔV	66.24 m/s	9.31 m/s	45.79 m/s	96.47 m/s
Plane-change ΔV_i	10.27 m/s	6.84 m/s	0 m/s	38.37 m/s
Total ΔV_T	76.51 m/s	13.44 m/s	53.98 m/s	119.37 m/s

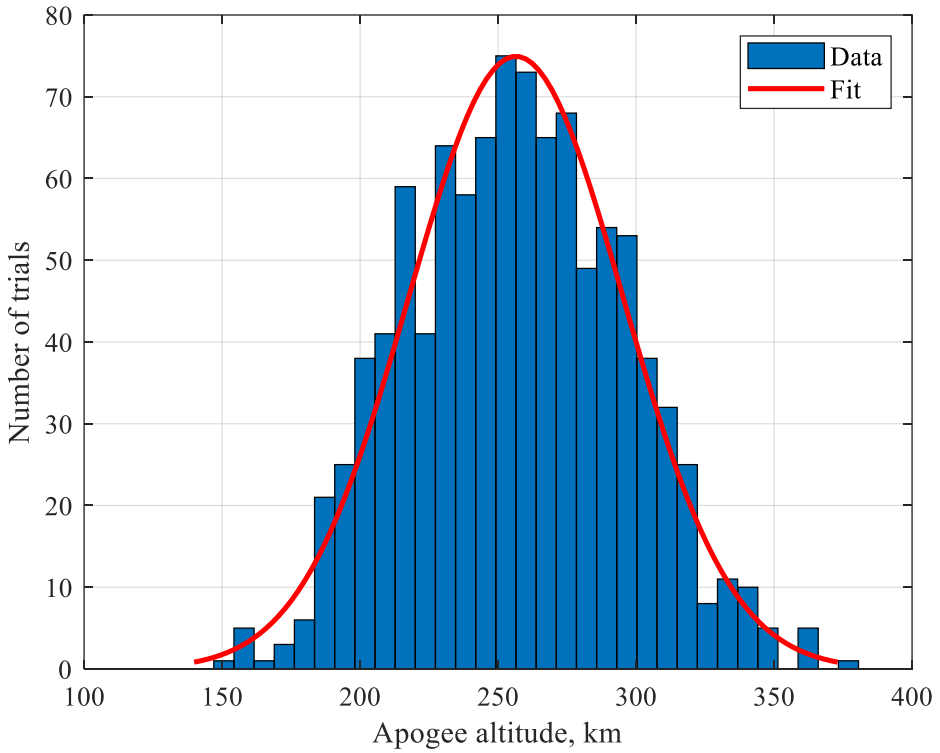

Fig. 5.25 Histogram of Apogee Altitude from 1000 Trails for Scenario 2

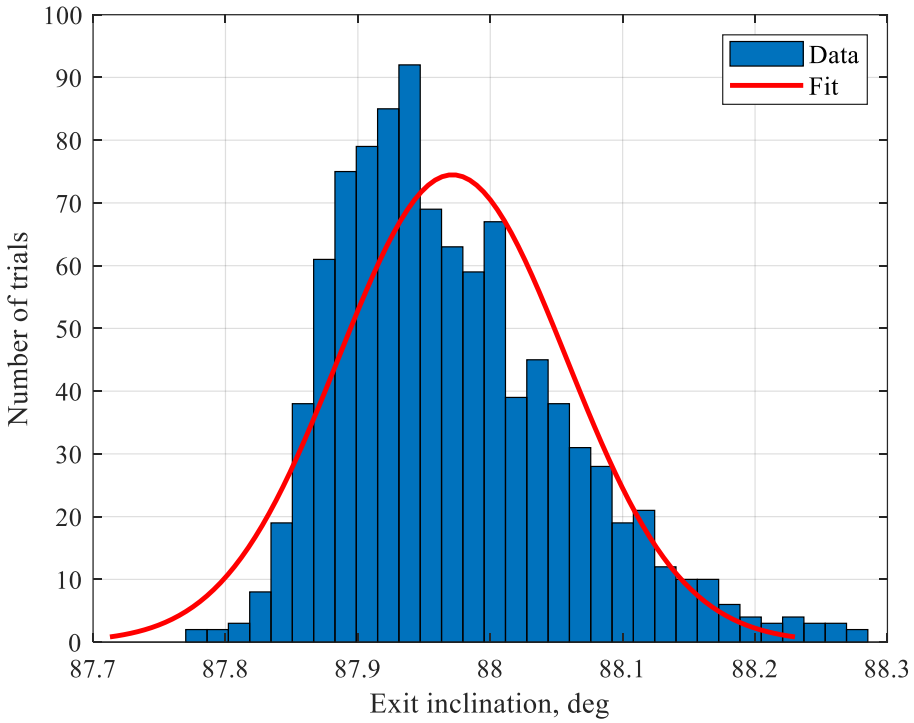

Fig. 5.26 Histogram of Exit Inclination from 1000 Trails for Scenario 2

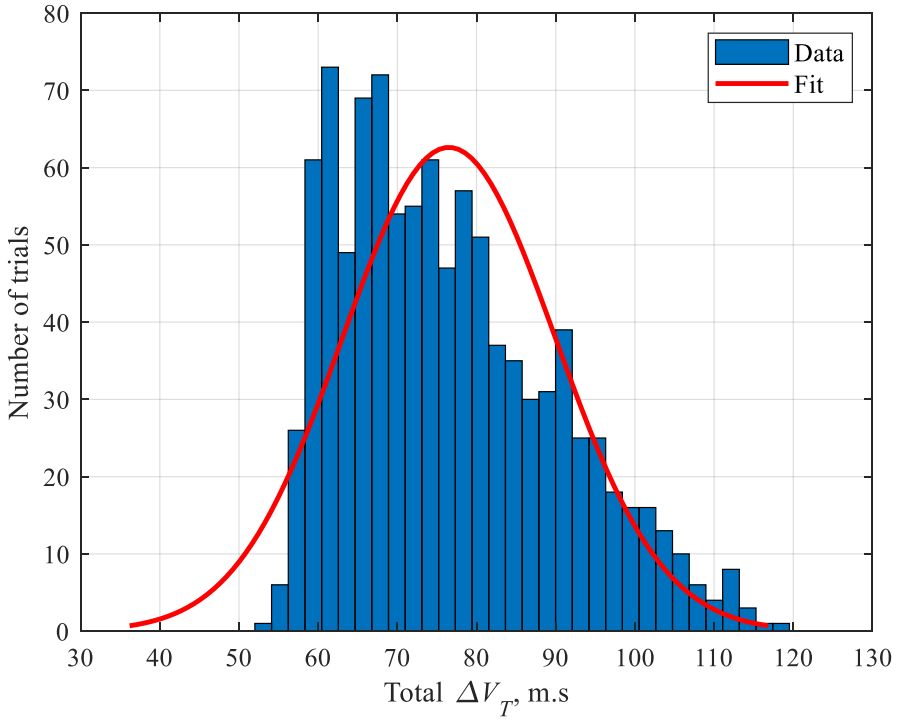

Fig. 5.27 Histogram of Total ΔV_T from 1000 Trails for Scenario 2

5.4 Comparison with NPC

For the Earth aerocapture problem, a comparison is made between the APC guidance algorithm proposed in this thesis and the NPC guidance algorithm investigated by Lu et al. [30]. These two studies share the same aerocapture mission, including the use of the same vehicle models, entry states, operational limits, and distributions for dispersions (a few dispersions are larger in this work, such as aerodynamic coefficients and entry state uncertainties). As we mentioned earlier, Lu et al. developed a closed-loop NPC guidance scheme that utilized the bang-bang control structure to steer the vehicle to a target state. Because the out-of-plane maneuvers are not reported in Ref. [30], we can only make a direct comparison for the in-plane maneuvers ΔV between the proposed APC method in this work and NPC method reported in Ref. [30]. Figure 5.28 shows the nominal in-plane ΔV values for the analytical guidance of this work with scenario 1 and 2, and the NPC from Ref. [30]. To establish the circular target orbit using nominal models, the APC guidance in-plane ΔV is 49.04 m/s with scenario 1 and 56.78 m/s with scenario 2, while the nominal value is reported in Ref. [30] as $\Delta V = 75.05$ m/s. By using the APC aerocapture guidance scheme with scenario 1 instead of the NPC guidance the minimized in-plane ΔV could be reduced by 35%. For a given ΔV, the propellant mass required for a propulsive burn can be calculated from the ideal rocket equation (15). When we consider that the Orion MPCV has initial vehicle mass of 8983.4 kg, and that the vehicle's onboard propellant has a specific impulse of 300 s [30], for the $\Delta V = 49.04$ m/s, $\Delta V = 56.78$ m/s, and $\Delta V = 75.05$ m/s, the propellant mass required for a propulsive burn is 148.50 kg, 171.72 kg, and 226.27 kg, respectively. Although both APC and NPC methods share a same constant bank angle ($\sigma = 15$ deg) in descent phase, the closed-loop bank command in the APC method is closer

to full lift down ($\sigma = 180$ deg) during the ascent phase than in the NPC method (recall that a lower constant bank angle ($\sigma_d = 95$ deg) is chosen for the ascent phase of the NPC method because of their tradeoff between ΔV performance and robustness). Hence, the nominal ΔV performance of the APC method is much closer to the optimal bang-bang solution.

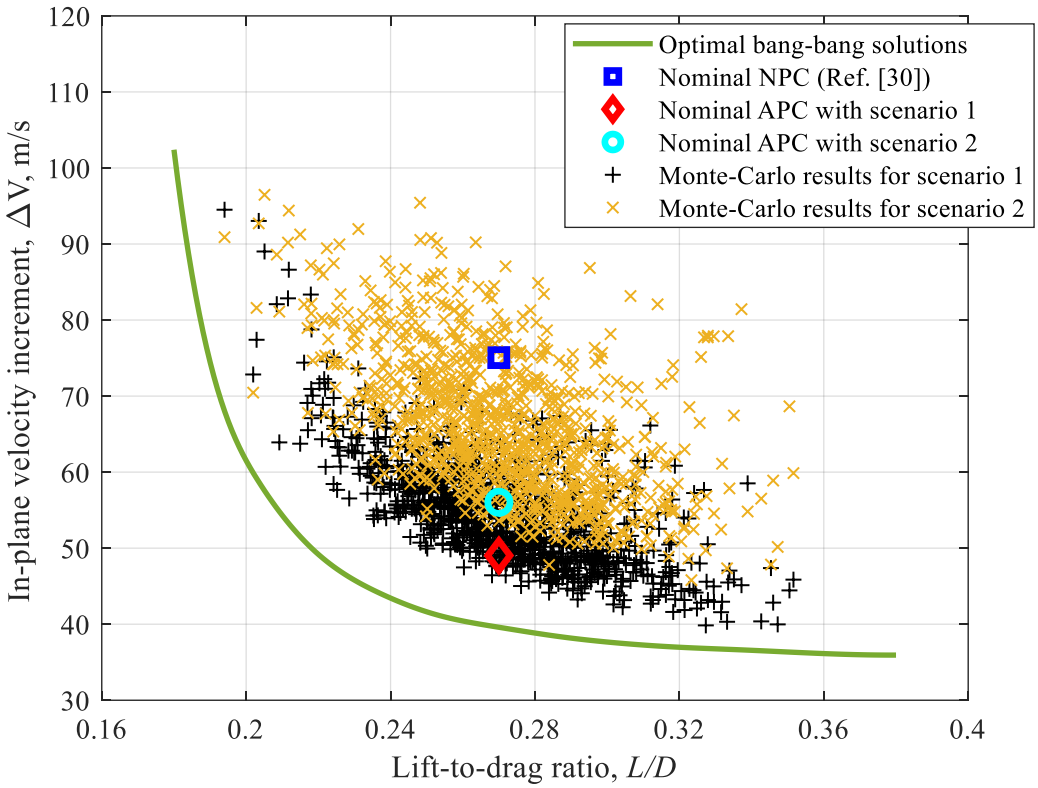

Fig. 5.28 Aerocapture In-plane Maneuver ΔV vs. Lift-to-Drag Ratio

Figure 5.28 also presents the total in-plane ΔVs from the 1000-dispersed Monte-Carlo simulation for scenarios 1 and 2 plotted against the randomized *L*/*D* ratio. Note that the statistics in Tables 5.4 and 5.11 respectively represent the 1000 black "+" and orange "x" symbols plotted in Figure 5.28, and that scenarios 1 and 2 are run under exactly the same Monte-Carlo dispersions. The green solid curve in Figure 5.28 presents, for a range of *L*/*D*

ratio, the minimum-ΔV solutions (single impulse) for the optimal bang-bang aerocapture problem with nominal entry states, nominal atmosphere, and no roll dynamics or plane-change maneuvers. Note that this curve is an extension of a vertical slice of Figure 3.5 at the nominal entry FPA, $\gamma_{\mathrm{EI}} = -5.91$ deg, and that the curve is a lower ΔV boundary for a range of *L*/*D* ratio, but in practice the optimal bang-bang bank control experiment is an unachievable goal due to the trajectory dispersions and limits on the attitude dynamics. The scatter plots for scenarios 1 and 2 have an inverse correlation with *L*/*D* ratio as the optimal bang-bang solutions. Since a three-term Fourier series model provides the better-fit curves for the $\rho C_L/m$ and $\rho C_D/m$ vs. altitude data than the exponential model, the majority of the 1000 data points for scenario 1 are much closer to the optimal bang-bang solutions than for scenario 2.

5.5 Variation in Entry Flight-Path Angle

In this section, a simulation scenario for a wide range of entry flight-path angle is created to test the proposed APC guidance method using scenario 1. Firstly, an entry FPA corridor width is determined. When the initial nominal velocity is fixed, *L/D* ratio and vehicle mass are the primary variables in the determination of the entry FPA corridor width to reach the target apoapsis. For a given initial velocity of 6.5 m/s and *L/D* (0.22 to 0.32), the entry FPA corridor width is set between –6.2 and –5.7 deg. The switching-point criteria (Figure 4.4) and the bank-reversal criteria (Figure 4.7) must be expanded to include large variations in the initial FPA. Figure 5.29 shows the bank-saturation altitude (h_{sat}) for six values of entry FPA (–6.2 to –5.7 deg) and six values of *L*/*D* ratio (0.22 to 0.32). In a similar way to the section 4.2.3, the bank-saturation altitude is determined from minimum-ΔV aerocapture trajectories for these 36 trials of entry FPA and *L*/*D*. Therefore, the bank-

saturation altitude is computed by a two-dimensional table look-up of the 36 combinations presented in Figure 5.3 with entry FPA and *L*/*D* as the independent variables.

Figure 5.30 presents the 36 bank-reversal inclinations (i_{rev}) for the combinations of six values of entry FPA and *L*/*D*. The bank-reversal inclination for any couple of entry FPA (between –6.2 and –5.7) and *L*/*D* (between 0.22 and 0.32) is determined in the same manner as the bank-saturation altitude. It should be noted that Figures 4.4 and 4.7 are essentially vertical slices of the three-dimensional surfaces, respectively, in Figures 5.29 and 5.30 at the nominal entry FPA, $\gamma_{\mathrm{EI}} = -5.91$ deg.

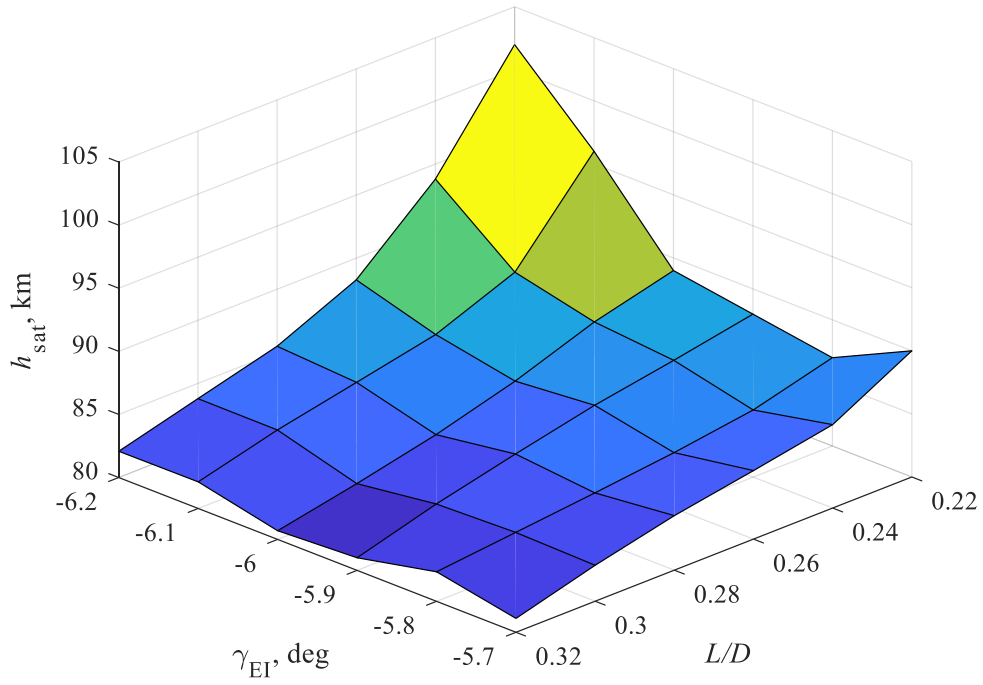

Fig. 5.29 Bank-Saturation Altitude (h_{sat}) vs. Entry FPA (γ_{EI}) and *L/D* Ratio

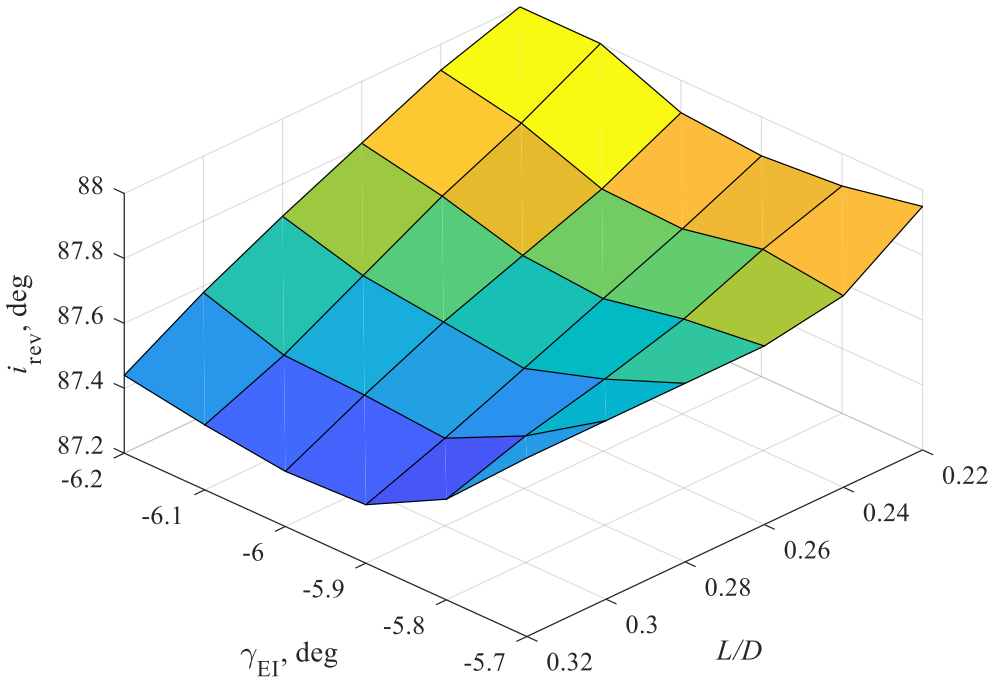

Fig. 5.30 Bank-Reversal Inclination (i_{rev}) vs. Entry FPA (γ_{EI}) and *L/D* Ratio

Lastly, a total of 1000 Monte-Carlo runs are made to analyze for a wide range of entry flight-path angle by using the APC guidance with scenario 1. For this 1000-run Monte-Carlo simulation, the entry FPA is uniformly dispersed between –6.2 and –5.7 deg; the other entry states (longitude, latitude, velocity, and heading angle) have Gaussian distributions (3σ values can be seen in Table 5.2); the lift and drag coefficients are distributed normally with 10% 3σ dispersions; vehicle mass has a uniform distribution with ±5% error; and the atmospheric density dispersions are modeled by Earth GRAM 2010 and equation (74). Figure 5.31 shows the in-plane maneuver ΔV from the 1000 Monte-Carlo trajectories using the APC guidance with scenario 1, as well as the minimum post-exit ΔV for the bang-bang aerocapture optimization problem with *L*/*D* = 0.22, 0.27 (nominal), and 0.32. The optimal bang-bang solutions (red, blue, green lines in Figure 5.31) have constant

values of *L/D* for between –6.2 and –5.7 deg. The lower the *L/D* ratio, the less control authority the vehicle will have. This causes guidance performance degradation in terms of post-exit ΔV. Figure 5.31 also shows that the APC guidance using scenario 1 provides near-optimal performance for an entry FPA shallower than the nominal case (–5.91 deg) and good aerocapture performance for the more difficult cases with steeper entry FPA. Because *L/D* is dispersed about the nominal value of 0.27, the majority of the 1000 in-plane post-exit ΔVs follows the trend of the optimal bang-bang solutions with *L/D* = 0.27. On the other hand, a few scenarios of the 1000 off-nominal guided trajectories have a high post-exit ΔV (> 120 m/s) due to combinations of low *L/D* and steep entry FPA.

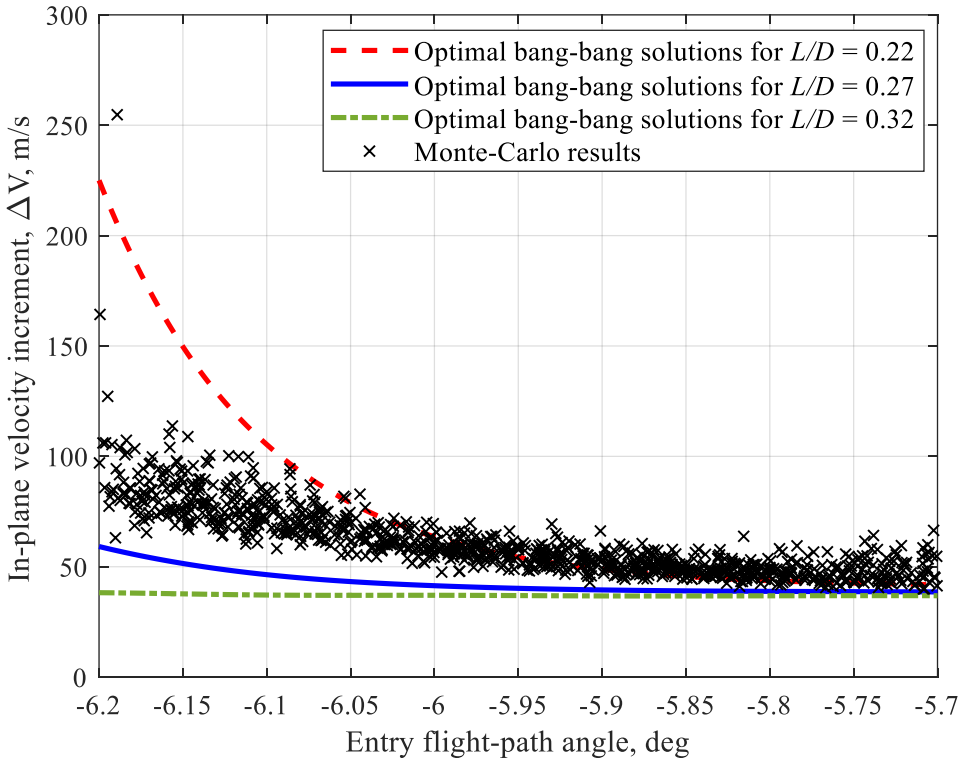

Fig. 5.31 Aerocapture In-plane Maneuver ΔV vs. Entry FPA

Figures 5.32-5.34 present the statistical results from the 1000 Monte-Carlo simulations under large variations in the entry flight-path angle. Mean apogee altitude and in-plane ΔV are still very close to target values. Figures 5.32 and 5.33 also show that the normal distribution curves for apogee altitude and pre-burn orbital inclination follow the heights of the bars, while there are a small number of outliers. Figure 5.34 shows that this is a right-skewed graph with a few data on the far right. This trend means that the more than 50% of the post-exit in-plane ΔVs are less than 61.12 m/s for this 1000-run Monte-Carlo simulation.

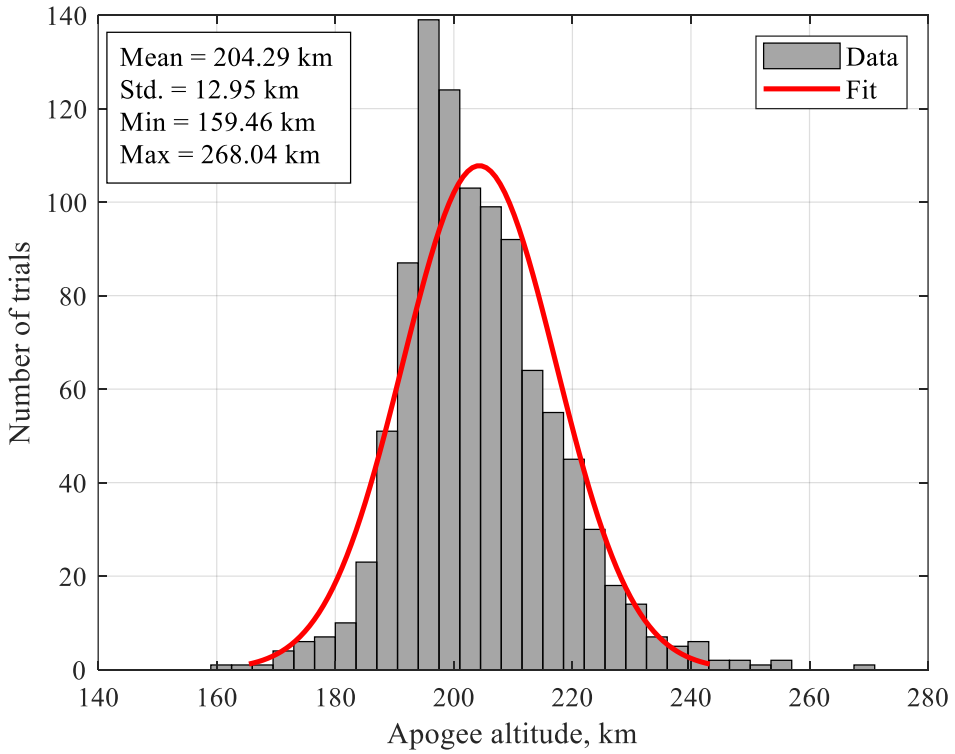

Fig. 5.32 Histogram of Apogee Altitude from 1000 Trails under Large Variations in Entry FPA

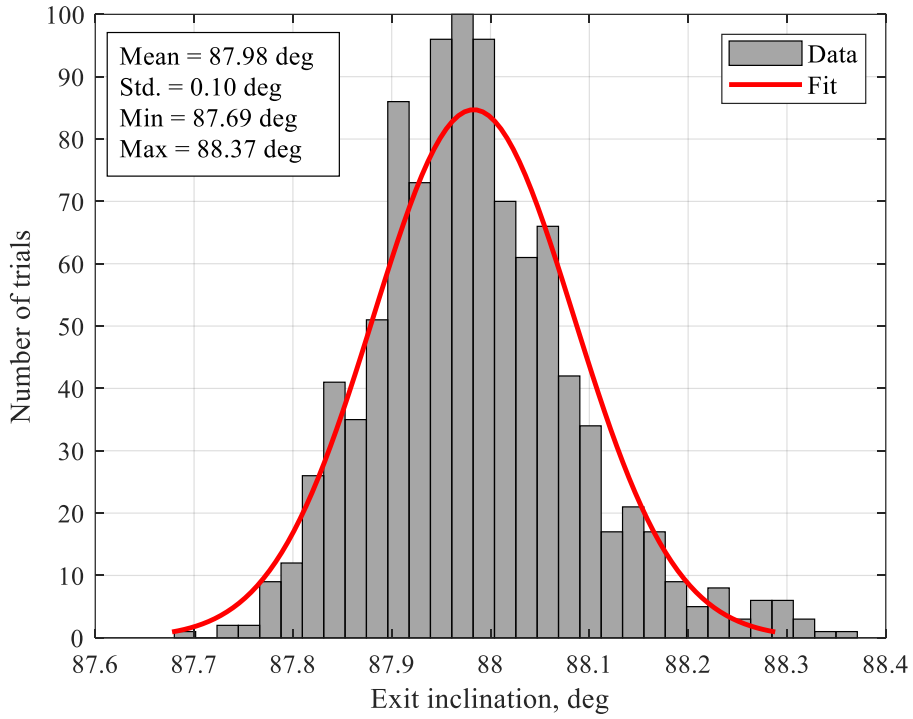

Fig. 5.33 Histogram of Exit Inclination from 1000 Trails under Large Variations in Entry FPA

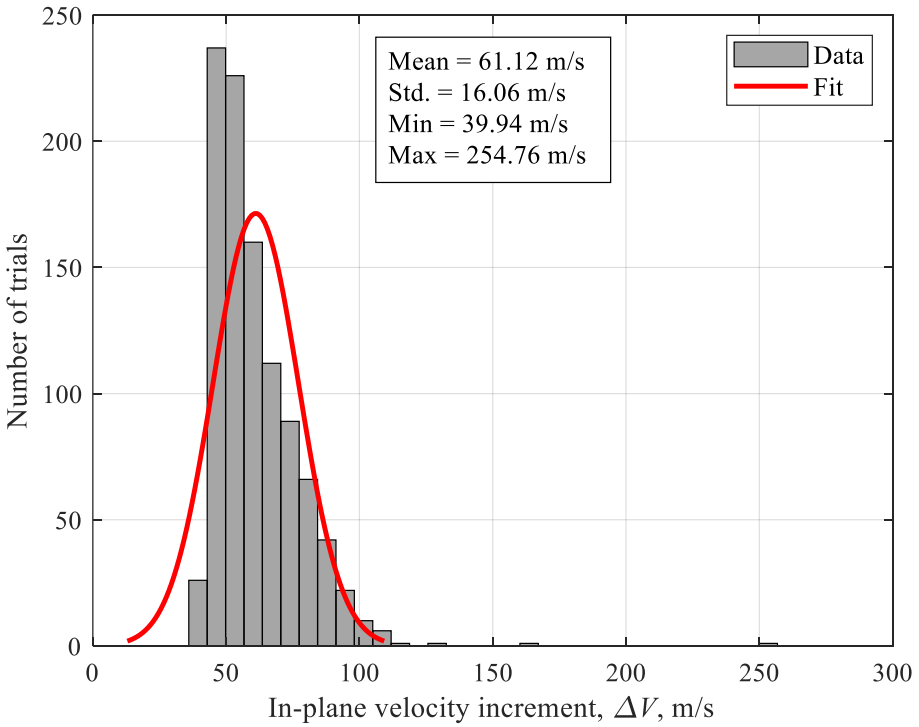

Fig. 5.34 Histogram of In-plane ΔV from 1000 Trails under Large Variations in Entry FPA

CHAPTER 6 – SUMMARY AND CONCLUSION

The aim of this research was to design a new approach to achieve aerocapture in a robust and near-optimal performance way. In this thesis, an explicit guidance method has been investigated for an Earth aerocapture problem. A novel analytical predictor-corrector guidance algorithm has been developed for providing robust guidance solutions with near-optimal ΔV performance.

A comprehensive review of the literature on the studies for aerocapture at Earth and some other planets was conducted in chapter 1. The vehicle model used in testing the aerocapture guidance algorithm was the Orion MPCV. The three-dimensional equation of motion of Orion MPCV were described in chapter 2. The impulsive maneuvers required during the post-atmospheric flight phase to establish the target orbit were mainly defined in two groups as in-plane and out-of-plane impulsive maneuvers. In-plane impulsive maneuvers were formulated based on the coplanar transfer with a single-tangential or two-tangential impulses.

In chapter 3, the bang-bang aerocapture optimization problem with a single inequality constraint were defined. The bank angle profile had a bang-bang structure during the atmospheric flight phase. MATLAB's Fmincon algorithm were used in the minimum-coplanar-ΔV optimization problem. The only variable optimized in the optimal aerocapture problem was the switching time, which is when the bank angle magnitude instantaneously transitions from 0 to 180 deg. The optimal FPA vs. altitude profile gave us the idea to define the sine of flight-path angle as an exponential function of altitude for the ascent

phase. In addition to this, the optimal bang-bang solutions were presented for comparison with the guided aerocapture performance from APC and NPC methods.

The analytical guidance scheme was developed by essentially utilizing the parameterizations of the aerodynamic acceleration effects ($\rho C_L/m$ and $\rho C_D/m$) and the FPA term. The $sin\gamma$ term was parameterized by an exponential function, while two options were considered to parameterize the terms $\rho C_L/m$ and $\rho C_D/m$: a Fourier series (scenario 1) or an exponential function (scenario 2) as described in chapter 4. For the parameterization of the $\rho C_L/m$ and $\rho C_D/m$ terms, the coefficients of these functions were found by a least-squares curve-fitting scheme. A closed-form equation for exit velocity and a closed-loop control law for tracking the reference trajectory were achieved by using these Fourier and exponential equations. The bank angle is the only control variable in the guidance algorithm. Bank control was open-loop (lift up) from EI to the switching point (near pull-up altitude) and then closed-loop (lift down) until atmospheric exit in order to emulate the bang-bang structure of optimal aerocapture trajectories. Bank reversal design was included in the analytical aerocapture guidance to minimize the plane-change ΔV_i.

Monte-Carlo simulations were used for the Earth aerocapture mission. Monte-Carlo dispersions in the vehicle parameters, entry state, and atmospheric density were given in chapter 5. For scenarios 1 and 2, the nominal and off-nominal guided trajectories were obtained from the Monte-Carlo simulations. The numerical solution of the APC guidance algorithm with scenario 1 and scenario 2 showed that although the 100% of the 1000 dispersed simulations are successfully captured for each scenario, the Fourier curve-fitting (scenario 1) is the better approach to achieve the target orbit with less insertion ΔV. The results of the comparison of APC and NPC methods for the in-plane ΔV performance

demonstrate that the proposed APC method clearly has a more performance advantage over the NPC method. Additionally, the APC guidance method was tested in a simulation environment with a wide range of entry FPA. All Monte-Carlo simulations reveal that the proposed APC guidance is robust, accurate, and provides near-optimal performance.

Key findings of this research are that the parameterization of the aerodynamic acceleration effects and the sine of FPA respectively with a Fourier series and exponential functions leads to closed-form solutions for the exit velocity and bank angle command; the determination of the switching time from open-loop to closed-loop control is a vital factor to the success of the aerocapture guidance; and including the attitude dynamics in the guidance algorithm improved the performance and robustness of the proposed APC.

REFERENCES

[1] Munk, M. M. and Moon, S. A., "Aerocapture Technology Development Overview," *IEEE Aerospace Conference*, Big Sky, MT, Mar. 2008, pp. 1–7. doi: 10.1109/aero.2008.4526545

[2] Hall, J. L., Noca, M. A., and Bailey, R. W., "Cost-Benefit Analysis of the Aerocapture Mission Set," *Journal of Spacecraft and Rockets*, Vol. 42, No 2, 2005, pp. 309–320. doi: 10.2514/1.4118

[3] Lockwood, M. K., Queen, E. M., Way, D. W., Powell, R. W., Edquist, K., Starr, B.W., Hollis, B.R., Zoby, E.V., Hrinda, G.A. and Bailey, R.W., "Aerocapture Systems Analysis for a Titan Mission," NASA TM-2006-214273, 2006.

[4] Spilker, T.R., Adler, M., Arora, N., Beauchamp, P.M., Cutts, J.A., Munk, M.M., Powell, R.W., Braun, R.D. and Wercinski, P.F., "Qualitative Assessment of Aerocapture and Applications to Future Missions," *Journal of Spacecraft and Rockets*, Vol. 56, No. 2, 2019, pp. 536–545. doi: 10.2514/1.a34056

[5] Hoffman, S., "A Comparison of Aerobraking and Aerocapture Vehicles for Interplanetary Missions," AIAA Paper 84-2057, Aug. 1984. doi: 10.2514/6.1984-2057

[6] Lockwood, M. K., "Titan Aerocapture Systems Analysis," AIAA Paper 2003-4799, July 2003**.** doi: 10.2514/6.2003-4799

[7] Zucchelli, E. M., "Aerocapture Guidance Numerical and Artificial Intelligence Solutions," Delft University of Technology, 2016.

[8] Cichocki, F., Cornara, S., Sanchez, M. and Cano, J.L., "Aerobraking Mission Analysis Tool for Mars Exploration Missions," *7th International Planetary Probe Workshop*, Barcelona, Spain, June 2010. doi: 10.13140/2.1.5173.6005

[9] Lyons, D.T., Beerer, J.G., Esposito, P., Johnston, M.D. and Willcockson, W.H., "Mars Global Surveyor: Aerobraking Mission Overview," *Journal of Spacecraft and Rockets*, Vol. 36, No. 3, 1999, pp. 307–313. doi: 10.2514/2.3472

[10] Kothari, M. and Padhi, R., "Energy-Insensitive Guidance of Solid Motor Propelled Long Range Flight Vehicles Using MPSP and Dynamic Inversion," *Proceedings of the 17th World Congress The Internatinal Federation of Automatic Control*, Seoul, Korea, July 2008. doi: 10.3182/20080706-5-kr-1001.02374

[11] Gurley, J. G. "Guidance for an Aerocapture Maneuver," *Journal of Guidance, Control, and Dynamics*, Vol. 16, No. 3, 1993, pp. 505–510. doi: 10.2514/3.21038

[12] Ro, T., Queen, E. M., and Striepe, S. A., "Martian Aerocapture Terminal Point

Guidance: A Reference Path Optimization Study," NASA/CP-1999-209235, 1999, pp. 85–99.

[13] Queen, E. M., "Angle-of-Attack-Modulated Terminal Point Control for Neptune Aerocapture," AAS Paper 04-129, Feb. 2004.

[14] Kozynchenko, A.I., "Development of Optimal and Robust Predictive Guidance Technique for Mars Aerocapture," *Aerospace Science and Technology*, Vol. 30, No. 1, 2013, pp. 150–162. doi: 10.1016/j.ast.2013.07.012

[15] Peng, Y. M., Xu, B., Fang, B. D., and Lei, H. L., "Analytical Predictor-Corrector Guidance Algorithm Based on Drag Modulation Flight Control System for Mars Aerocapture," *International Journal of Aerospace Engineering*, Vol. 2018, 2018. doi: 10.1155/2018/5907981

[16] Peng, Y. M., Xu, B., Lu, X., Fang, B. D., and Zhang, H., "Analytical Predictive Guidance Algorithm Based on Single Ballistic Coefficient Switching for Mars Aerocapture," *International Journal of Aerospace Engineering*, Vol. 2019, 2019. doi: 10.1155/2019/5765901

[17] Gamble, J. D., Cerimele, C. J., Moore, T. E., and Higgins, J., "Atmospheric Guidance Concepts for an Aeroassisted Flight Experiment," *Journal of the Astronautical Sciences*, Vol. 36, No. 1, 1988, pp. 45–71

[18] Masciarelli, J., Rousseau, S., Fraysse, H. and Perot, E., "An Analytic Aerocapture Guidance Algorithm for the Mars Sample Return Orbiter," AIAA Paper 2000-4116, Aug. 2000. doi: 10.2514/6.2000-4116

[19] Masciarelli, J., "Aerocapture Guidance Algorithm Development and Testing," *NASA Science Technology Conference*, College Park, MD, June 2007.

[20] Cerimele, C. J., and Gamble, J. D., "A Simplified Guidance Algorithm for Lifting Aeroassist Orbital Transfer Vehicles," AIAA Paper 1985-0348, Jan. 1985. doi:10.2514/6.1985-348

[21] Hanak, C., Crain, T. and Masciarelli, J., "Revised Algorithm for Analytic Predictor-Corrector Aerocapture Guidance: Exit Phase," AIAA Paper 2003-5746, Aug. 2003. doi: 10.2514/6.2003-5746

[22] Lockwood, M. K., Starr, B. R., Paulson Jr, J. W., Kontinos, D. A., Chen, Y. K., Laub, B., Olejniczak, J., Wright, M. J., Takashima, N. and Justus, C. G., "Systems Analysis for a Venus Aerocapture Mission," NASA TM-2006-214291, 2006.

[23] Masciarelli, J. and , Queen, E. M., "Guidance Algorithms for Aerocapture at Titan," AIAA Paper 2003-4804, July 2003. doi: 10.2514/6.2003-4804

[24] Hamel, J.-F. and Lafontaine J. D., "Improvement to the Analytical Predictor-Corrector Guidance Algorithm Applied to Mars Aerocapture," *Journal of Guidance, Control, and Dynamics*, Vol. 29, No. 4, 2006, pp. 1019–1022. doi: 10.2514/1.20126

[25] Rousseau, S., "An Energy Controller Aerocapture Guidance Algorithm for the Mars Sample Return Orbiter," AAS Paper 01-104, Feb. 2001, pp. 67–83.

[26] Bryant, L. E., Tigges, M. A., and Ives, D. G., "Analytical Drag Control for Precision Landing and Aerocapture," AIAA Paper 1998-4572, Aug. 1998.

[27] Perot, E., Fraysse, H., Rousseau, S. and Berges, J.C., "Comparison of an Analytical Predictor Corrector and a Terminal Point Controller for the Mars Sample Return Aerocapture.," Association A'eronautique et Astronautique de France, Paper AAAF, Mar. 2001, pp.14-67.

[28] Casoliva, J., Lyons, D. T., Wolf, A. A., and Mease, K. D., "Robust Guidance via a Predictor-Corrector Algorithm with Drag Tracking for Aero-Gravity Assist Maneuvers," AIAA Paper 2008-6816, Aug. 2008.

[29] Lafleur, J. M., "The Conditional Equivalence of ΔV Minimization and Apoapsis Targeting in Numerical Predictor-Corrector Aerocapture Guidance," NASA TM-2011-216156, Johnson Space Center, Houston, TX, Aug. 2011.

[30] Lu, P., Cerimele, C. J., Tigges, M. A., and Matz, D. A., "Optimal Aerocapture Guidance," *Journal of Guidance, Control, and Dynamics*, Vol. 38, No. 4, 2015, pp. 553–565. doi: 10.2514/1.G000713

[31] Webb, K. D., Lu, P., and Dwyer Cianciolo, A. M., "Aerocapture Guidance for a Human Mars Mission," AIAA Paper 2017-1900, Jan. 2017. doi: 10.2514/6.2017-1900

[32] Webb, K. D., "Evaluation of an Optimal Aerocapture Guidance Algorithm for Human Mars Missions," Iowa State University, 2016.

[33] Putnam, Z. R. and Braun, R. D., "Drag-Modulation Flight-Control System Options for Planetary Aerocapture," *Journal of Spacecraft and Rockets*, Vol. 51, No 1, 2014, pp. 139–150. doi: 10.2514/1.A32589

[34] Putnam, Z. R., "Improved Analytical Methods for Assessment of Hypersonic Drag-Modulation Trajectory Control," Georgia Institute of Technology, 2015.

[35] Braun, R. D., and Powell, R. W., "Predictor-Corrector Guidance Algorithm for Use in High-Energy Aerobraking System Studies," *Journal of Guidance, Control and Dynamics*, Vol. 15, No. 3, 1992, pp. 672–678. doi: 10.2514/3.20890

[36] Braun, Jits, R. Y., and Walberg, G. D., "Blended Control, Predictor-

CorrectorGuidance Algorithm: an Enabling Technology for Mars Aerocapture," Acta Astronautica, Vol. 54, No. 6, 2004, pp. 385–398. *Dynamics*, Vol. 15, No. 3, 1992, pp. 672–678. doi: 10.1016/S0094-5765(03)00159-0

[37] Evans, S. W., and Dukeman, G. A., "Examination of a Practical Aerobraking Guidance Algorithm," Journal of Guidance, Control, and Dynamics, Vol. 18, No. 3, 1995, pp. 471–477.

[38] Powell, R., "Numerical Roll Reversal Predictor Corrector Aerocapture and Precision Landing Guidance Algorithms for the Mars Surveyor Program 2001 Missions," AIAA Paper 98-4574, Aug. 1998. doi: 10.2514/6.1998-4574

[39] Brent, R. P., Algorithms for Minimization Without Derivatives, Prentice-Hall, Englewood Cliffs, NJ, 1973, Chaps. 4 and 5. doi:10.2307/2005713

[40] Rousseau, S., Perot, E., Graves, C., Masciarelli, J., and Queen, E. , "Aerocapture Guidance Algorithm Comparison Campaign," AIAA Paper 2002-4822, Aug. 2002. doi: 10.2514/6.2002-4822

[41] Bibb, K., Walker, E., Brauckmann, G. and Robinson, P., "Development of the Orion Crew Module Static Aerodynamic Database, Part II: Subsonic/Supersonic," *29th AIAA Applied Aerodynamics Conference*, Honolulu, Hawaii, June. 2011. doi: 10.2514/6.2011-3507

[42] Orion MPCV Model, from https://space.skyrocket.de/doc_sdat/orion-mpcv.htm (cited, Aug., 2020).

[43] Mazzaracchio, A., "Flight-Path Angle Guidance for Aerogravity-Assist Maneuvers on Hyperbolic Trajectories," *Journal of Guidance, Control, and Dynamics,* Vol. 38, No. 2, 2015, pp. 238-248. doi: 10.2514/1.G000670

[44] Miele, A., Zhao, Z. G., and Lee, W. Y., "Optimal Trajectories for the Aeroassisted Flight Experiment, Part 1, Equations of Motion in an Earth–Fixed System," NASA CR-186134, 1989.

[45] Kluever, C.A., *Space Flight Dynamics*, John Wiley & Sons., New Jersey, 2018.

[46] Fmincon Algorithm in MATLAB from, http://www.mathworks.com/help/optim/ug/fmincon.html *MathWorks*, (cited, Aug., 2020).

[47] Ode45 in MATLAB, from http://www.mathworks.com/help/matlab/ref/ode45.html *MathWorks* (cited, Aug., 2020).

[48] Moseley, P. E., "The Apollo Entry Guidance: A Review of the Mathematical Development and Its Operational Characteristics," TRW, Note 69-FMT-791,

Houston, TX, 1969.

[49] “Earth Global Reference Atmospheric Model 2010 (Earth GRAM 2010),” Software Package, Ver. MFS-32780-1, George C. Marshall Space Flight Center, Huntsville, AL, 2010, https://software.nasa.gov/software/MFS-32780-1 (cited, Aug., 2020)

APPENDIX A

In this thesis, MATLAB programming language was used for computation and simulation. Script and function m-files for the optimal bang-bang control problem and closed-form solutions (exit velocity and bank angle command) of the three-term Fouirer scenario are presented below.

Running Optimization M-file for Optimal Bang-Bang Control Problem:

```
clc; clear all;
format long     % output display format

global r2d d2r ft_to_m h_EI R_Earth mu_Earth  initial_state
        % global variables

%%% Conversion factors %%%
ft_to_m = 0.3048;    % feet to meters
r2d = 180/pi;        % radians to degrees
d2r = 1/r2d;         % degrees to radians

mu_Earth = 3.986*10^14;     % Earth's gravitational parameter, m^3/s^2
h_EI = 121920;              % altitude at entry interface (EI), m
R_Earth = 6378135;          % Earth radius, m

%%% Initial state variables %%%
r = h_EI + R_Earth;         % radial distance at EI, m
theta = -116.5*d2r;         % longitude at EI, rad
phi = -46.67*d2r;           % latitude at EI, rad
v_inertial = 11020;         % inertial velocity at EI, m/s
gamma_inertial = -5.91*d2r; % inertial flight-path angle at EI, rad
psi_inertial = 0*d2r;       % inertial heading angle at EI, rad

initial_state   =   [r,   theta,   phi,   v_inertial,   gamma_inertial,
psi_inertial];
```

```
ts_initial = 100;    % initial point
lb = 50;             % lower bound
ub = 150;            % upper bound

options        =        optimset('Display','iter','Algorithm','interior-
point','MaxIter',4000,'MaxFunEvals',70000,'TolFun',1e-20);
        % optimization options
[x, fval, exitflag, output] = fmincon(@obj_fun, ts_initial, [], [], [],
[], lb, ub, @nonlconstr, options)
        % syntax of Fmincon algorithm
```

Objective Function:

```
function [min_DV] = obj_fun(x)

global sigma d2r initial_state r_a      % global variables

ts = x(1);           % switching time, s

[v_Rel,  gamma_Rel,  psi_Rel]  =  fun_Iner_to_Rel  (initial_state(1),
initial_state(2), initial_state(3), initial_state(4), initial_state(5),
initial_state(6));
        % transforming state variables from inertial to Earth-relative

x0  =  [initial_state(1),  initial_state(2),  initial_state(3),  v_Rel,
gamma_Rel, psi_Rel];
        % Earth-ralative initial state
sigma = 0*d2r;       % bank angle during descent phase
options = odeset('MaxStep',1);  % ODE options
[t1, x1] = ode45(@fun_nominal_atmospheric, [0 ts], x0, options);
        % syntax of ode45 solver

x02 = [x1(end,1), x1(end,2), x1(end,3), x1(end,4), x1(end,5), x1(end,6)];
        % Earth-ralative state at switching time
sigma = 180*d2r;     % bank angle during ascent phase
options = odeset('Events', @myEventoptimal,'MaxStep',1);
```

```
        % ODE options
[t2, x2] = ode45(@fun_nominal_atmospheric,[ts  3000],x02,options);

[v_Iner_exit, gamma_Iner_exit] = fun_Rel_to_Iner (x2(end,1), x2(end,2),
x2(end,3), x2(end,4), x2(end,5), x2(end,6));
        % transforming state variables from Earth-relative to inertial

r_a = x2(end,1);    % apogee radius

[h_a, DV] = fun_calculation_DV (v_Iner_exit);

min_DV = DV;

end
```

Constraint Function:

```
function [c, ceq] = nonlconstr(x)

global sigma h_EI R_Earth d2r initial_state

ts = x(1);

[v_Rel,gamma_Rel,psi_Rel]    =    fun_Iner_to_Rel    (initial_state(1),
initial_state(2), initial_state(3), initial_state(4), initial_state(5),
initial_state(6));
        % transforming state variables from inertial to Earth-relative

x0  =  [initial_state(1),  initial_state(2),  initial_state(3),  v_Rel,
gamma_Rel, psi_Rel];
        % Earth-ralative initial state
sigma = 0*d2r;      % bank angle during descent phase
options = odeset('MaxStep',1);  % ODE options
[t1, x1] = ode45(@fun_nominal_atmospheric,[0  ts],x0,options);
        % syntax of ode45 solver

x02 = [x1(end,1), x1(end,2), x1(end,3), x1(end,4), x1(end,5), x1(end,6)];
```

```
        % Earth-ralative state at switching time
sigma = 180*d2r;     % bank angle during ascent phase
options = odeset('Events', @myEventoptimal,'MaxStep',1);
        % ODE options
[t2, x2] = ode45(@fun_nominal_atmospheric, [ts 3000], x02, options);

r_a = x2(end,1);     % apoapsis radius

c = (R_Earth+h_EI) - r_a;    % inequality constraint
ceq = [];                    % equality constraint

end
```

Main Function:

```
function [dx]=fun_nominal_atmospheric(t,x)

global  sigma mu_Earth h_EI R_Earth

%%% Vehicle parameters %%%
S = 19.86;                          % reference area, m^2
m = 8983.4;                         % vehicle mass, kg
CL = 0.3699;                        % lift coefficient
CD = 1.37;                          % drag coefficient

%%% State variables %%%
r = x(1);                           % radial distance, m
theta = x(2);                       % longitude, deg
phi = x(3);                         % geo-centric latitude, deg
V = x(4);                           % relative velocity, m/s
gamma = x(5);                       % relative flight path angle, deg
psi = x(6);                         % relative heading angle, deg

h = r-R_Earth;
[rho,~] = nominal_density_model(h/10^3);    % nominal density model

if h > h_EI
```

```
    J2 = 0;
else
    J2 = 0.00108262;            % Earth zonal coefficient
end
omega = 7.292115*10^-5;         % Earth angular velocity, rad/s

q = (V^2*rho)/2;                % q-bar, kg/(m-s^2)
L = q*S*CL/m;                   % lift acceleration, m/s^2
D = q*S*CD/m;                   % drag acceleration, m/s^2

%%% Trigonometric functions %%%
sphi = sin(phi);        cphi = cos(phi);        tphi = sphi/cphi;
sgamma = sin(gamma);    cgamma = cos(gamma);    tgamma = sgamma/cgamma;
spsi = sin(psi);        cpsi = cos(psi);
ssigma = sin(sigma);    csigma = cos(sigma);

%%% Gravitational acceleration components %%%
gr = mu_Earth/r^2*(1+J2*((R_Earth/r)^2)*(1.5-4.5*sphi^2));
gphi = mu_Earth/r^2*(J2*((R_Earth/r)^2)*(3*sphi*cphi));

%%% Equations of motion %%%
dx = zeros(6,1);
dx(1) = V*sgamma;
dx(2) = V*cgamma*spsi/(r*cphi);
dx(3) = V*cgamma*cpsi/r;
dx(4) = -D-gr*sgamma-gphi*cgamma*cpsi+...
        omega^2*r*cphi*(sgamma*cphi-cgamma*sphi*cpsi);
dx(5) = 1/V*(L*csigma+(V^2/r-gr)*cgamma+ gphi*sgamma*cpsi+...

2*omega*V*cphi*spsi+omega^2*r*cphi*(cgamma*cphi+sgamma*cpsi*sphi));
dx(6) = 1/V*(L*ssigma/cgamma+V^2/r*cgamma*spsi*tphi+...
        gphi*spsi/cgamma-2*omega*V*(tgamma*cpsi*cphi-...
        sphi)+omega^2*r/cgamma*spsi*sphi*cphi);
```

Post-Exit ΔV Function:

```
function [h_a,DeltaV] = fun_calculation_DV(v)

global  R_Earth mu_Earth r_a

%V in meter/s    %gamma in rad
d_apogee = 200000;      % desired target apogee, m
d_perigee = 200000;     % desired target perigee, m

a = mu_Earth/(2*mu_Earth/(r_a)-v^2);
        % semimajor axis of exo-atmospheric orbit, m
r_p = 2*a-r_a;          % perigee radius of exo-atmospheric orbit, m
h_a = r_a-R_Earth;      % apogee altitude of exo-atmospheric orbit, m

Delta_V1 = sqrt(2*mu_Earth)*(sqrt(1/r_a-1/(r_a+(R_Earth+d_perigee)))-
sqrt(1/r_a-1/(r_a+r_p)));
        % first impulse for apogee raise
Delta_V2 = abs(sqrt(2*mu_Earth)*(sqrt(1/(R_Earth+d_perigee)-
1/(R_Earth+d_apogee+R_Earth+d_perigee))-sqrt(1/(R_Earth+d_perigee)-
1/(r_a+(R_Earth+d_perigee)))));
        % second impulse for apogee correction (if necessary)
DeltaV = Delta_V1+Delta_V2;
        % total in-plane velocity increment
end
```

ODE Event Function:

```
function [value, isterminal, direction] = myEventoptimal (~, xx)

value      = (xx(5) - 0);     % the FPA value that we want to be zero
isterminal = 1;   % stop the integration
direction  = -1;  % -1 = Decreasing, 1 = Increasing

end
```

Closed-Form Solutions for Exit Velocity and Bank Angle Command Exit Velocity with Three-Term Fourier Scenario:

```
function [V_exit, sigma] = fun_exit_velocity_FOURIER3(h_now, v_Iner_now,
gamma_Iner_now, gamma_exit, CFL, CFD)
global R_Earth  mu_Earth S

%%% Constants A0 and A1 (Eqs. 51-53) %%%
z_now = log(sin(gamma_Iner_now));
z_exit = log(sin(gamma_exit));
h_exit = 121920;

Q = inv([1 h_now; 1 h_exit])*[z_now; z_exit];
q0 = Q(1);   q1 = Q(2);
A0 = exp(q0);   A1 = -q1;

B = -S/(2*A0);      % constant term

%%% Drag-only exit velocity (Eq. 36) %%%
Drag_only_exit_velocity = v_Iner_now*exp(B*(...
exp(A1*h_exit)*(CFD(1)/A1+...
CFD(2)*(CFD(end)*sin(CFD(end)*h_exit)+A1*cos(CFD(end)*h_exit))
/(CFD(end)^2+A1^2)+...
CFD(3)*(-CFD(end)*cos(CFD(end)*h_exit)+A1*sin(CFD(end)*h_exit))
/(CFD(end)^2+A1^2)+...
CFD(4)*(2*CFD(end)*sin(2*CFD(end)*h_exit)+A1*cos(2*CFD(end)*h_exit))
/(4*CFD(end)^2+A1^2)+...
CFD(5)*(-2*CFD(end)*cos(2*CFD(end)*h_exit)+A1*sin(2*CFD(end)*h_exit))
/(4*CFD(end)^2+A1^2)+...
CFD(6)*(3*CFD(end)*sin(3*CFD(end)*h_exit)+A1*cos(3*CFD(end)*h_exit))
/(9*CFD(end)^2+A1^2)+...
CFD(7)*(-3*CFD(end)*cos(3*CFD(end)*h_exit)+A1*sin(3*CFD(end)*h_exit))
/(9*CFD(end)^2+A1^2))-...
```

```
exp(A1*h_now)*(CFD(1)/A1+...
CFD(2)*(CFD(end)*sin(CFD(end)*h_now)+A1*cos(CFD(end)*h_now))
/(CFD(end)^2+A1^2)+...
CFD(3)*(-CFD(end)*cos(CFD(end)*h_now)+A1*sin(CFD(end)*h_now))
/(CFD(end)^2+A1^2)+...
CFD(4)*(2*CFD(end)*sin(2*CFD(end)*h_now)+A1*cos(2*CFD(end)*h_now))
/(4*CFD(end)^2+A1^2)+...
CFD(5)*(-2*CFD(end)*cos(2*CFD(end)*h_now)+A1*sin(2*CFD(end)*h_now))
/(4*CFD(end)^2+A1^2)+...
CFD(6)*(3*CFD(end)*sin(3*CFD(end)*h_now)+A1*cos(3*CFD(end)*h_now))
/(9*CFD(end)^2+A1^2)+...
CFD(7)*(-3*CFD(end)*cos(3*CFD(end)*h_now)+A1*sin(3*CFD(end)*h_now))
/(9*CFD(end)^2+A1^2))));

%%% Drag-free exit velocity (Eq. 40) %%%
Drag_free_exit_velocity = sqrt(v_Iner_now^2 +...
2*mu_Earth/(R_Earth+h_exit) - 2*mu_Earth/(R_Earth+h_now));
%%% Exit velocity gravity correction (Eq. 41) %%%
Exit_velocity_gravity_correction = Drag_free_exit_velocity - v_Iner_now;
%%% Analytical exit velocity (Eq. 42) %%%
V_exit = Drag_only_exit_velocity + Exit_velocity_gravity_correction;

%%% Lift-acceleration term (rho*CL/m) (Eq. 30) %%%
rho_CL_m = (CFL(1)+...
    CFL(2)*cos(h_now*CFL(end)) + CFL(3)*sin(h_now*CFL(end)) +...
    CFL(4)*cos(2*h_now*CFL(end)) + CFL(5)*sin(2*h_now*CFL(end))+...
    CFL(6)*cos(3*h_now*CFL(end)) + CFL(7)*sin(3*h_now*CFL(end)));

%%% Closed-loop bank angle (Eq. 58) %%%
sigma = acos((-A1*v_Iner_now^2*sin(gamma_Iner_now)*tan(gamma_Iner_now)-
(v_Iner_now^2-mu_Earth/(R_Earth+h_now))*cos(gamma_Iner_now)/...
(R_Earth+h_now))/0.5*v_Iner_now^2*S*rho_CL_m);

end
```

VITA

Ibrahim Halil Cihan was born on August 2, 1989, in Sanliurfa, Turkey, where he received his primary and secondary education. He joined Yildiz Technical University in Istanbul, Turkey and received his B.S degree with honors in Mechanical Engineering in 2012. Upon completing B.S, he was awarded the Turkish Ministry of National Education fellowships for the study-abroad program. He then joined the Mechanical and Aerospace Engineering department at the University of Missouri – Columbia and received his M.S degree in 2016 and Ph.D. in 2020. His research interests are guidance and control of aerospace vehicles and optimal path planning.